Structural and electronic properties of Si:TiO_2 interfaces from first principles



Yide Chang

Linacre College, University of Oxford

A thesis submitted for the Degree of
MSc by Research in Materials

Trinity Term 2023

Abstract

A number of transition metal oxides that serve as electron/hole selective contacts in solar cells have attracted attention due to their simple and low-cost deposition methods. Among them, TiO_2 has been identified as a promising electron transport layer in Si solar cells. Experiments have shown that the Si:TiO_2 interface undergoes structural changes depending on how it was fabricated. However, the sensitivity of electronic properties, such as band alignments, to different structural features of the Si:TiO_2 interface is not well understood. In this thesis, first-principles calculations are performed to calculate the band alignments between Si and anatase TiO_2, investigating different surface orientations and terminations. By using the vacuum-level alignment method, a 2.1 eV reduction in band offsets is observed for the O-terminated Si slab compared to other terminations. However, this large reduction in band offset is not found when using the heterointerface alignment method in which band offsets are obtained with four different heterointerface models. Even though these heterointerface models contain an excess of oxygen, their offsets agree well with the vacuum-level alignments using stoichiometric or H-terminated slabs. Moreover, a 0.4 eV increase in band offset is found for the anatase (101) surface compared to the (001) surface for both alignment methods. Additionally, different exchange-correlation treatments are investigated including rSCAN, PBE+U, and post-processing GW corrections. By considering the results of calculations on a test set of 21 semiconductors, rSCAN is demonstrated to provide more accurate band offsets than PBE, but the errors are still of order 0.7 eV. Next, the infrared spectra of two Si:TiO_2 interface models are calculated to assist future spectroscopy experiments in assigning observed features to particular structures. Finally, a comparison of oxygen and hydrogen-terminated surfaces is carried out for Si and C, linking the current study to previously published work on diamond-C surfaces.

Preface

The work presented in this thesis has been carried out by the author in the Department of Materials, University of Oxford from October 2021 to May 2023, under the supervision of Dr. Christopher Patrick and Prof. Jonathan Yates. The research presented in this thesis is entirely original, and any work of others has been appropriately cited. This thesis has not been previously submitted for a degree at this or any other academic institution. Some of the work has been published in peer-reviewed journals and presented at conferences, as outlined below:

Journal articles

First-principles band alignments at the Si:anatase TiO_2 interface

Yide Chang, Jonathan Yates, and Christopher Patrick. *ACS Omega* 8, 20138 (2023), DOI: 10.1021/acsomega.3c02865.

Conferences

The 6th Energy Materials workshop of the Thomas Young Centre, poster presentation, December 2022, UK.

Contents

Abstract i

Preface ii

Contents iii

1 Introduction 1

1.1 Solar photovoltaics 1

1.1.1 Renewable energy demand 1

1.1.2 Global demand for solar cells 2

1.1.3 Generations of solar cells 2

1.1.4 Designs of C-Si solar cells 3

1.2 Band alignments 4

1.2.1 General concept 4

1.2.2 Types of band alignments 5

1.3 Outline and organization of the thesis 5

2 Literature review 7

2.1 Introduction 7

2.2 Conceptual design of photovoltaic cells 7

2.2.1 Directly metallized contacts 7

2.2.2 Passivating contacts 9

2.2.3 Dopant-free passivating contacts 11

2.2.4 TiO_2 in c-Si solar cells 12

2.3 Anatase and rutile TiO_2 13

2.4 Experimental measurements of Si:TiO_2 band alignments 15

2.5 Key research questions for this thesis 15

3 First-principles methodologies **17**

3.1 Introduction 17

3.2 Density-functional theory 17

3.3 Plane wave basis set 20

3.4 Pseudopotentials 21

3.5 "Band gap problem" 22

3.6 Jacob's ladder 23

3.6.1 Local density approximation 23

3.6.2 Generalized gradient approximation 24

3.6.3 The DFT+U method 25

3.6.4 Meta-generalized gradient approximation 27

3.6.5 Hybrid functional 27

3.6.6 GW approximation 28

4 DFT calculations in this thesis **30**

4.1 Introduction 30

4.2 Calculating band alignments 30

4.2.1 The vacuum-level alignment method 30

4.2.2 The heterointerface alignment method 32

4.3 Calculating infrared spectroscopy 34

4.3.1 Introduction 34

4.3.2 Finite displacement method 34

4.3.3 Dynamical matrix 36

5 Performance of meta-GGA rSCAN **39**

5.1 Introduction 39

5.2 General concept of rSCAN 39

5.3 Testing performance of rSCAN 40

5.3.1 Constructing slab models 40

5.3.2 Computational details 41

5.3.3 Comparison to previous calculations and experiments 41

5.4 Conclusion 44

6 First-principles band alignments at the Si:anatase TiO_2 interface 45

6.1 Introduction 45

6.2 Methods 45

6.2.1 Constructing Si slabs 45

6.2.2 Constructing TiO_2 slabs 47

6.2.3 Constructing Si:anatase TiO_2 interface models 48

6.2.4 Computational details 49

6.3 Convergence tests 50

6.3.1 Cutoff energy 50

6.3.2 k-point sampling for bulk Si and TiO_2 51

6.3.3 k-point sampling for Si and TiO_2 slabs 53

6.3.4 Vacuum spacing and slab thickness 54

6.4 Results 55

6.4.1 Structural and electronic properties of bulk anatase TiO_2 and Si 55

6.4.2 Vacuum-level alignments and effects of surface termination 57

6.4.3 Influence of exchange-correlation treatment 60

6.4.4 Heterointerface alignments 62

6.4.5 Effects of lattice mismatch on the band alignments 65

6.5 Conclusion 67

7 Infrared spectra of Si, TiO_2 slabs, and Si:TiO_2 interface models 69

7.1 Introduction 69

7.2 Constructing slabs and interface models 69

7.3 Computational details 71

7.4 Infrared spectra 71

7.4.1 Infrared spectra of Si slabs 71

7.4.2 Infrared spectra of the anatase TiO_2 slab 75

7.4.3 Infrared spectra of Si:TiO_2(001) interface models 76

7.5 Conclusion 77

8 DFT calculations of C slabs **78**

8.1 Introduction 78

8.2 Constructing C slabs and computational details 78

8.3 Stabilities and EAs of oxygen-terminated C slabs 80

8.4 Infrared spectra of oxygen-terminated C slabs 80

8.5 Stabilities and EAs of hydrogen-terminated C slabs 82

8.6 Conclusion 83

9 Conclusion **84**

9.1 General overview 84

9.2 Future work 86

A Convergence tests **88**

A.1 Introduction 88

A.2 "Fine grid scale" 88

A.3 k-point sampling for bulk TiO_2 in the z-axis 90

A.4 k-point sampling for Si and TiO_2 slabs 90

A.5 Convergence tests for Si and TiO_2 within the Quantum ESPRESSO package . . . 94

A.6 Convergence tests for C cell 96

B Band structure and DOS of the Si:TiO_2 interface **98**

B.1 Introduction 98

B.2 Model 1 98

B.3 Model 2 99

Bibliography **101**

Acknowledgements **I**

Chapter 1

Introduction

1.1 Solar photovoltaics

1.1.1 Renewable energy demand

Due to the rapid expansion of the world's population in the 21st century, the demand for energy has been growing exponentially. To meet this demand, the primary approach to producing energy is burning fossil fuels, such as coal, oil, and gas, even though they are harmful to the environment and not sustainable [1] [2]. In 2020, about 84% of the world's energy was produced by consuming fossil fuels [3]. The release of carbon dioxide along with other gases (known as greenhouse gases) produced by burning fossil fuels has resulted in global warming or climate change, causing significant harm to global economic, environmental, and human lives [4]. Ref. 5 shows that the Earth's surface temperature is rising at a rate of approximately 0.2 °C per decade. Based on this rate, it is predicted that global temperature will surpass 1.5 °C above pre-industrial levels by the year 2037 [5]. To address this pressing issue, an agreement was concluded among 196 countries in 2015 that requires member nations to reduce greenhouse gas emissions and achieve the goal of limiting the increase in global average temperatures to below 2 °C [6]. China and the United States have proposed the goal of achieving zero greenhouse gas emissions by 2060 and 2050, respectively [7]. To achieve this goal, at least 80% of electricity need to be shifted to low-carbon sources [5]. Therefore, as the demand for energy continues to rise, renewable energy technologies have gained significant attention from the market.

Instead of consuming fossil fuels, renewable energies, such as solar and wind energy, are produced from natural and sustainable resources. According to Ref. 8, 29% of the global electricity in 2020 was generated from renewable energy sources. This percentage is predicted to increase

to 45% by the year 2040. Most of the renewable energy is likely to come from solar, wind, and hydropower [8]. Today, more industries are focusing on solar power as the cost of solar energy continues to drop due to the development of fabrication processes, materials, and technologies [5].

1.1.2 Global demand for solar cells

Solar energy is considered a highly promising renewable energy resource due to its lower material and installation costs and environmentally friendly characteristics when compared with other energy technologies [9]. Since the discovery of the crystalline Si (c-Si) solar cell in 1954, many affordable alternative types of solar cells, such as mono-crystalline, thin-film solar cells [10], organic solar cells [11], and perovskite solar cells [12], have been developed. According to Ref. 13, prices of solar cells have decreased by almost 90% along with an improvement in quality from 2008 to 2018. In the year 2017, 1.7% of global electricity was produced by solar photovoltaic (PV) modules [14]. PV cells are now the cheapest option for new electricity generation in many countries and have shown the second-largest generation growth of all renewable technologies in 2021 [9]. It is expected that the PV cell market will reach an annual growth rate of 25% from 2022 to 2026 [15].

1.1.3 Generations of solar cells

Instead of focusing on lowering the cost of PV cells, various designs of PV cells have been developed followed by different manufacturing methods, leading to the rapid growth of power conversion efficiencies (PCE) of PV cells. Depending on the different designs and types of materials used for PV cells through the last few decades, PV cell technologies can be categorized into four generations. The first generation of PV cells is based on mono-crystalline and poly-crystalline silicon [16]. Since the discovery of c-Si solar cells, the PCE has increased by 20.1%, reaching a current record of 26.1% [17]. The second generation is thin-film PV cells designed based on amorphous Si [18] and copper indium gallium selenide (CIGS) [10, 19], etc. The CIGS are promising absorber materials for solar cells due to suitable direct band gaps ranging from 1 eV to 2.6 eV and high absorption coefficients. The second generation PV cells have been designed to be a lower-cost replacement for c-Si solar cells. The third generation of PV cells includes a wide range of designs, ranging from expensive high-efficiency designs to inexpensive low-efficiency designs [20]. This category includes dye-sensitized solar cells [21], perovskite solar cells [22], chalcogenide-based solar cells [23], and solar cells based on organic polymers [24], etc. These cells are still in the

experimental stage and have not yet been widely used in the commercial market. [16]. Fourth generation PV cells are based on the combination of polymer thin films and inorganic nanostructures or organic-based nanomaterials [25]. Fourth generation PV cells are also referred to as hybrid inorganic cells, which have promising potential for becoming the future PV cells due to their lower cost, flexibility, and high stability properties [26].

1.1.4 Designs of C-Si solar cells

PV cell technologies convert energy from sunlight directly into electricity by the PV effect [27]. The dominant design of the PV cell in the current global market is c-Si based solar cells, occupying a 95% share of the PV cell market [14]. The basic structure of a c-Si solar cell contains doped thin silicon wafers to create a p-n junction. The Si is doped with group III elements to form p-type Si and doped with group V elements to form n-type Si. The p-n junction is a boundary between two regions of the silicon allowing for the separation of electrons and holes generated by the absorbed photons. Specifically, as n and p-type Si wafers are combined together, a depletion region will be formed, which creates an electric field. As photons enter the device, their energy, which is associated with their wavelength or frequency, needs to be larger than the band gap of Si in order to excite electrons from the valence band to the conduction band and leave holes behind. The excited electrons will then accumulate in n-type Si and the holes will accumulate at p-type Si. As the accumulation continues and creates a potential difference, electrons can be extracted via an external circuit and generate electricity [27].

There have been many designs of c-Si solar cells. The initial design was based on directly metallized contacts, where a metal layer is overlaid on the Si wafer. This design requires a relatively simple and low-cost manufacturing process [14]. However, this direct contact of the metal with a silicon wafer causes recombination losses of the photogenerated holes and electrons and limits the PCE [28, 29]. The heavy doping approach lowers the recombination rate but leads to Auger recombination [30] [31]. To further reduce manufacturing costs and increase PCE, a passivating contact design has been introduced in which thin films like SiO_x are inserted between the c-Si wafer and metal terminal [32]. Another approach to using this passivating contact idea is inserting dopant-free materials like TiO_x [33]. Materials such as metal oxides with wider band gaps have more suitable optical characteristics for PV cells [14]. More discussion about different designs of c-Si solar cells is given in Chapter 2. The focus of this thesis is on the interface between the dopant-free wide band semiconductor TiO_2 and Si wafer.

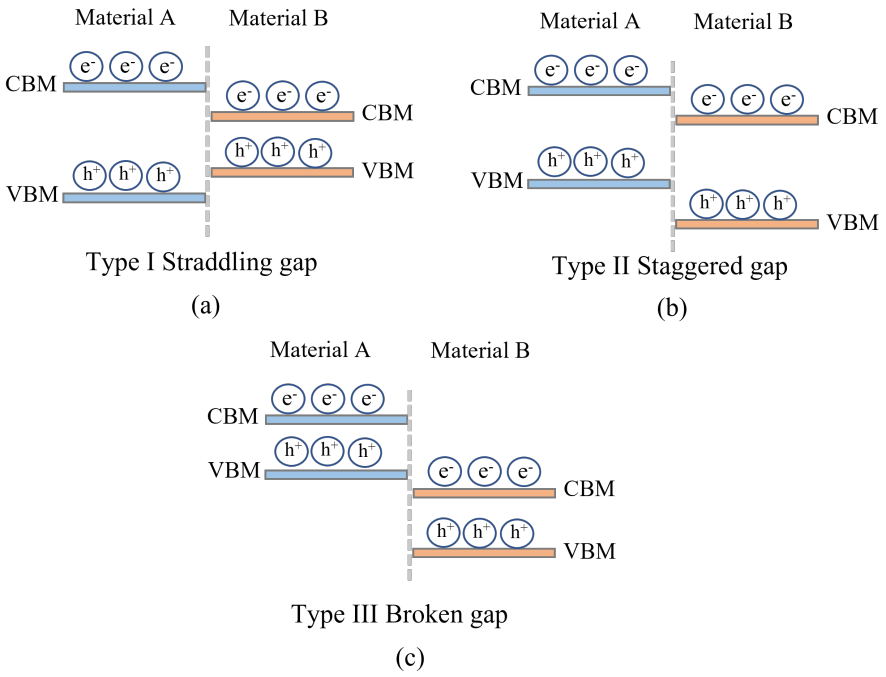


Figure 1.1: Types of band alignments (a) Type I straddling gap, (b) Type II staggered gap, and (c) Type III broken gap. This figure is reproduced from Figure 1 in Ref. 34.

1.2 Band alignments

1.2.1 General concept

Proper band alignment between materials is one of the crucial quantities in electronic devices [35]. When two different materials are brought into contact, their energy bands can shift relative to each other due to differences in their electronic properties. The way that energy bands are aligned at the interface is called band alignment. In the case of the semiconductor:metal interface, band alignment is determined by the Schottky barrier heights at the interface and denoted as the valence and conduction band discontinuities. Large barriers in devices will prevent charge transport while small barriers enable charge transport across an interface [36, 37].

In order to physically describe the relative band alignment at the heterointerface, band offsets are used, which refer to the relative position of the valence band maximum (VBM) and conduction band minimum (CBM) of the two materials. The band offset can be either positive or negative. In solar cell systems, the conduction band offset (CBO) often describes the flow of electrons, while the valence band offset (VBO) describes the flow of holes [38, 39].

1.2.2 Types of band alignments

There are three possible types of band alignment: type I straddling gap, type II staggered gap, and type III broken band alignment. The type I alignment describes the CBM and VBM of one material located within the band gap of the other material, given in Fig. 1.1a. In a type II alignment, either the CBM or VBM of each material is located within the band gap of the other material, shown in Fig. 1.1b. The potential barrier at the interface can easily promote electron and hole carrier transfer and separate charge carriers, which can significantly enhance the efficiency of PV cells. This type of band alignment is often seen in heterojunctions between different semiconductors. The III band alignment is referred to as the broken gap, where the VBM of one material is higher than the CBM of the other material, shown in Fig. 1.1c [34, 37, 40]. The VBO and CBO are identified as the difference between the VBM and CBM of the two materials that form an interface, respectively [40]. Since the band offset is an important fundamental property and crucial to device performance, the primary focus of this thesis is to calculate the band offsets of the Si:TiO_2 interface using two different approaches.

1.3 Outline and organization of the thesis

The structure of this thesis is as follows. In Chapter 2, a literature review is presented, focusing on the background information of directly metallized and passivating contact solar cells. The role of TiO_2 in c-Si solar cells is explored, along with a comparison between the anatase and rutile TiO_2. Furthermore, various experimental measurements of the Si:TiO_2 interface's band alignments are discussed. Moving on to Chapter 3, the theoretical background of the first-principles calculations used in this thesis is introduced. This includes a brief overview of different types of exchange-correlation functionals in Jacob's ladder. Chapter 4 provides a general review of the two commonly used methods for calculating band alignment through density-functional theory (DFT). These methods will later be applied to determine the band alignment of the Si:TiO_2 interface. Furthermore, the finite displacement method and the dynamical matrix, used for calculating the infrared spectra, are also discussed. In Chapter 5, the theoretical concept of the regularized SCAN (rSCAN) exchange-correlation functional [41] is introduced, followed by the presentation of the computational results for 21 semiconductors. These results aim to test the performance of rSCAN. In Chapter 6, the calculated band alignments of the Si:TiO_2 interface, incorporating various structural features, are presented. Additionally, the chapter includes a discussion on the influence of

different exchange-correlation functionals on the determined band alignments of the Si:TiO_2 interface. Chapters 7 and 8 focus on the calculated infrared spectra of Si, TiO_2, C slabs, and Si:TiO_2 interface models. Furthermore, a comparison is made between oxygen and hydrogen-terminated surfaces for Si and C, which is related to the previously published work on diamond-C surfaces. Finally, Chapter 9 provides a summary of the thesis's findings and proposes possible directions for future research.

Chapter 2

Literature review

2.1 Introduction

The objective of this chapter is to provide an overview of the literature regarding different designs of c-Si solar cells. Initially, the commonly used design with directly metallized contacts is presented along with certain surface phenomena that unexpectedly limit its PCE. Then, the passivating and dopant-free passivating contacts, which incorporate an interlayer between the Si layer and the overlying metal layer contacts, are briefly discussed. Among various transition metal oxides (TMOs), TiO_2 has been identified as a promising electron transport layer in c-Si solar cells. Therefore, the role of TiO_2 in c-Si solar cells in various experimental studies is summarized, followed by descriptions of anatase and rutile TiO_2. As this thesis primarily focuses on Si:TiO_2 band alignments, several experimentally determined band offsets are provided, which are later compared with the calculated offsets in this thesis.

2.2 Conceptual design of photovoltaic cells

2.2.1 Directly metallized contacts

In order to generate an electrical current in a solar cell, it is necessary to separate the photo-excited electrons and holes within the light-absorbing semiconductor and direct them toward the negative and positive contacts, respectively [14]. This separation process has led to the conceptual design of putting a conductive layer, such as a metal, directly onto a silicon wafer. This directly metallized contact approach is based on the Schottky-Mott theory. In a c-Si solar cell, the asymmetrical work function of the overlying metal layer can control the surface potential of the Si, with electrons

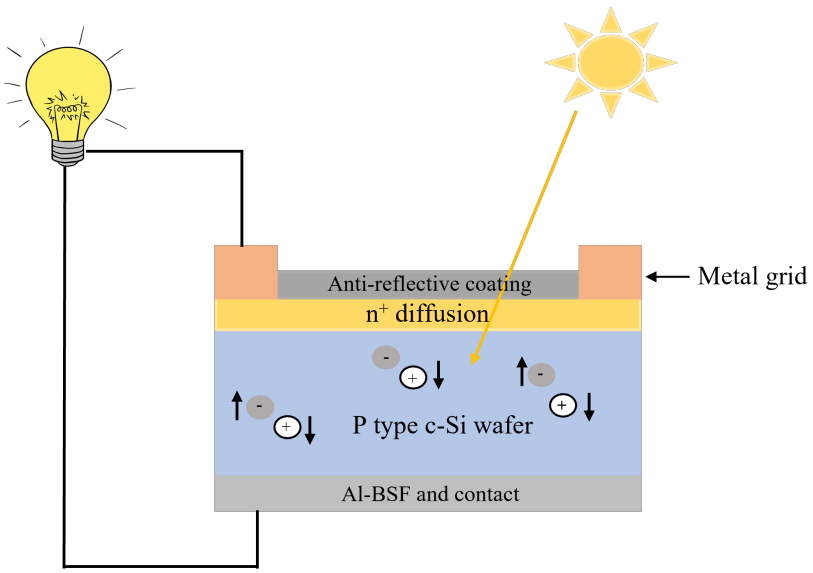


Figure 2.1: Schematic diagram of a directly metallized contacts (AL-BSF) c-Si solar cell demonstrating electron-hole pair generation. This figure is reproduced from Box1 in Ref. 14.

and holes accumulating at a low and high work function, respectively. By choosing an optimized metal contact, the electrical losses of the solar cell can be controlled, and the Schottky barrier, which is a potential energy barrier that impedes the charge transfer at the contact interface, will be small [42, 43]. One example is the aluminum back surface field cell (Al-BSF), where the whole rear-side silicon surface is covered with aluminum, as shown in Fig. 2.1. In the case of a p-type c-Si solar cell, where a thick p-type Si wafer acting as the absorber layer is placed under a thin n-type Si wafer, the depositing Al will form a barrier with p-type Si to prevent the flow of the minority carrier, electrons in this case, to the rear surface and reduce the recombination. An additional upgrade to the Al-BSF design is to add a passivation layer (often aluminium oxide) on the rear side to improve passivation and internal reflection. This design is called passivated emitter and rear contact solar cell (PERC) [14, 16]. The Al-BSF and PERC solar cells are categorized as directly metallized contact c-Si cells, having PCE around 20 % and 24 %, respectively [44].

However, several unexpected surface phenomena, which were not accounted for in the Schottky-Mott theory, are present in directly metallized contact solar cells, such as dangling bonds and metal-induced gap states (MIGS) [45]. Dangling bonds can be understood as unsaturated chemical bonds that occur at the surface of a semiconductor. These bonds appear when atoms on the surface do not have enough neighboring atoms to bond with, resulting in one or more unpaired electrons that are not involved in bonding. These unpaired electrons can give rise to undesirable electronic properties, such as surface states. These dangling bonds at the semiconductor surface will interact with metal states to generate MIGS at the metal and semiconductor junction [14]. In-

side the semiconductor band gap, the metal travelling wavefunction persists in an evanescent state and penetrates a short distance into the semiconductor, resulting in the formation of electronic states in the semiconductor's band gap. In addition, dangling bonds and MIGS act as amphoteric states that can function as either an acid or a base to accept or donate electrons depending on the conditions. These states exhibit charge states of +1, 0, and -1, leading to a substantial increase in recombination rate and a decrease in the efficiency of solar cells [42, 46]. Furthermore, both dangling bonds and MIGS can cause Fermi-level pinning (FLP), where the Fermi-level of the semiconductor surface is pinned to a particular energy level due to the presence of a high density of interface states. This effect will limit the ability to modify the surface Fermi level of semiconductors when contacting different metals and results in the depletion of charge carriers and reduction of the PCE [47]. To reduce the effect of FLP on directly metallized solar cells, the heavy doping approach is employed to reduce the width of the depletion region within the semiconductor so that the charge carriers can tunnel through the Schottky barrier. Although a heavily doped surface can achieve relatively low recombination currents, the PCE of this method is not significant due to the band gap narrowing and unavoidable Auger recombination [48]. Auger recombination can be described as a high-energy electron or hole recombining with a lower-energy electron or hole, transferring the excess energy to a third charge carrier in the form of kinetic energy rather than emitting a photon, resulting in the generation of additional electron-hole pairs or the heating of the material [30].

In terms of Si, it has four valence electrons in its outermost shell, which requires the formation of four bonds with neighboring atoms to fully saturate the valence shell and achieve a more stable structure. By cutting Si along the (001) crystallographic plane, the surface will have two half-filled dangling bonds per atom, creating surface states. Dangling bonds of Si can be terminated by applying a chemical reaction with oxygen or hydrogen to form a Si-O or Si-H bond at the surface, which relocates the energy of the defect state to be inside the valence or conduction bands [49]. However, the energy of MIGS is not eliminated when Si is passivated using hydrogen or an oxide layer; instead, it can only be decreased more rapidly by inserting a passivating interlayer between the Si layer and the metal layer. This approach is called the passivating contact approach [46].

2.2.2 Passivating contacts

To saturate dangling bonding and reduce the impact of MIGS and FLP, a common approach is to insert a thin passivating interlayer between the semiconductor layer and the overlying metal

layer. This approach will not only passivate the surface states but will also physically separate the semiconductor and metal, which decreases the FLP effects. Based on experimental studies, the FLP effects from directly metallized contacts are particularly strong but can be alleviated by introducing a wider-gap layer, such as an oxide layer [50]. The rate of MIGS decay is shown to decrease at a faster rate within the wider-gap semiconductor [34, 51]. In addition, unlike heavily doped contacts that require processing at high temperatures above 750 °C, some of the passivating internal layers can be deposited at a relatively lower temperature of approximately 250 °C, simplifying the fabrication process [52].

The original design of passivating contacts on c-Si solar cells has a metal-insulator-semiconductor (MIS) structure, similar to the metal-oxide-semiconductor structure [53]. Ever since then, various structures based on the MIS configuration have been proposed, [54–56]. These configurations have demonstrated remarkable performance and PCE during their respective periods of investigation. MIS contacts have been implemented in both p-type and n-type c-Si solar cells, achieving PCE higher than 21% [14].

In recent developments, remarkable progress has been made in achieving a high PCE of 25.1% in Si heterojunction (SHJ) based cells. The thin n or p doped hydrogenated amorphous silicon (a-Si:H) layer is in contact with the c-Si absorber wafer in order to either form a p-n junction or provide surface passivation. An intrinsic a-Si:H or SiO_2 interlayer is inserted between the c-Si wafer and doped a-Si:H layer in order to passivate surface defects and mitigate FLP, which enables the doped a-Si:H layer to control the surface potential of the Si wafer and facilitate the charge carrier selectivity process [57, 58]. Despite the impressive PCE of SHJ-based solar cells, there are still many shortcomings, such as current loss due to parasitic photon absorption and high fabrication cost due to complicated deposition processes. The parasitic absorption occurs in the front a-Si:H layer and transparent conductive oxide (TCO) in which incident light is absorbed by them rather than the absorber layer, resulting in the generation of excess carriers that do not collect as current and recombination of electron-hole pairs before collection [59, 60]. To reduce parasitic absorption, an interdigitated back contact (IBC) cell has been developed, where the doped a-Si:H layer and TCO are relocated to the rear side of the solar cell facing away from sunlight, minimizing parasitic absorption and achieving a PCE of 26.7% [61].

Despite achieving high PCE, fabricating the IBC cell with a-Si:H and doped a-Si:H is very challenging from an industry perspective due to the complicated and dangerous deposition process for the doped a-Si:H layers. The doped a-Si:H layers are typically deposited by plasma-enhanced

chemical vapor deposition which involves the use of pyrophoric silane, which is highly reactive and spontaneously ignites in the presence of air [62], and toxic boron/phosphorous gas precursors. Therefore, there is a need to explore alternative passivating contacts that can be deposited safely and efficiently. TMOs have attracted much attention as dopant-free passivating materials because of their low-cost deposition methods, such as thermal evaporation, spray, and brush painting methods [63].

2.2.3 Dopant-free passivating contacts

Dopant-free wide band gap materials, including metal compounds, low-dimensional semiconductors, and organic materials, are increasingly being used as promising alternatives for the passivation of c-Si solar cells [64]. Specifically, dopant-free wide band gap materials, especially the TMOs, have more suitable optical characteristics for c-Si solar cells, such as higher transparency, which reduces parasitic absorbance at the front surface. The potential to tune the electronic and optical properties through control of structure and stoichiometry provides diverse prospects for designing the interface. [14, 65].

TMOs are oxides of chemical elements that belong to the d-block of the periodic table. The selection of TMOs as either electron or hole selective is dependent upon their work function. A high work function is suitable for a hole-selective TMO, while a low work function is eligible for an electron-selective TMO [14]. Due to the transfer of electrons from the valence shell of transition metals to oxygen atoms in order to satisfy the octet rule, the majority of TMOs are d^0 oxides, in which the valence band is occupied by oxygen 2p-states, and the conduction band is occupied by transition metal d-states. Oxygen vacancies are a common feature of d^0 oxides, and due to the entirely unoccupied d orbitals, metal charge transfer occurs more easily [66, 67]. PV performance can be modified by changes in the work function. However, authors of Ref. 68, 69 mention that controlling the work function of TMOs is challenging because different preparation methods of TMOs can cause stoichiometric changes. Deposition temperature, ambient conditions, and different fabrication processes influence the performances of dopant-free passivating contacts solar cells, especially when using TMOs. Annealing is also an important step because it can generally change the work function, optical band gap, and transmittance of the material [70, 71]. However, it remains unclear how modifications to the structural characteristics may influence the band alignments of solar cells.

Experimental studies have been conducted on several n-type TMOs, such as TiO_x [63], ZnO_x

[72], and TaO_x [73], for their potential application as electron-selective materials because they have a small CBO with Si and good surface passivation quality. However, the use of TMOs as hole-selective contacts, resulting in a small VBO with the Si wafer, has not been widely explored. These days, MoO_x [74], WO_x [75], and related TMOs have garnered increased attention.

2.2.4 TiO_2 in c-Si solar cells

From the 1970s to the 1990s, TiO_2 was commonly used as an anti-reflective coating in the solar cell industry due to its favorable optical properties, including a refractive index of approximately 2.4 and optimal absorption in the visible range [76, 77]. In recent years, TiO_2 has gained attention as a promising alternative to SiO_2 for passivating c-Si solar cells. Through experimental analysis, it has been determined that the large band gap in the ultraviolet (UV) range and Fermi level close to the conduction band of TiO_2 enable the formation of a hole-blocking Si:TiO_2 interface [14, 78]. This interface is characterized by a small CBO (ΔE_C = 0.3 eV) and a large VBO (ΔE_V = 2.3 eV), which was measured using direct and inverse photoemission spectroscopy (PES) [79]. As a result of this band alignment, TiO_2 can form electron-selective contact, efficiently blocking holes at the interface with c-Si. The band alignments of the Si:TiO_2 interface measured from Ref. 79 are shown in Fig. 2.2. The formation of a hole-blocking interface in Si:TiO_2-based solar cells results in low dark current and series resistivity, which increases the fill factor and PCE [80]. Moreover, TiO_2 has been shown to provide excellent surface passivation quality for c-Si solar cells and has demonstrated stability in harsh environments. In n-type c-Si solar cells, TiO_2 films have achieved impressive conversion efficiencies of 23% [81] and 21.6% [63] in partial rear contact and full area contact at the rear side, respectively, indicating its huge potential for PV applications.

Various deposition techniques, including atomic layer deposition (ALD) [63] and chemical vapor deposition [79], etc, have been explored to investigate the passivation quality of TiO_2 on Si surface. Generally, experimental studies on Si:TiO_2 have aimed to produce amorphous TiO_2 due to its superior passivation qualities [63, 82]. According to the study in Ref. 82, amorphous TiO_2 thin film was found to have excellent surface passivation properties on Si, resulting in lower recombination velocity, which is beneficial for the applications in c-Si solar cells. Ref. 63 also concludes that the amorphous phase TiO_2 and the formation of Si-O-Ti bonding at the Si:TiO_2 interface achieve very good passivation quality on the Si surface at temperatures below 300°C [83]. However, for actual solar cell applications, front contact formation requires annealing at temperatures above 300 °C, which causes the degradation of surface passivation quality due to the

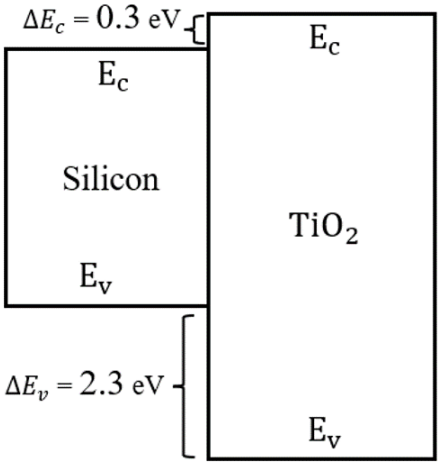
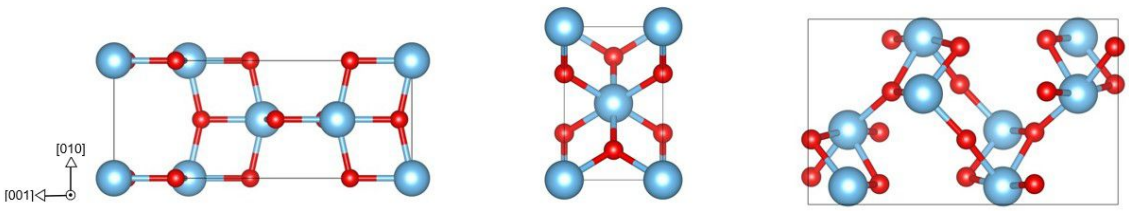


Figure 2.2: Band alignments diagram of the Si:TiO_2 interface. This figure is reproduced from Figure 1A in Ref. 79.

transformation of TiO_2 from amorphous to anatase phase, as measured by X-ray diffraction, and the breaking of Si-O-Ti bonds, which introduces more surface defects and increases recombination velocity [63, 82]. Therefore, low-temperature ALD [84] and electron-beam-processed [85] TiO_2 have been reported to avoid high-temperature substitution while maintaining good surface passivation on Si surfaces. A further interesting finding is presented in Ref. 86. The authors were able to tune the carrier selectivity of TiO_x passivating layers from electron-selective to hole-selective by reducing the oxygen content and controlling the ALD process. This versatility in carrier selectivity is attributed to the induced band bending at the c-Si:TiO_x interface [86].

2.3 Anatase and rutile TiO_2

TiO_2 exists in different crystal structure polymorphs, namely anatase, rutile, and brookite [87]. Among these, anatase and rutile are the most commonly studied forms due to their chemical stability and biologically harmless properties, making them useful as photocatalysts. Brookite, on the other hand, is the least stable phase among the three, with an orthorhombic structure that is difficult to synthesize [88]. Both rutile and anatase TiO_2 are composed of TiO_6 octahedra, where each Ti atom is surrounded by six oxygen atoms, with the space group P42/mnm and I41/amd, respectively. The conventional unit cell of rutile TiO_2 is tetragonal and contains two TiO_2 units, with a total of 6 atoms. The anatase TiO_2 cell is also tetragonal but contains four TiO_2 units, with a total of 12 atoms [89,90]. Fig. 2.3 illustrates the crystal structures of anatase, rutile, and brookite TiO_2.



(a) Anatase TiO_2 (b) Rutile TiO_2 (c) Brookite TiO_2

Figure 2.3: Polymorphs of TiO_2, (a) anatase TiO_2, (b) rutile TiO_2, (c) brookite TiO_2. O and Ti atoms are shown in red and light blue, respectively.

From a thermodynamic perspective, the rutile phase of TiO_2 is considered to be more stable than the anatase phase under all temperatures and pressures for the bulk material. However, when the size of the TiO_2 nanoparticles is smaller than 11 nm, the anatase phase becomes the most thermodynamically stable [91]. In general, the initial phase during the synthesis process is anatase, and the transformation process from anatase to rutile is strongly dependent on the synthesis parameters, such as raw materials, processing methods, and thermal treatments [92]. A bond-breaking and reforming process is involved in this transformation, which indicates this transforming process is irreversible [88].

TiO_2 is widely used as a photocatalyst due to its chemical stability, oxidizing power, and cheap cost [93]. Although the rutile phase of TiO_2 is more stable than the anatase phase, previous studies have demonstrated that anatase TiO_2 exhibits superior photocatalytic performance compared to rutile TiO_2. Experimental studies have shown that anatase TiO_2 has an indirect UV band gap of 3.2 eV, while rutile TiO_2 has a direct band gap of 3.0 eV. Semiconductors with an indirect band gap typically have a longer charge carrier lifetime than semiconductors with a direct band gap, as determined by photoconductivity measurements. Therefore, the photoexcited electrons and holes in anatase TiO_2 have a greater chance of participating in surface reactions than those in rutile TiO_2 [94]. Additionally, anatase TiO_2 has a higher surface adsorption capacity and lower charge carrier recombination rate due to its high density of localized states. On the other hand, rutile TiO_2 with large grain size shows a relatively higher recombination rate and lower ability to adsorb species [94]. Furthermore, calculations in Ref. 95 have indicated that anatase TiO_2 has a smaller average effective mass of electrons and holes compared to rutile and brookite TiO_2. The small effective mass enhances the mobility of photogenerated charge carriers, thus improving photocatalytic performance.

2.4 Experimental measurements of Si:TiO_2 band alignments

Several experimental studies have reported the measurements of band edges of isolated TiO_2 and Si in different forms. The conduction and valence band edges of TiO_2 were measured to be approximately 4 eV and 7–7.2 eV below the vacuum level, respectively [96,97]. The band edges of Si(001) were found to be 4.05 eV and 5.17 eV for the conduction and valence bands, respectively [98–100]. Based on these measurements, the conduction band and valence band offsets were calculated to be 0 eV and 2 eV, respectively, with respect to a common vacuum level. The 0 eV CBO implies that electrons can easily pass through the TiO_2 layer, while the 2 eV VBO acts as a barrier that prevents holes from moving from Si to TiO_2. The device characteristics measured for the Si:TiO_2 interface fabricated in the above studies [98–100] were found to be in agreement with the description of an electron-selective contact. Additionally, Ref. 101 and Ref. 35 have predicted very similar offsets (0 eV and 1.95 eV) based on the alignment of the charge neutrality level. It is worth noticing that reported band edge positions for TiO_2 exhibit significant variation based on the various preparation conditions. In Ref. 102, valence band positions of 7 eV below the vacuum were measured in *ex situ* preparation, while 9 eV are measured in oxidized preparation.

Several experiments have measured the band alignments at the Si:TiO_2 interface directly. By using direct and inverse PES, a CBO with a magnitude of less than 0.3 eV and a VBO with a magnitude higher than 2.3 eV are measured [79]. Ref. 80 also reported direct PES measurements Si:TiO_x ($x = 2.02$, i.e. slightly oxygen-rich) and found a reduced VBO, of $\sim$1.7 eV [14]. All these band alignments measured indicate that the energy of the conduction band of TiO_2 is higher than the energy of the Si conduction band, which forms the type I band alignment, as shown in Fig. 1.1a.

2.5 Key research questions for this thesis

Experimentally speaking, there are many parameters associated with synthesizing the Si:TiO_2 interface, such as annealing treatment, deposition method, and used precursors, resulting in systematic variation of electronic properties, such as the apparent benefits of amorphous TiO_2 compared to anatase in forming a defect-free surface [84, 85]. Therefore, understanding the systematic variation of the different parameters, characterized at the material and device level, will be crucial for further improving TiO_2-based passivating contact solar cells. However, conducting such an experiment requires significant time and resources from researchers.

First-principles calculations offer a complementary approach to investigating the interface, especially focusing on its fundamental electronic properties. Besides, although Si and TiO_2 are important functional materials, first-principles modeling of their interfacial properties is an unexplored area. So in this thesis: I have applied computational modelling techniques based on DFT to investigate the sensitivity of band alignments to the atomistic structure of the Si:TiO_2 interface. My focus is on the interfacial band alignment because it is crucial in determining the carrier selectivity and device characteristics, such as fill factor and open-circuit voltage [80]. The structural detail of the Si:TiO_2 interface is then studied through infrared calculations.

Chapter 3

First-principles methodologies

3.1 Introduction

The aim of this chapter is to provide a brief overview of the theoretical background for the calculations performed in this thesis, which use DFT with plane wave basis sets and pseudopotentials. The initial sections of this chapter review these fundamental aspects. The later section addresses the well-known "band gap problem", which is encountered during calculations in this thesis and impacts the calculated band offsets. To mitigate this problem, more advanced functionals and methods are considered. Specifically, the conventional Perdew-Burke-Ernzerhof (PBE) functional and the more advanced meta-GGA rSCAN functional are used in the calculations, and the band edge correction obtained from the hybrid functionals and the GW approximation are taken into consideration. Additionally, DFT+U calculations are performed on TiO_2, as this approach has become a popular tool for dealing with strongly correlated systems. Therefore, for the rest of the chapter, different types of functionals in Jacob's ladder are briefly introduced, followed by a review of the DFT+U approach and the GW approximation.

3.2 Density-functional theory

First-principles calculations have been widely used by researchers to predict the properties and behavior of materials. In principle, these calculations involve solving the Schrödinger equation, $\hat{\mathcal{H}}\Psi = E\Psi$, to determine the ground-state energy of the system [103, 104]. For a system containing both electrons and nuclei, the time-independent many-body Schrödinger equation can be expressed in atomic Hartree units as:

$$\left[-\sum_i \frac{\nabla_i^2}{2} - \sum_I \frac{1}{M_I}\frac{\nabla_I^2}{2} - \sum_{i,I} \frac{Z_I}{|\mathbf{r}_i - \mathbf{R}_I|} + \frac{1}{2}\sum_{i,j\neq i} \frac{1}{|\mathbf{r}_i - \mathbf{r}_j|} + \frac{1}{2}\sum_{I,J} \frac{Z_I Z_J}{|\mathbf{R}_I - \mathbf{R}_J|}\right]\Psi = E\Psi \tag{3.1}$$

The first term in the bracket is the total electronic kinetic energy; the second term is the total nuclei kinetic energy; the third term is the attractive Coulomb potential between the electrons and the nuclei; the fourth term is the Coulomb repulsion between electrons; and the last term is the Coulomb repulsion between nuclei. The spatial coordinates of the electrons and nuclei are denoted by $\mathbf{r}_i$, $\mathbf{r}_j$ and $\mathbf{R}_I$, $\mathbf{R}_J$, respectively. The atomic number of the nucleus I is represented by $\mathbf{Z}_I$, and the mass of the nuclei is represented by $\mathbf{M}_I$ [104, 105].

Solving the many-body Schrödinger equation to find the eigenstate with the lowest energy would correspond to finding the ground state of the system. From this, many material properties can be calculated, such as electronic and elastic properties. However, solving such an equation is incredibly expensive and challenging. Under the Born-Oppenheimer approximation in which the nuclear motion and electron motion are separated into different mathematical problems, the total wavefunction Ψ in Equation 3.1 can be expressed as the product of the electronic and nuclear wavefunctions, denoted as $\Psi_{\text{tot}} = \Psi(\mathbf{r}_1, \mathbf{r}_2, \ldots, \mathbf{r}_N)\,\Phi(\mathbf{R}_1, \mathbf{R}_2, \ldots, \mathbf{R}_M)$, where N and M represent the numbers of electrons and nuclei, respectively [106]. To simplify the equation and use the fact that the mass of nuclei is much higher than electrons (assuming $\mathbf{M}_I = \infty$), the nuclei are considered static with respect to the motion of the electrons. This approximation neglects the kinetic energy of the nuclei and treats Coulomb repulsion between nuclei as a constant [107]. If the positions of the M nuclei are known, the ground-state energy can be expressed as a function of their positions, $E(\mathbf{R}_1, \mathbf{R}_2, \ldots, \mathbf{R}_M)$. Thus, the Schrödinger equation that describes the electrons is given by:

$$\left[-\sum_i \frac{\nabla_i^2}{2} + \sum_i V_n(\mathbf{r}_i, \{\mathbf{R}_I\}) + \frac{1}{2}\sum_{i,j\neq i} \frac{1}{|\mathbf{r}_i - \mathbf{r}_j|}\right]\Psi(\mathbf{r}_1, \mathbf{r}_2, \ldots, \mathbf{r}_N) = E\Psi(\mathbf{r}_1, \mathbf{r}_2, \ldots, \mathbf{r}_N) \tag{3.2}$$

$V_n(\mathbf{r}_i, \{\mathbf{R}_I\}) = -\sum_I \frac{Z_I}{|\mathbf{r}_i - \mathbf{R}_I|}$ represents the Coulomb potential experienced by electrons due to the nuclei, while the Coulomb repulsion between nuclei is included in the total energy E. However, solving this equation for more than one electron is still challenging due to the electron-electron interactions. One approach to simplify the problem is to use the independent electron

approximation, where the electron wavefunction Ψ is treated as a product of individual electron wavefunctions but the Coulomb repulsion between electrons is ignored. To take this Coulomb repulsion into consideration while maintaining the single-particle description, one could use a mean-field approximation, which considers the Coulomb repulsion between electrons described in terms of the Hartree potential [108]:

$$V_{\mathrm{H}}(\boldsymbol{r}) = \int d\boldsymbol{r}' \frac{n\left(\boldsymbol{r}'\right)}{|\boldsymbol{r} - \boldsymbol{r}'|} \tag{3.3}$$

where $n(\mathbf{r}')$ represents the charge density, and V_{H} represents the average potential experienced by each electron. By using the mean-field approximation, all individual interactions between electrons are replaced with a single, averaged interaction. However, the Hartree potential overestimates the Coulomb repulsion between electrons due to the Pauli exclusion principle, which states that electrons can not be too close to each other. Furthermore, the Hartree potential does not consider the effects of electron motion on other electrons.

DFT has become one of the most widely used methods for calculating the properties of materials. It is based on mathematical theorems established by Kohn and Hohenberg [109], as well as a set of equations developed by Kohn and Sham in the mid-1960s [110]. Kohn and Hohenberg's theorems state that the ground-state energy of a system is a unique functional of the electron density:

$$E_0 = E_0[n] \tag{3.4}$$

This theorem states that electron density n is sufficient to calculate the total energy E of a system in its ground state [109]. However, the functional $E_0[n]$ that relates the density to the energy is unknown. Kohn and Sham later addressed this issue by proposing a way to find the electron density by solving a set of equations in which each equation only involves a single electron [110]. The electron density is described as:

$$n(\mathbf{r}) = \sum_i |\psi_i(\mathbf{r})|^2 \tag{3.5}$$

Following Kohn and Hohenberg's theorems, the Kohn-Sham equations are described as follows:

$$\left[-\frac{1}{2}\nabla^2 + V_n(\mathbf{r}, \{\mathbf{R}_I\}) + V_H(\mathbf{r}) + V_{xc}(\mathbf{r})\right] \psi_i(\mathbf{r}) = \varepsilon_i \psi_i(\mathbf{r}) \tag{3.6}$$

$\psi_i(\mathbf{r})$ are the single electron wavefunctions with corresponding single electron eigenvalues ε_i. The kinetic energy is represented by $-\frac{1}{2}\nabla^2$. V_n is potential of nuclei experienced by electrons; V_{H} is the Hartree potential. The remaining interaction in the system is described by the exchange-correlation potential V_{xc}, which can be determined as a functional derivative of the exchange-correlation energy:

$$V_{xc}(\mathbf{r}) = \frac{\delta E_{xc}[n]}{\delta n(r)} \tag{3.7}$$

The exchange-correlation energy contains all remaining energy not included in the kinetic and potential terms. The true form of the exchange-correlation energy is not known and must be approximated instead. More detail about the exchange-correlation energy is present in Section 3.6.

The Kohn-Sham equations can be solved through a self-consistent process involving a trial electron density obtained from isolated atoms for example. The trial density is used to solve the Kohn-Sham equations, which yield single-particle wavefunctions. The resulting electron density obtained using Equation 3.5 is compared to the trial density, and if they match, the ground-state electron density has been found. If the densities do not match, the process is repeated using the new electron density as the trial density until the calculated density matches the old density [104, 107].

3.3 Plane wave basis set

If the nuclei are arranged in a periodic pattern, the potential must be periodic with the form of $V(\mathbf{r} + \mathbf{L}) = V(\mathbf{r})$, where L is a real space lattice vector. In terms of the wavefunction, Bloch's theorem states that the single electron wavefunction for a periodic potential must be quasi-periodic in which the wavefunction translated by any lattice vector will be the same wavefunction multiplied by a phase factor. The explicit form of electron wavefunction can be expressed as a product of a phase factor $\exp(ik{\cdot}\mathbf{r})$ and a function $u_{\nu k}(\mathbf{r})$ that is periodic in space with the same periodicity as the unit cell [111]:

$$\psi_{\nu k}(\mathbf{r}) = \exp(ik \cdot \mathbf{r}) u_{\nu k}(\mathbf{r}) \tag{3.8}$$

Unlike the electron wavefunction $\psi_i(\mathbf{r})$ in Equation 3.6 which is labeled by the number of the electron in the system, the $\psi_{\nu k}(\mathbf{r})$ is labeled by the band index ν and the Bloch wavevector k which lies within the first Brillouin zone. $u_{\nu k}$ is periodic in space and can be expanded in terms of plane waves after doing a Fourier transform:

$$u_{\nu k}(\mathbf{r}) = \sum_{G} c_{\nu k+G} \exp[iG \cdot \mathbf{r}] \tag{3.9}$$

where G denotes the reciprocal lattice vectors, $G = m_1\mathbf{b}_1 + m_2\mathbf{b}_2 + m_3\mathbf{b}_3$ with m_i being integers. The $c_{\nu k+G}$ quantities are the coefficients of the Fourier transform. By combining Equations 3.8 and 3.9, the wavefunction using the plane wave basis set can be written as:

$$\psi_{\nu k}(\mathbf{r}) = \sum_{G} c_{\nu k+G} \exp[i(k+G)\mathbf{r}]. \tag{3.10}$$

Many packages, such as CASTEP [112], have used this plane wave method as the basis set in the code. However, there are an infinite number of possible reciprocal lattice vectors G. To reduce the computational cost of the calculations, the plane wave cutoff energy E_{cut}, which can be interpreted as the kinetic energy associated with the largest reciprocal space vector used to describe the wavefunction, is introduced. The cutoff energy is given as:

$$\frac{1}{2}\left|k+G\right|^2 \leq E_{cut} \tag{3.11}$$

In practical calculations, increasing the cutoff energy and Brillouin zone sampling (k-point sampling) will increase the accuracy of calculations, but also need more computational resources [104, 107]. Therefore, it will be beneficial to do a convergence test over a range of cutoff energy and k-point sampling to find the optimal value that can converge specific properties of materials with a certain tolerance. The convergence tests for materials used in this thesis are discussed in later sections.

3.4 Pseudopotentials

The spatial distribution of electron density shows that core electrons, which are tightly bonded to the nucleus, play a less important role in explaining chemical bonding and other material properties. On the other hand, the valence electrons, which are less tightly bound to the nucleus, are crucial in defining these properties [113]. As a result, in DFT calculations, the wavefunctions of core electrons are often considered "frozen" as they appear in an isolated atom. This approach reduces the computational cost by not specifically describing the wavefunctions of core electrons as they have minimal impact on the calculated properties. Since different eigenstates of the Hamiltonian have to be orthogonal to each other, valence wavefunctions oscillate rapidly near the nucleus

to maintain this orthogonality with the core electrons. Therefore, it is difficult to accurately describe this oscillation unless using higher energy cutoffs. To mitigate the computational cost, a smooth pseudo-wavefunction is often used to replace the oscillating part of the valence wavefunction, as proposed in pseudopotential methods [107]. The pseudo-wavefunction should yield identical valence electron wavefunctions outside the core region, while inside the core region it needs to be smoother and avoid nodal structures compared to the original wavefunction [104].

The transferability of pseudopotentials is a key requirement in DFT calculations. A pseudopotential is generated from an isolated atom of a specific element, but once constructed, it should ideally be usable in calculations involving that atom in any chemical environment, without the need for further modifications. There are various types of pseudopotentials. Norm-conserving pseudopotentials [114] are one example of widely known and used pseudopotentials. The idea of norm-conserving pseudopotentials is that the total integrated charge density within the core region given by real wavefunctions and pseudo wavefunctions must be identical. This requirement results in sharply peaked orbitals particularly for first row elements (O, N, C, etc.), which can require a large number of plane waves for convergence in DFT calculations. One way to produce a smoother pseudo-wavefunction is to use ultrasoft pseudopotentials developed by Vanderbilt [115]. Ultrasoft pseudopotentials have relaxed the norm-conserving constraint and made it more flexible to create pseudo-wavefunction inside the core region, but also lead to a deficit of charge density. Augmentation of the density is applied in a more efficient way to make sure the density is corrected. Equations 18, 19, and 20 in Ref. 115 provide more specific detail about this augmentation. Ultrasoft pseudopotentials are used in this thesis because they require relatively lower cutoff energies than other pseudopotentials and have been widely tested.

3.5 "Band gap problem"

The underestimation of the band gap is a well-known limitation in DFT calculations, and it can also affect the accuracy of other properties such as band alignments and optical properties. In Kohn-Sham DFT calculations, the band gap, $E_{\mathrm{g}}^{\mathrm{KS}}$, is determined as the smallest difference between the unoccupied and occupied Kohn-Sham eigenvalues. The band gap measured by the experiment is called the quasiparticle band gap, $E_{\mathrm{g}}^{\mathrm{qp}}$. In a solid-state system that has a large number of electrons, the change in electron density will be negligible when adding or removing an electron, as well as the Hartree potential. However, the exact exchange-correlation potential will show a discontinuous

jump even though the change in electron density is infinitesimally small, resulting in changing in exchange-correlation energy. The constant energy Δ_{xc} is the difference between the quasiparticle band gap and the Kohn–Sham band gap of a solid [116]. The quasiparticle gap can be expressed as:

$$\lim_{\Delta n \to 0} E_{\mathrm{g}}^{\mathrm{qp}} = E_{\mathrm{g}}^{\mathrm{KS}} + \Delta_{xc} \tag{3.12}$$

If the exact exchange-correlation functional is used, the value of Δ_{xc} will be non-zero [104]. However, the exact exchange-correlation functional is not known. Widely used functionals, like the local density approximation (LDA) [117, 118] and generalized gradient approximation (GGA) [119, 120], have a derivative discontinuity that is equal to zero ($\Delta_{xc} = 0$) for solids. Therefore, they can not produce the correct quasiparticle gap. Many approaches have been developed to improve the accuracy of predictions for band gaps. For example, more advanced methods like the GW approximation [121, 122] or hybrid functionals [123, 124] can overcome this problem. Still, these calculations also require significantly larger computational resources, mainly when calculating complicated and large-scale systems.

3.6 Jacob's ladder

The Kohn-Sham equations show that the ground state energy can be calculated by self-consistently solving a set of single-particle equations. The exchange-correlation functional plays a crucial role in accurately solving the Kohn-Sham equations. Various functionals have been developed and can be categorized based on increasing accuracy and computational cost, following a scheme known as the Jacob's ladder, as shown in Fig. 3.1.

3.6.1 Local density approximation

Kohn and Sham introduced an approximation where the exchange-correlation energy at every position is assumed to be equal to the exchange-correlation energy of a homogeneous electron gas with the same density at that position [109]. Building upon this concept, a functional has been constructed in terms of energy density in a homogeneous electron gas situation. The energy of this functional is given by:

$$E_{\mathrm{xc}}[n] = \int n(\mathbf{r}) \epsilon_{\mathrm{xc}}(n(\mathbf{r})) d\mathbf{r} \tag{3.13}$$

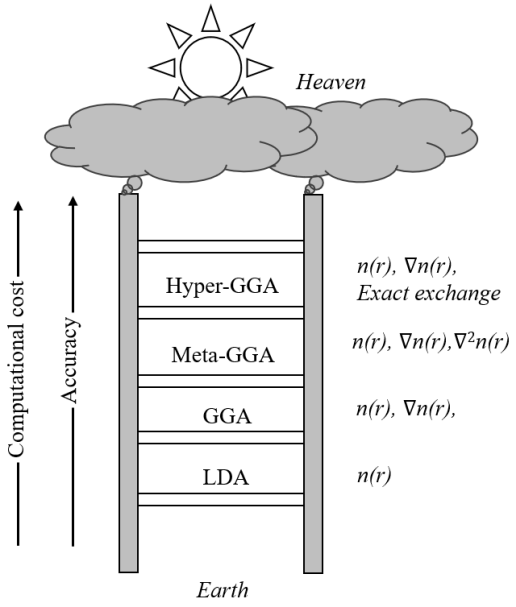


Figure 3.1: Classification of DFT functionals described using Jacob's ladder. This figure is reproduced from Figure 10.2 in Ref. 107

This functional, known as the LDA functional, only depends on the local density $n(\mathbf{r})$. This approximation of the exchange-correlation energy is also applied to the exchange-correlation potential [104], which is given as:

$$V_{\mathrm{XC}}(\mathbf{r}) = V_{\mathrm{XC}}^{\text{electron gas}}\left(n(\mathbf{r})\right) \tag{3.14}$$

The LDA functional is a widely used exchange-correlation functional in DFT calculations because of its relatively low computational cost and reasonable accuracy. It is possible to calculate the exchange energy of the homogeneous electron gas exactly, while the correlation energy can be calculated numerically and parameterized very accurately [118]. However, when calculating some properties in bulk solids, the LDA accuracy is limited by the assumption that the electron density is uniform throughout a material. In reality, the electron density in materials can vary significantly due to diverse chemical characteristics [107].

3.6.2 Generalized gradient approximation

More complex approximations have been developed to address the uniform density constraints in LDA. One important type of functional is the GGA. The GGA functionals take into account the spatial variation of electron density as well as the density at that point itself, which is expressed as:

$$E_{\mathrm{xc}}^{\mathrm{GGA}}[n] = \int n(\mathbf{r})\epsilon_{\mathrm{xc}}(n(\mathbf{r}), \nabla n(\mathbf{r}))d\mathbf{r} \tag{3.15}$$

$\nabla n(\mathbf{r})$ is the gradient of the electron density. There are many distinct GGA functionals because there are various ways to use the information from the gradient of the electron density [107, 119, 120]. PBE is one of the most widely used GGA functionals. In this thesis, most of the calculations are performed using the PBE functional because PBE is expected to be more accurate than LDA. For example, the calculated atomization energies of various solids using PBE yielded smaller error percentages than using the LDA functional compared to experimental values [125]. However, this is not always the case. The actual accuracy of both functionals depends on the specific system. For instance, the calculated lattice constants of AlP, AlAs, and GaAs using LDA are closer to experimental results than PBE [125].

3.6.3 The DFT+U method

The LDA and GGA functionals often underestimate the band gap of semiconductors and inaccurately describe the electronic structure of strongly correlated materials [126]. Using DFT+U (LDA+U or GGA+U) corrections on strongly correlated electronic states is one approach to reduce the "band gap problem" [127]. Specifically, in the Kohn-Sham equations (Equation 3.6), the Hartree potential (Equation 3.3) represents the Coulomb repulsion between the electron and the total electron density defined by all electrons. Part of the Hartree potential involves Coulomb interaction between the electron and itself because the electron used in the Kohn-Sham equations is included in the total electron density. This self-interaction error is not fully cancelled by the approximate exchange-correlation functionals, such as LDA and PBE, which causes the highly localized orbital to be less stable. The idea of the DFT+U method is inspired by the Hubbard model [128], which describes the transition between metal and insulator, and tends to improve the description of the ground state of correlated systems [107]. The Hubbard model includes the Coulomb repulsion between electrons at the same atomic orbitals, which is also called on-site repulsion. The simple form of the Hubbard Hamiltonian is given as:

$$H_{Hub} = t \sum_{\langle i,j\rangle,\sigma} \left(c_{i,\sigma}^{\dagger} c_{j,\sigma} + \text{ h.c. } \right) + U \sum_{i} n_{i,\uparrow} n_{i,\downarrow} \tag{3.16}$$

The first term is kinetic energy which describes the electron creation with spin σ on atomic site i and the destruction of the electron on atomic site j. The first term is also known as the hopping

term, and t is the hopping amplitude. When the electrons are strongly localized, they can not move freely between atomic sites rather than jump between adjacent atomic sites. The second term is the interaction energy with the term U that describes Coulomb repulsion between electrons at the same atomic orbitals [126].

The basic concept of U correction in DFT is to add the second interaction term in the above equation to the on-site Coulomb interaction of localized electrons. This additional Hubbard model is usually applied to the strongly correlated electronic states, such as d and f orbitals. The rest of the electronic states are treated by the original DFT approximation. With the DFT+U method, the total energy functional is modified [129, 130] and written as:

$$E_{DFT+U}[n(\mathbf{r})] = E_{DFT}[n(\mathbf{r})] + E_{Hub}\left[n_m^{I,\sigma}\right] - E_{dc}\left[n^{I,\sigma}\right] \tag{3.17}$$

E_{DFT} is the total energy of the system calculated using the LDA or GGA functionals. $n(\mathbf{r})$ is the electron density, and $n_m^{I,\sigma}$ represents the atomic orbital occupations for correlated atom I. σ is the spin of this atom. E_{Hub} represents the Coulomb repulsion between the on-site orbitals. Some of the Coulomb repulsion in E_{Hub} have already been counted in the DFT part of the total energy functional, so the double-counting term, E_{dc}, must be removed [126, 131].

In practical calculations, the strength of the on-site interactions is determined by the on-site Coulomb term U of two electrons at the same orbital. The numerical value of the U needs to be specified in order to use DFT+U. There are two approaches to determining the value. The first approach is to choose a well-known property of a material and to test what value of U gives the most similar result to the selected property. The second approach uses other $ab\ initio$ calculations that are feasible to estimate U [107]. This Hubbard U correction can be added to the local and semi-local density functionals, giving the LDA+U and GGA+U methods. The implementation of the DFT+U method can be done in various ways. For example, CASTEP implemented the DFT+U method following the approach in Ref. 130 and Ref. 132. The only external parameter required for doing DFT+U calculations in CASTEP is the effective value of the on-site Coulomb parameter, U, for each relevant orbital [112]. Additionally, unlike the hybrid functionals and the GW approximation that require numerous computational resources, the computational cost of DFT+U is only slightly higher than normal DFT calculations.

3.6.4 Meta-generalized gradient approximation

Unlike the GGA functionals, which consider the electron density $n(\mathbf{r})$ and electron gradients $\nabla n(\mathbf{r})$ in calculations, meta-GGA includes an additional term known as the Laplacian (second derivative) of the electron density, $\nabla^2 n(\mathbf{r})$. In practice, the kinetic energy density $\tau(\mathbf{r})$ of the Kohn-Sham orbitals has the same information as the Laplacian of the electron density, but makes the exchange-correlation functional more flexible and numerically more stable [107]. The kinetic energy density is defined as the summation over all occupied Kohn-Sham orbitals $\varphi_i(\mathbf{r})$:

$$\tau(\mathbf{r}) = \frac{1}{2} \sum_{\text{occupied states}} |\nabla \varphi_i(\mathbf{r})|^2 \tag{3.18}$$

The mathematical form of the meta-GGA functionals is given as:

$$E_{\text{xc}}^{\text{GGA}}[n] = \int n(\mathbf{r}) \epsilon_{\text{xc}}(n(\mathbf{r}), \nabla n(\mathbf{r}), \tau(\mathbf{r})) d\mathbf{r} \tag{3.19}$$

In general, the meta-GGA functionals provide more accurate results compared with the LDA and GGA functionals. However, the self-interaction error mentioned in Section 3.6.3 still exists in the meta-GGA functionals. The computational cost of using the meta-GGA functionals is also higher. One version of the meta-GGA functional is the Strongly Constrained and Appropriately Normed (SCAN) functional, which satisfies all the known constraints that a meta-GGA functional can fulfill. The SCAN functional has been used to study different properties of materials in recent years and has proven to provide relatively accurate total energies of atoms and molecules [133]. For example, the SCAN functional can accurately describe the electronic and dynamic properties of liquid water [134]. Systematic improvements are shown when using SCAN to calculate electronic structure properties of thin-film materials [135].

In this thesis, I am primarily focusing on the newly developed meta-GGA functional rSCAN by Bartók and Yates [41]. rSCAN is developed to retain the accuracy and improve the stability of SCAN. More information about rSCAN and the calculated results using rSCAN in this thesis are given in Chapter 5.

3.6.5 Hybrid functional

A different approach to reducing the "band gap problem" in DFT calculations is using more advanced and expensive functionals like hybrid functionals [123, 124]. Hybrid functionals incorpo-

rate a fraction of the exact nonlocal Hartree-Fock exchange. This exact nonlocal Hartree-Fock exchange can be written as:

$$E_X = -\frac{1}{2}\sum_{\nu_i,\nu_j,\sigma}^{N}\iint \frac{\psi^*_{\nu_i,\sigma}(\mathbf{r}_1)\,\psi^*_{\nu_j,\sigma}(\mathbf{r}_2)\,\psi_{\nu_j,\sigma}(\mathbf{r}_1)\,\psi_{\nu_i,\sigma}(\mathbf{r}_2)}{r_{12}} d\mathbf{r}_1 d\mathbf{r}_2 \tag{3.20}$$

r_{12} is equal to $|\mathbf{r_1} - \mathbf{r_2}|$. $\psi_{\nu_i,\sigma}(\mathbf{r})$ represents the Kohn–Sham one-electron orbitals. The symbol ν represents a composite index that labels the band index and wavevector. σ is the spin index. N is the number of occupied orbitals [136]. Based on Equation 3.20, the Hartree-Fock exchange is not dependent on density; instead, it depends on Kohn–Sham orbitals. Furthermore, the Hartree-Fock exchange is nonlocal, which means it can not be described at one specific location unless electron wavefunctions are known at all locations. [137, 138].

A hybrid exchange-correlation functional is a linear combination of this Hartree-Fock exchange and other exchange and correlation functionals, such as LDA and GGA. The hybrid GGA functionals have the form:

$$E_{xc}^{\text{hybrid}} = E_{xc}^{GGA} + \alpha(E_x^{\text{HF}} - E_x^{GGA}) \tag{3.21}$$

α is the mixing coefficient that determines the fraction of exact exchange included in the functional. The value of α is typically chosen to be around $\frac{1}{4}$, which produces reasonable results for a wide range of systems [139]. E_{x}^{HF} is the Hartree-Fock exchange energy, and $E_{\text{x}}^{\text{GGA}}$ is the GGA exchange energy [140, 141]. In general, the results obtained using the hybrid functionals are more accurate than the local and semilocal functionals [38]. Still, the computational cost of using the hybrid functionals is much higher than using the LDA or GGA functionals.

3.6.6 GW approximation

In the DFT approach, the approximation of the unknown exchange-correlation potential of the Kohn-Sham equations leads to undesirable calculation results for some properties, and the energies in the Kohn-Sham equations are not meant to be the true energy levels of electrons. One approach to solving these problems is using the GW method [122]. The name "GW" represents an approximation of the self-energy, which is a nonlocal effective potential dependent on frequency. The G stands for Green's function, which describes the propagation of particles in an interacting system. W stands for the screened Coulomb interaction. The self-energy is expressed as a product of the

Green's function and the screened Coulomb interaction. The exchange and correlation potential in Equation 3.6 can be replaced by the self-energy, denoted by Σ. The quasiparticle energies $E_{\nu k}$ calculated using the GW approximation is defined as [142]:

$$E_{\nu k} = \varepsilon_{\nu k} + Z_{\nu k} \left\langle \psi_{\nu k} \left| \Sigma \left(\varepsilon_{\nu k} \right) - V_{xc} \right| \psi_{\nu k} \right\rangle \tag{3.22}$$

V_{xc} is the exchange and correlation potential. $Z_{\nu k}$ represents the associated quasiparticle renormalization. ν and k are the band index and wavevector, respectively, corresponding to eigenvalues ε and Kohn-Sham eigenstates ψ. The self-energy Σ correction includes the finite discontinuity Δ_{xc} in Equation 3.12, so the accurate quasiparticle band gap can be calculated using the GW approximation [104]. The GW approximation is currently very popular when calculating the band structure of solids since it provides the best solution to the DFT "band gap problem". However, the computational cost of using the GW approximation is extremely high, limiting its applications in complicated systems. It is also worth mentioning that Equation 3.22 provides a link between the quasiparticle energy and the Kohn-Sham energy, with the second term representing the correction. Therefore one approach, which is employed in this thesis, is to calculate this correction for a simpler bulk system and apply it to the more complicated system.

Chapter 4

DFT calculations in this thesis

4.1 Introduction

In this thesis, two methods have been used to calculate the band alignments of the Si:TiO_2 interface, referred to as the vacuum-level alignment method and the heterointerface alignment method. In the vacuum-level alignment method, energy levels of separate materials are aligned to a common vacuum level. The heterointerface alignment method takes into account the potential variation across the heterointerface model. This chapter first provides an overview of these two methods along with example calculations. Then, the finite displacement method and dynamical matrix that are used to calculate the infrared spectra are briefly discussed.

4.2 Calculating band alignments

4.2.1 The vacuum-level alignment method

The vacuum-level alignment method involves aligning the VBM and CBM against the vacuum level using the ionization potential (IP) and electron affinity (EA). IP and EA are the difference between the vacuum level and the VBM/CBM in the bulklike region located far from the surface. These values are associated with atomic structure, surface orientation, and surface contamination. They can be calculated using a slab model composed of a bulk and vacuum region. In the idealized slab model, the calculated planar-averaged Kohn-Sham potential exhibits oscillatory behavior in the bulk-like region about a value denoted as $\varepsilon_{\mathrm{Ref}}$, and reaches a plateau within the vacuum region, representing the vacuum level, denoted as $\varepsilon_{\mathrm{Vac}}$.

The procedure for calculating band alignments involves first obtaining the energy difference

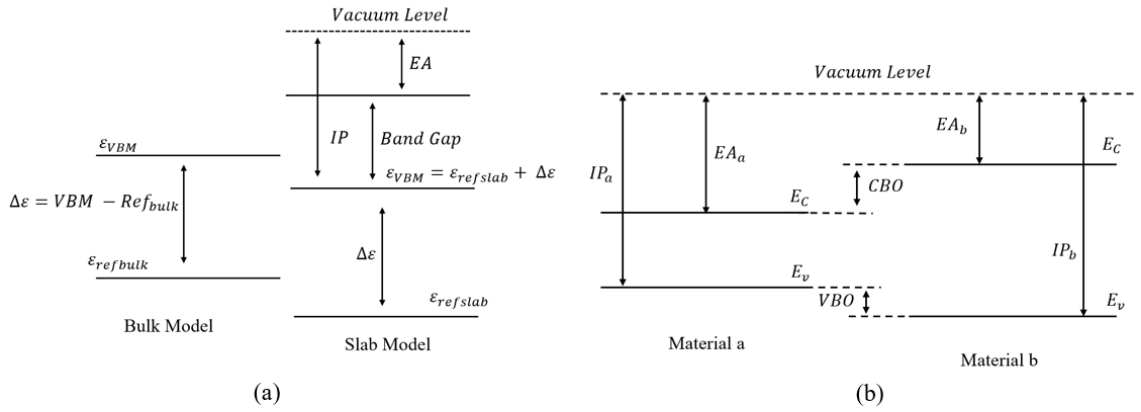


Figure 4.1: (a) Schematic diagram for determining IP and EA using bulk and slab models. (b) Schematic diagram for VBO and CBO of materials a and b calculated by using the vacuum-level alignment method.

between the VBM and the macroscopic average of the Kohn-Sham potential using a bulk model. This energy difference is then added to the Kohn-Sham potential of the bulk-like region in the slab model, resulting in a new VBM. The IP can then be determined by calculating the energy difference between the vacuum level and this new VBM. The EA is obtained by subtracting the band gap calculated in bulk from the IP. Fig. 4.1a illustrates the schematic diagram for determining IP and EA using bulk and slab models. The VBO and CBO are generally the difference between the IP and EA of the two materials, respectively, shown in Fig. 4.1b. In this thesis, this method is referred to as the vacuum-level alignment method [38].

During calculations, the planar average of the Kohn-Sham potential within the bulk-like region of the slab model exhibits periodic oscillations in the direction perpendicular to the surface, which is the z-axis in this case. It is difficult to determine a single value used as the reference potential with these oscillations. Therefore, the macroscopic average method is applied to remove these oscillations:

$$\bar{\bar{V}}(z) = \frac{1}{L}\int_{-L/2}^{L/2} \bar{V}(z)dz \tag{4.1}$$

$\bar{V}$ is the planar average of electrostatic potential; L is the length of the period of oscillation along the z-axis [139]. Fig. 4.2 shows an example of the calculated planar and macroscopic average potential of the Si slab terminated with hydrogen atoms.

The estimation of the VBO $\Delta\varepsilon_{\mathrm{IP}}^{\mathrm{a-b}}$ using the vacuum-level approach is described as:

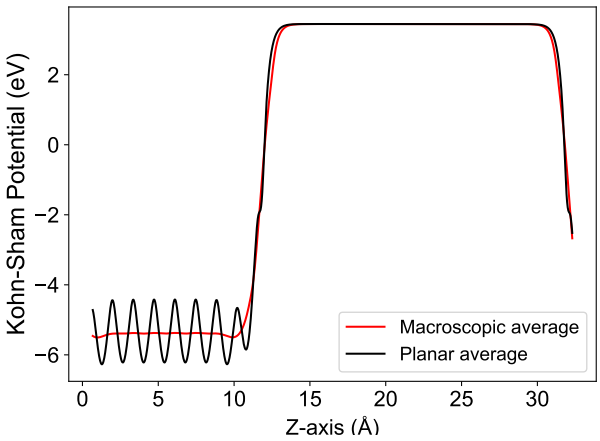


Figure 4.2: Calculated planar (black) and macroscopic average (red) potential of the Si slab terminated with hydrogen atoms.

$$\Delta E_{\mathrm{IP}}^{\mathrm{a-b}} = \left(\Delta\varepsilon_{\mathrm{VBM-Ref}}^{\mathrm{a}} - \Delta\varepsilon_{\mathrm{Vac-Ref}}^{\mathrm{a}}\right) - \left(\Delta\varepsilon_{\mathrm{VBM-Ref}}^{\mathrm{b}} - \Delta\varepsilon_{\mathrm{Vac-Ref}}^{\mathrm{b}}\right) \tag{4.2}$$

$\Delta\varepsilon_{\mathrm{VBM-Ref}}$ is the energy difference between the VBM and macroscopic average of reference potential obtained from bulk calculation. $\Delta\varepsilon_{\mathrm{Vac-Ref}}$ represents the energy difference between the macroscopic average of reference potential in the vacuum region and the bulk-like region obtained from the slab calculation [143]. Since only bulk and slab calculations are needed to obtain the band alignments in this approach, the computational cost for doing such calculations is relatively small compared with the heterointerface approach in which a heterointerface calculation is involved, discussed in Section 4.2.2 below. In addition, certain interfaces such as anatase TiO_2(001):$SrTiO_3$(001) have been found to show reasonable agreement between calculated band offsets using the vacuum-level method and experimental results [144]. However, the correct band offset is not always guaranteed. For instance, the calculated VBO of TiO_2(001):ZnO(11$\bar{2}$0) using this approach is inconsistent with experimental results, according to Ref. 145. It is important to note that the vacuum-level approach does not consider potential interface effects or bonding types between two materials.

4.2.2 The heterointerface alignment method

Ideally, the accurate determination of band alignments is based on heterointerface calculations because heterointerface structures can provide a relatively realistic representation of the interface between two different materials, which can possibly reduce the impact of the termination effects

that occurred at the interface. Unlike the vacuum-level alignment method, the variation of Kohn-Sham potential across the heterointerface is used as the reference potential.

Similar to the vacuum-level alignment method, the first step to calculate band alignments is to perform a bulk calculation on each material to determine the VBM and CBM with respect to the macroscopic average of Kohn-Sham potential. The second step is to determine the alignment of the macroscopic average of Kohn-Sham potential in the bulk-like region of each material by conducting heterointerface calculations. In this thesis, the heterointerface models were constructed by placing the material a slab on top of the material b slab, and a large vacuum region was used to separate periodic replicas and reduce the dipole effects. In this way, only one particular interface was formed and considered in the calculation, which reduced the computational cost. It is worth noticing that the interface model constructed here is not intended to be a realistic representation of the actual interface in the experimental study, where multiple layers of materials are formed together with a significantly large thickness. The macroscopic average of Kohn-Sham potential should reach a plateau value in the bulk-like region for each material, as well as in the vacuum region. By combining the bulk calculation and the heterointerface calculation, the theoretical prediction of band alignments of two semiconductors can be achieved [139].

The construction of heterointerfaces presents certain challenges, such as lattice mismatch and incoherent structures, which will induce strain on the two constituent semiconductors [38]. For example, heterostructures are denoted as $a : b$, where material b is overlaid on material a. As material a serves as the substrate, calculations are performed based on its relaxed lattice constants. Material b, on the other hand, is calculated using the strained lattice constants, as its in-plane lattice parameter is fixed to that of material a. Still, the out-of-plane lattice parameter is allowed to relax. The strained VBO ΔE_v is defined as:

$$\Delta E_v = \left(E_v^b - E_v^a\right) + \Delta V \tag{4.3}$$

The VBM with respect to the macroscopic average of Kohn-Sham potential of materials a and b are denoted by E_v^a and E_v^b, respectively. The Kohn-Sham potential difference of the two materials calculated from the heterointerface calculation is represented by ΔV. The corresponding CBO can be determined by using the band gaps calculated from bulk calculations [139, 146]. In Ref. 145, the VBO of TiO_2(001):ZnO(11$\bar{2}$0) was also calculated using the heterointerface alignment method, providing a consistent VBO to the experimental value. The band offsets of

TiO_2(001):$SrTiO_3$(001) obtained using the heterointerface alignment method are similar to those obtained using the vacuum-level alignment method in Ref. 144 and consistent with experimental results as well.

While reasonable band offsets have been obtained using the heterointerface alignment method as compared to experimental values and vacuum-level alignments, the computational cost of using the heterointerface alignment method is significantly higher than that of the vacuum-level alignment method. The vacuum-level alignment method only involves using bulk and slab calculations and does not require a specific description of the structural details of the actual interface, which requires fewer computational resources to perform. However, in experimental studies, the interface formed with various interfacial bonding may screen electric dipoles, resulting in a different band alignment. Therefore, in certain cases, the heterointerface calculation is required to achieve accurate band offsets.

4.3 Calculating infrared spectroscopy

4.3.1 Introduction

In this thesis, the primary focus has been on investigating the sensitivity of band alignments to different structural features of the Si:TiO_2 interface. With several Si:TiO_2 interface models constructed, infrared spectra were then calculated to study the structural feature of this interface, present in Chapter 7. The calculated vibrational frequencies will act as a reference point to help experimentalists to identify the particular structures in their Si:TiO_2 interface. Here, the finite displacement method and the dynamical matrix used to calculate infrared spectra are briefly discussed.

4.3.2 Finite displacement method

The principle of infrared spectroscopy is to measure the specific infrared radiation absorbed when infrared light shines on a sample, which can be used to characterize the corresponding structure of the materials. The remaining light passes through the sample and is received by a detector. The detector detects the transmitted frequencies, which can also provide the values of the frequencies being absorbed [147]. In particular, with its ability to provide the structural and vibrational properties of the analyzed material, infrared spectroscopy has become a widely used analytical tool for characterizing thin films and investigating interfaces [148]. In this thesis, the infrared spectra of

slabs and interface models are calculated using the Quantum ESPRESSO package [149] with the finite displacement method implemented in the $Phonopy$ package [150, 151].

The atomic vibration involves a very small displacement from the equilibrium position of the nuclei. If the nuclei are treated as classical objects, the equation of motion described by Newton's second law is given as:

$$M\frac{\partial^2 u_n}{\partial t^2} = -\frac{\partial U}{\partial u_n} \tag{4.4}$$

u is the atomic displacement of the atom n. U is the total potential energy. It is possible to approximate the U of a solid or molecular using a Taylor expansion if the displacement u is small, denoted as:

$$U\left(\mathbf{R}_1,\ldots,\mathbf{R}_M\right) = U\left(\mathbf{R}_1^0,\ldots,\mathbf{R}_M^0\right) + u_{I\alpha}\frac{\partial U}{\partial R_{I\alpha}} + \frac{1}{2}\frac{\partial^2 U}{\partial R_{I\alpha}\partial R_{J\beta}}u_{I\alpha}u_{J\beta} + ... \tag{4.5}$$

The $R_{J\beta}$ represents the coordinate of the Jth nucleus along β direction ($\beta = x, y, z$). The first term on the right side is the potential energy at a particular point, and the second term is the first-order derivative of this energy multiplied by displacement away from that point. The rest of the terms are the higher order terms. This expansion of U is usually kept up to the second-order derivative, referred to as the harmonic approximation.

At the equilibrium position, the force $\frac{\partial U}{\partial R_{I\alpha}}$ is zero, so the second term vanishes. The second-order derivative of the potential energy is called the force constant matrix:

$$\Phi_{I\alpha;J\beta} = \left.\frac{\partial^2 U}{\partial R_{I\alpha}R_{J\beta}}\right|_{\mathbf{R_0}} \tag{4.6}$$

The $\mathbf{R_0}$ represent the force constants that have been evaluated at the equilibrium position of the nuclei. $I\alpha$ corresponds to a row index, while $J\beta$ represents a column index. The force constants matrix can be constructed by moving atom J in the β direction by an amount x and calculating the force on atom I in the α direction. To make the results more accurate, the atom J is displaced with the same amount x but in the opposite direction. The element in the force constants matrix is the averaged value of the results of these two calculations:

$$\Phi_{I\alpha;J\beta} = -\frac{\left[F_{I\alpha}\left(u_{J\beta}=x\right) - F_{I\alpha}\left(u_{J\beta}=-x\right)\right]}{2x} \tag{4.7}$$

In total, 6N calculations are required to construct the whole force constants matrix, where N is

the number of atoms. This method is referred to as the finite displacement method [104]. It is important to mention that the $Phonopy$ package [150, 151] used here can exploit the symmetry of the structure, which will reduce the number of calculations required, saving some computational resources.

4.3.3 Dynamical matrix

Since the force on an atom can be expressed as the first derivative of potential energy, the force constants matrix can be used to interpret the force on atom I in direction α if all the atoms move in various directions:

$$M_I \frac{\partial^2 u_{I\alpha}}{\partial t^2} = F_{I\alpha} = \sum_{J\beta} -\Phi_{I\alpha;J\beta} u_{J\beta} \tag{4.8}$$

By introducing the mass-weighted displacement $e_{I\alpha} = \sqrt{M_I} u_{I\alpha}$ and factors $M_J^{-1/2}$, $M_J^{1/2}$ on right-hand side, the Equation 4.8 can be write as:

$$\frac{d^2 e_{I\alpha}}{dt^2} = \sum_{J\beta} -D_{I\alpha;J\beta} e_{J\beta} \tag{4.9}$$

where $D_{I\alpha;j\beta} = \frac{\Phi_{I\alpha;j\beta}}{\sqrt{M_I M_J}}$ is the dynamical matrix, which can be diagonalized to find eigenvalues. The vibrational frequencies are the square root of the eigenvalues.

For one-dimensional periodic structures, the displacement is expressed in terms of a plane wave, denoted as:

$$u_I(t) = u_0 e^{i(qR_I - \omega t)} \tag{4.10}$$

Here, u_0 is a constant, and R_I is the equilibrium position of the nuclei. q and ω represent the wavevector and frequency, respectively. With this expression and assuming atoms are only moving in α direction, Equation 4.8 can be written as:

$$\omega^2(q) = \frac{1}{M} \sum_J \Phi_{0J} \mathrm{e}^{iqR_J} \tag{4.11}$$

This equation states that the vibrational frequency can be obtained from the Fourier transform of the force constants matrix and it also depends on the wavevector. In the case of a material in three dimensions, three Cartesian directions and more numbers of unit cells or atoms need to be taken into consideration The force constants matrix in 3D cases is expressed as:

$$\Phi_{ls\alpha,l's'\beta} = \frac{\partial^2 U}{\partial \left(R_{l\alpha} + \tau_{s\alpha}\right) \partial \left(R_{l'\beta} + \tau_{s'\beta}\right)} \tag{4.12}$$

Here, the s is the specific atom; l represents the specific unit cell, and α and β represent the Cartesian direction. τ describes the position of the atom within the unit cell. The displacement of an atom in the form of propagating waves is:

$$u_{ls\alpha}(t) = u^0_{s\alpha} \mathrm{e}^{i[\mathbf{q}\cdot(\mathbf{R}_l+\tau_s)-\omega t]} \tag{4.13}$$

Finally, by following the same step in the 1D case, the dynamical matrix is described as:

$$D_{s\alpha,s'\beta}(\mathbf{q}) = \frac{1}{\sqrt{M_s M_{s'}}} \sum_l e^{i\mathbf{q}\cdot\mathbf{R}_l} \mathrm{e}^{i\mathbf{q}\cdot(\tau_{s'}-\tau_s)} \Phi_{0s\alpha,ls'\beta} \tag{4.14}$$

Now, the dynamical matrix, which describes the vibrational properties of a material, is dependent on the wavevector q [104]. In practical calculations, the force constants matrix Φ, required for obtaining the dynamical matrix, can be calculated within DFT. In this thesis, the finite displacement method was applied as described previously. Specifically, the $Phonopy$ package [150, 151] was used to displace every atom in various directions with a certain displacement. Subsequently, a self-consistent calculation was performed for each displaced atom to obtain the force constants matrix. The dynamical matrix was then obtained by performing a Fourier transform of the force constants matrix for a given wavevector. Finally, the obtained dynamical matrix was diagonalized, producing the vibrational frequencies.

In polar semiconductors or insulators, there is an extra polarization effect, induced by the long-range Coulomb interaction of the displacement of atoms, for the longitudinal optical (LO) phonon. The macroscopic electric field generated by the polarization near the gamma point results in an additional restoring force between atoms, yielding a higher LO frequency compared with the transverse optical phonon (TO). The difference in frequency between LO and TO phonons at the gamma point is known as the LO-TO splitting [152]. To consider this additional force, a non-analytical term correction is included when $q = 0$ in the dynamical matrix [153].

$$\tilde{D}^{\mathrm{NA}}_{s\alpha,s'\beta}(\boldsymbol{q}=\mathbf{0}) = \frac{4\pi}{\Omega\sqrt{M_s M_{s'}}} \frac{\left(\sum_\gamma q_\gamma Z^*_{s,\gamma\alpha}\right)\left(\sum_{\gamma'} q_{\gamma'} Z^*_{s',\gamma'\beta}\right)}{\sum_{\alpha\beta} q_\alpha \epsilon^\infty_{\alpha\beta} q_\beta} \tag{4.15}$$

ϵ is the dielectric permittivity tensor, which is related to polarization induced by the electrical field.

$Z^*_{s,\gamma\alpha}$ represents the Born effective charge tensor, expressed as:

$$Z^*_{s,\gamma,\alpha} = V\frac{\partial P_\gamma}{\partial u_{s,\alpha}} = \frac{\partial F_{s,\alpha}}{\partial E_\gamma} \tag{4.16}$$

V represents the volume of the unit cell. P is the macroscopic polarisation. The Born effective charge tensor gives the polarization per unit cell created along the direction γ while the displaced atom s along the direction α. It can also be denoted as the force acting on an atom generated by the macroscopic electric field [153].

The infrared spectra presented in this thesis displays absorbed frequencies on the x-axis and the absorption intensity on the y-axis. The intensity of infrared peaks is proportional to the square of the dipole moment change induced by the material's vibrations [154, 155]. The Born effective charge tensor, as described in Equation 4.16, characterizes the dipole moment change with respect to atomic displacements. Following Ref. 155, the infrared intensity is given by:

$$I_{\mathrm{IR}}(c) = \sum_{\alpha=1}^{3}\left|\sum_{s=1}^{n_{\mathrm{a}}}\sum_{\beta=1}^{3} {Z_{\alpha\beta}}^*(s)X_\beta(c,s)\right|^2 \tag{4.17}$$

$X_\beta(c,s)$ is defined as the Γ point eigen-displacements, which are obtained by dividing the corresponding eigenvector by the square root of the atomic masses. c and n_{a} describe the vibrational mode and the number of atoms in unit cells.

Chapter 5

Performance of meta-GGA rSCAN

5.1 Introduction

As mentioned previously in Section 3.6.4, the meta-GGA SCAN functional has been used to study different materials. Studies demonstrated that SCAN provides more accurate DFT descriptions of thin film materials [156], semiconductors [157], and liquid water [134] than the conventional LDA and GGA functionals. However, despite its success in predicting various material properties, the implementation of the SCAN functional is often challenging since a very dense numerical grid of space is required. While generating a library of ultrasoft pseudopotential for SCAN calculations, Bartók and Yates observed numerical instability and subsequently introduced several modifications to SCAN to mitigate this issue, resulting in the rSCAN functional [41]. As a newly developed meta-GGA functional, rSCAN has yet to be widely used, particularly for calculating band offsets. As pointed out by the authors of Ref. 158, accurately obtaining band offsets at the meta-GGA level is an attractive prospect due to the lower computational expense compared to using hybrid functionals or the GW approximation. To understand the performance of rSCAN and its comparison to PBE in predicting band offsets, the band gaps, IPs, and EAs for a test set of semiconductors were calculated using PBE and rSCAN. These results were further compared with experimental and GW@HSE calculated values provided in Ref. 38.

5.2 General concept of rSCAN

According to Ref. 41, the numerical instability problem of SCAN is induced by the iso-orbital indicator function, α.

$$\alpha = \frac{\tau - \tau_W}{\tau_U} \tag{5.1}$$

τ represents the orbital kinetic energy density. τ_W is the Weizsäcker kinetic energy density that incorporates a contribution to the kinetic energy density depending on the gradient of the particle density [159]. τ_U represents the kinetic energy density of the uniform electron gas. α detects different local bonding environments and is used to switch between different local approximations of the exchange and correlation energies based on different bonding types. The derivatives of α with respect to electron density have divergent behavior when electron densities decrease, leading to divergence in exchange-correlation potentials. This divergent behavior of α and resulting instability at the low-density region is partially due to the rapid decrease of τ_U. Therefore, the first modification that Bartók and Yates proposed was in τ_U, where a small constant τ_r was added. The τ_U was modified to become $\tau'_U = \tau_U + \tau_r$ with τ_r is equal to 1×10^{-4}, which only affects α at low densities. The second modification they proposed was to replace α with α', where $\alpha' = \frac{\alpha^3}{\alpha^2+\alpha_r}$, and α_r is equal to 1×10^{-3}. This regularized α' is only slightly different from the original α. The divergence of derivatives of α was corrected with these two modifications while preserving the original functional form of SCAN as much as possible.

Bartók and Yates also observed that numerical instability can arise when the switching function approaches $\alpha \approx 1$. This is because every derivative of the switching function should be 0 when $\alpha \approx 1$ in order to maintain the gradient expansion for the exchange energy in the slowly varying limit, which causes oscillations in the derivatives in the surrounding region. To effectively eliminate the oscillations, they replaced the $0 < \alpha < 2.5$ region with a 7th degree polynomial [41].

5.3 Testing performance of rSCAN

5.3.1 Constructing slab models

Following Ref. 38, 21 semiconductors were studied here, namely C, Si, and Ge in the diamond structure, BN, AlP, AlAs, AlSb, GaP, GaAs, GaSb, InP, InAs, InSb, ZnS, ZnSe, ZnTe, CdS, CdSe, and CdTe in the zinc-blende structure, and GaN and ZnO in the wurtzite structure. The calculations were performed on specific surface orientations, specifically the (111) surface for C, Si, and Ge in the diamond structure, the (1120) surface for GaN and ZnO in the wurtzite structure, and the (110) surface for the remaining materials in the zinc-blende structure. To construct slab models,

the first step involved optimizing the bulk crystal structure of each semiconductor. Subsequently, the relaxed bulk structures were copied and cleaved to produce slab models, which were then subjected to geometry optimizations while keeping the cell dimensions fixed at their corresponding bulk values. The (110) slab models of zinc-blende materials contain 9 atomic layers with a vacuum region of 33 Å to 37 Å separating periodic replicas along the surface normal. The 2×1 reconstructed (111) slab models of diamond materials have 14 atomic layers with approximately 32 Å vacuum region along the surface normal. (1120) slabs for GaN and ZnO in the wurtzite structure have 9 atomic layers with 33 Å vacuum region in the z-axis between periodic slabs.

5.3.2 Computational details

The calculations were conducted using the CASTEP package [112], with a plane wave basis set, periodic boundary conditions, and ultrasoft pseudopotentials. Exchange and correlation effects were included either at the GGA level using the PBE functional [119] or using the meta-GGA rSCAN functional [41]. In PBE bulk calculations, a plane wave cutoff of 700 eV and Monkhorst-Pack grids [160] with dimensions of $8\times8\times8$ were used, except for CdS, CdSe, and CdTe, which used a cutoff energy of 900 eV. On the other hand, the rSCAN bulk calculations used a plane wave cutoff energy of 800 eV, except for CdS, CdSe, and CdTe, which used a higher cutoff energy of 1000 eV, while the k-point sampling was held constant. In all slab calculations, $6\times6\times1$ k-point sampling was used, and the plane wave cutoff remained constant. Geometry optimizations were carried out until the force on each atom was below 0.05 eVÅ^{-1}. For the bulk calculations, the convergence threshold for pressure was set to be 0.1 GPa. Following the vacuum-level approach, the planar-averaged Kohn-Sham potential was used as the reference potential, which was extracted by the $c2x$ software package [161], in order to determine the IP and EA.

5.3.3 Comparison to previous calculations and experiments

The results of the calculations are presented in Fig. 5.1, while the corresponding numerical values and lattice constants are listed in Table 5.1 along with experimental values obtained from Ref. 38 and Ref. 162. Fig. 5.1a shows that the band gaps calculated using the rSCAN functional are generally higher than those obtained with the PBE functional, while also being closer to the experimental band gaps. However, despite these improvements, the calculated band gaps using rSCAN are still not as precise as the experimental values with a mean absolute error of 0.68 eV, suggesting that the issue of band gap underestimation still exists. On the other hand, the reported

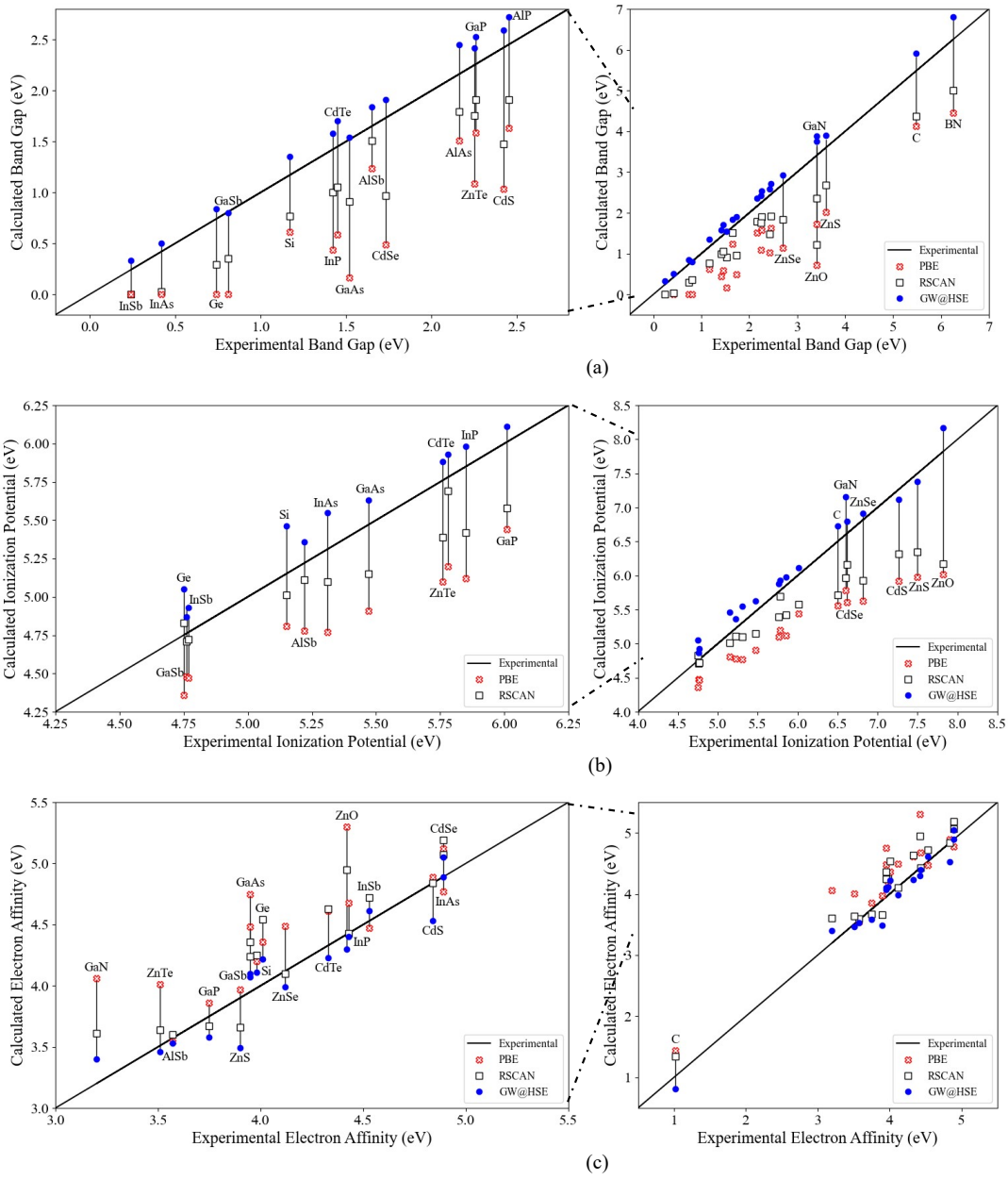


Figure 5.1: (a) Band gap of 21 semiconductors, (b) IP, and (c) EA of 18 semiconductors obtained using PBE and rSCAN along with the reported experimental and GW@HSE calculated values. [38, 162].

Table 5.1: Calculated lattice constants (a and c, in Å), band gaps (E_g), IP, and EA in eV using PBE and rSCAN along with the experimental values obtained from Refs. 38 and 162.

	PBE					rSCAN					Expt. [38, 162]				
	a	c	E_g	IP	EA	a	c	E_g	IP	EA	a	c	E_g	IP	EA
BN	3.624	-	4.46	6.99	2.53	3.607	-	5.00	7.23	2.23	3.616	-	6.25	-	-
C	3.571	-	4.13	5.56	1.44	3.554	-	4.37	5.71	1.34	3.567	-	5.48	6.50	1.02
Si	5.468	-	0.61	4.81	4.20	5.439	-	0.77	5.01	4.25	5.431	-	1.17	5.15	3.98
Ge	5.762	-	0.00	4.36	4.36	5.682	-	0.29	4.83	4.54	5.658	-	0.74	4.75	4.01
AlP	5.505	-	1.63	5.70	4.07	5.473	-	1.91	5.97	4.05	5.463	-	2.45	-	-
AlAs	5.730	-	1.51	5.30	3.79	5.679	-	1.80	5.54	3.74	5.661	-	2.16	-	-
AlSb	6.227	-	1.23	4.78	3.54	6.179	-	1.51	5.11	3.60	6.136	-	1.65	5.22	3.57
GaP	5.505	-	1.58	5.44	3.86	5.451	-	1.91	5.58	3.67	5.451	-	2.226	6.01	3.75
GaAs	5.748	-	0.16	4.91	4.75	5.673	-	0.91	5.15	4.24	5.654	-	1.52	5.47	3.95
GaSb	6.213	-	0.00	4.48	4.48	6.139	-	0.35	4.71	4.36	6.096	-	0.81	4.76	3.95
InP	5.956	-	0.44	5.12	4.68	5.902	-	1.00	5.42	4.43	5.869	-	1.42	5.85	4.43
InAs	6.191	-	0.00	4.77	4.77	6.108	-	0.03	5.10	5.07	6.058	-	0.42	5.31	4.89
InSb	6.632	-	0.00	4.47	4.47	6.564	-	0.00	4.72	4.72	6.479	-	0.24	4.77	4.53
ZnS	5.443	-	2.01	5.98	3.97	5.382	-	2.69	6.35	3.66	5.409	-	3.6	7.50	3.90
ZnSe	5.734	-	1.15	5.63	4.49	5.668	-	1.84	5.93	4.10	5.669	-	2.7	6.82	4.12
ZnTe	6.186	-	1.09	5.10	4.01	6.125	-	1.75	5.39	3.64	6.103	-	2.25	5.76	3.51
CdS	5.928	-	1.03	5.92	4.89	5.867	-	1.48	6.32	4.84	5.818	-	2.42	7.26	4.84
CdSe	6.196	-	0.49	5.61	5.12	6.123	-	0.97	6.16	5.19	6.077	-	1.73	6.62	4.89
CdTe	6.624	-	0.59	5.20	4.61	6.568	-	1.05	5.69	4.63	6.481	-	1.45	5.78	4.33
ZnO	3.282	5.296	0.72	6.02	5.30	3.233	5.211	1.21	6.17	4.95	3.250	5.207	3.40	7.82	4.42
GaN	3.217	5.243	1.72	5.78	4.06	3.180	5.182	2.36	5.97	3.61	3.190	5.186	3.40	6.60	3.20
Mean error:	0.08	0.07	-1.09	-0.78	0.32	0.02	0	-0.68	-0.48	0.20	-	-	-	-	-

GW@HSE values show an overestimation of band gaps by an average of 0.23 eV, resulting in a closer agreement with experimental values compared to rSCAN. In Fig. 5.1b, a similar trend is observed for IPs, with PBE underestimating IPs by 0.78 eV on average, resulting in higher VBM in comparison to experimental values. While rSCAN has shown some improvements with a mean underestimated error of 0.48 eV, it is still not as precise as GW@HSE results with a mean 0.17 eV difference compared to experimental data. Additionally, the agreement between calculated and experimental IPs become systematically worsens for higher IPs. Accordingly, it is expected the rSCAN to be more reliable for calculating VBOs of materials with similar IPs. Fig. 5.1c indicates that the calculated EAs do not follow the same trend as the IPs. As the EA is derived by subtracting the band gap from the IP (EA = IP - band gap), the underestimation of both the IP and band gap could lead to error cancellation, making it difficult to determine whether the EA is overestimated or underestimated. It is also important to note that when calculating VBOs and CBOs, which are based on differences in IPs or EAs rather than their absolute values, error cancellation may occur [158].

5.4 Conclusion

This short chapter has focused on evaluating the performance of the rSCAN functional by calculating the band gaps, IPs, and EAs of 21 semiconductors, using the GGA level PBE and meta-GGA level rSCAN functionals. These calculation results are consistent with a recent study that examined various meta-GGA functionals for calculating band alignments [158], including the closely related r^{2}SCAN functional [163], which demonstrates that rSCAN provides band offsets that are closer than PBE to experiment and to higher-level calculations. Nevertheless, discrepancies exist when compared to experimental or GW calculations, especially for materials with larger IPs. It is reasonable to conclude that rSCAN provides more accurate offsets than PBE, but a higher level of theory like GW is required for $<\sim$0.5 eV accuracy.

Chapter 6

First-principles band alignments at the Si:anatase TiO_2 interface

6.1 Introduction

As previously discussed in Section 2.2.4 of this thesis, Ref. 86 has shown the capability of transforming the TiO_2 passivating layer from electron-selective to hole-selective contacts by reducing the oxygen content to form TiO_x nanolayers. Apart from stoichiometry, little is currently understood about the atomistic structure of the Si:TiO_2 interface and its impact on the band offsets. Therefore, the purpose of this chapter is to use first-principles calculations to investigate the dependence of band offsets on the structural features of the Si:TiO_2 interface. This was accomplished through band offset calculations using both vacuum-level alignment and heterointerface alignment methods, as described in Section 4.2. Additionally, the influence of various exchange-correlation treatments, including PBE, PBE+U, rSCAN, and functionals beyond the GGA level was investigated.

6.2 Methods

6.2.1 Constructing Si slabs

As one of the most important semiconductors, Si has been extensively used in the modern semiconductor industry. The stability of various Si surfaces has been studied both experimentally and theoretically [164–166]. The Si(001) surface is the most stable at high temperatures, as determined by first-principles calculations in Ref. 166. This conclusion has been supported by Bermond's ex-

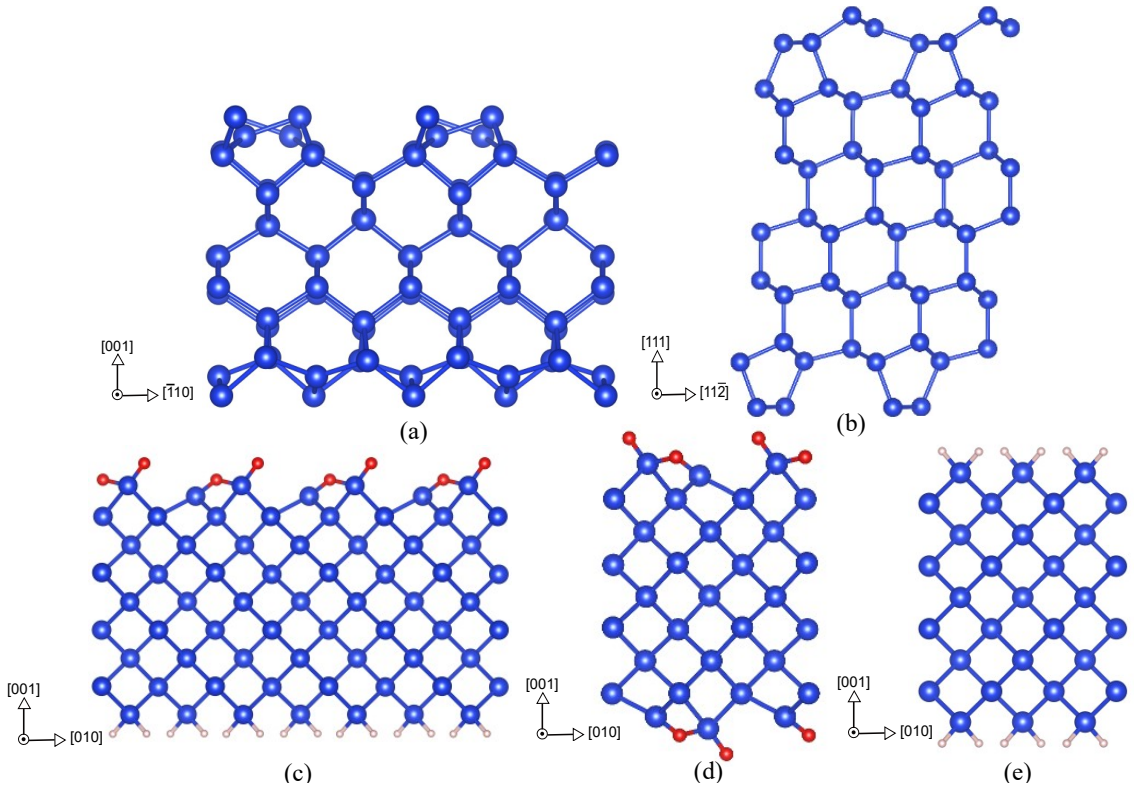
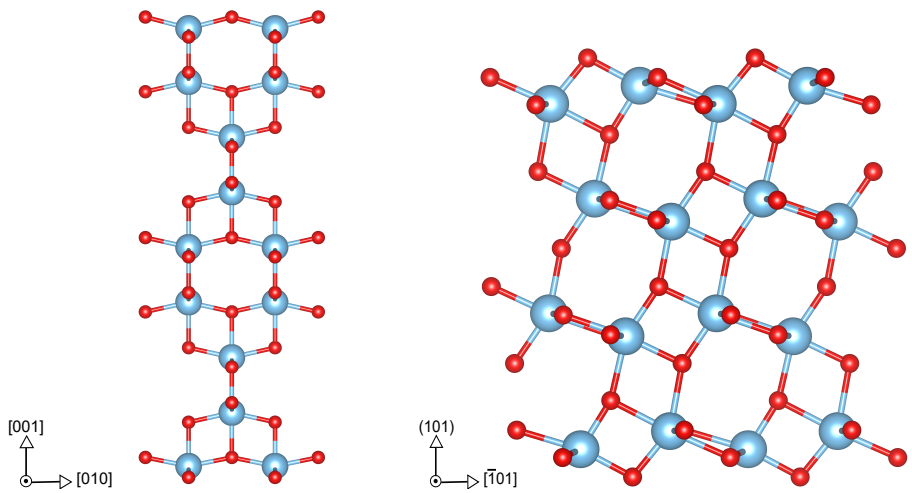


Figure 6.1: (a) Reconstructed Si(001) slab, (b) Si(111) slab, (c) oxygen-terminated Si slab with hydrogen passivated at the lower surface, (d) oxygen-terminated Si slab with oxygen passivated at the lower surface, and (e) hydrogen-terminated Si slab. Si/H/O atoms are shown in blue/pink/red, respectively.

perimental research [164]. Therefore, the Si(001) surface was the main focus of this study. Cleaving c-Si along this plane resulted in dangling bonds at the surface. For the vacuum-level alignment calculations, these dangling bonds were saturated through atomic passivation or by allowing the surface to undergo a 2×2 reconstruction [167]. In addition, the reconstructed 2×1 Si(111) surface was also considered to examine the impact of surface orientation on band offsets.

Following the procedure given in Section 5.3.1, the optimized slab models for Si(001) and (111) surfaces were created, shown in Fig. 6.1a and 6.1b. Specifically, the reconstructed Si(001) slab has approximate lateral dimensions of 16 Å$\times$8 Å (8 surface atoms) and a thickness of 11 Å (9 atomic layers), with a vacuum region of 20 Å separating periodic replicas along the surface normal. The reconstructed Si(111) slab has dimensions of 4 Å$\times$13 Å (4 surface atoms) and a thickness of 20 Å (14 atomic layers), with a vacuum region of 20 Å. The models where the dangling bonds on both the lower surface and upper surface were saturated with either O or H, resulting in Si-OH, Si-OO, and Si-HH slabs, are shown in Figs. 6.1c, 6.1d, and 6.1e, respectively. The initial structure of oxygen-terminated Si slabs is constructed based on the ether structure pro-



(a) (b)

Figure 6.2: (a) Reconstructed TiO_2(001) slab, (b) TiO_2(101) slab. O and Ti atoms are shown in red and light blue, respectively.

posed in Ref. 168, where oxygen atoms form a bridge between two adjacent Si atoms and are singly bonded to each Si atom. During the relaxation process, half of the single-bonded oxygens undergo cleavage and become double bonded to Si, forming a ketone structure. Eventually, the oxygen-terminated Si(001) surface was found to comprise a mix of ether and ketone structures, arranged in a 2×2 reconstruction. The Si-HH and Si-OO slabs have approximate lateral dimensions of 6 Å×6 Å with similar thickness and vacuum region as the Si(001) slab, while the lateral dimensions of Si-OH slab are 16 Å×6 Å.

6.2.2 Constructing TiO_2 slabs

The aim of experimental studies on synthesizing the Si:TiO_2 interface is to produce amorphous TiO_2 due to its excellent passivation qualities [63]. The presence of anatase TiO_2 in this interface is often associated with stress-induced phase transformation and the generation of defects, which can result in reduced passivation quality of TiO_2 and increased surface recombination velocity [82]. However, anatase is the most commonly found form at the nanoscale in TiO_2 [169]. As reported in Ref. 63, annealing at temperatures above 300 °C is typically necessary to form a front contact for n-type solar cells featuring a full-area TiO_2 contact, leading to a phase transformation from amorphous to anatase TiO_2. Other studies have confirmed the existence of this transformation at around 300 °C, with lower temperatures being required to form an amorphous layer [84, 85]

To closely match the experimental findings, anatase TiO_2 was used in this study. The TiO_2(001)

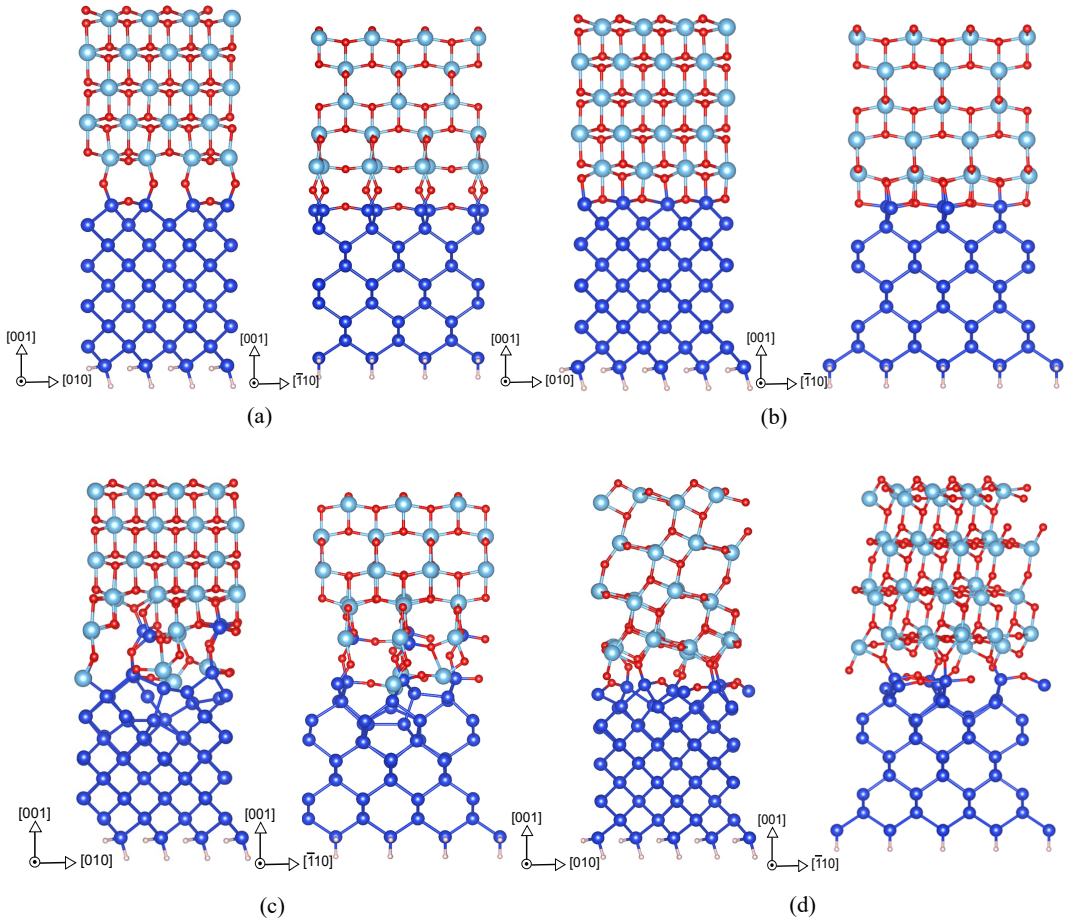


Figure 6.3: Atomic structure of (a)Model 1, (b) Model 2, (c) Amorphous Si:TiO_2(001), Model 3 and (d) Si:TiO_2(101), Model 4 interface models. Si/H/O/Ti atoms are shown in blue/pink/red/light blue respectively.

and TiO_2(101) surfaces were particularly focused on, shown in Fig. 6.2a and 6.2b, respectively. Among the anatase TiO_2 surfaces, TiO_2(101) is known to be the most thermodynamically stable surface and has been widely studied in both experimental and theoretical research [90, 169, 170]. On the other hand, the TiO_2(001) surface, despite being the next-most-stable surface, is predicted to exhibit strong chemical activity and is also of interest [171]. The anatase TiO_2(101) slab was calculated with lateral dimensions of 10 Å×4 Å, a thickness of 13 Å, and a vacuum region of 23 Å. The TiO_2(001) slab has lateral dimensions of 4 Å×4 Å, a thickness of 20 Å, and a vacuum region of 23 Å in the z-axis between periodic slabs.

6.2.3 Constructing Si:anatase TiO_2 interface models

The Si(001) slab was chosen as the substrate for the Si:TiO_2 heterointerface model. Two types of crystalline Si:anatase TiO_2(001) interface models, referred to as Model 1 and Model 2, were constructed as periodic supercells with various interfacial bonding, as shown in Fig. 6.3a and 6.3b,

respectively. The a and b vectors of the TiO_2 slab were oriented at 45 degrees with respect to the a and b vectors of the Si slab in order to create an ordered arrangement of Si-O and Ti-O bonds. In addition, Model 3 and Model 4, shown in Fig. 6.3c and 6.3d, were constructed to include amorphous Si:TiO_2(001) and crystalline Si:TiO_2(101) interface models. Model 3 was generated using the $cp.x$ program from the Quantum ESPRESSO package [149] with a Nose-Hoover thermostat [149, 172] for several picoseconds in Car-Parrinello molecular dynamics simulations. The resulting structure was then optimized using the CASTEP package [112]. It is important to note that this method was used to produce a disordered interface structure model and does not represent a realistic annealing process.

The heterointerface alignment calculations were performed using Models 1–4, where an 11 Å-thick slab (9 layers) of Si was combined with a 10 Å-thick slab of TiO_2 (5 layers), followed by 20 Å of vacuum. The lower face and upper face of the Si slab were saturated with hydrogen and oxygen atoms, respectively. The interface models were constructed using the relaxed Si lattice parameters, with lateral dimensions of the unit cell set at 6 Å$\times$6 Å. The effect of lattice mismatch on band alignment was investigated by constructing Model 1 and Model 2 using the TiO_2 lattice parameters, shown in Section 6.4.5.

6.2.4 Computational details

All calculations in this chapter were carried out following the same computational detail provided in Section 5.3.2. The PBE functional [119] at the GGA level, PBE+U at the GGA+U level [132], and rSCAN [41] at the meta-GGA level were used to investigate the effect of exchange-correlation functionals on band alignment, as well as functionals beyond the GGA level, which acted as a post-processing step. The PBE and PBE+U calculations were conducted with a maximum cutoff for the plane wave basis sets of 700 eV, while 800 eV was used for rSCAN calculations. To minimize interactions arising from the periodic replication of the slab and ensure more accurate calculation results, a large vacuum region and the self-consistent dipole correction were applied in the calculations [173]. Reciprocal space sampling was performed using Monkhorst-Pack grids [160], with dimensions of 6$\times$6$\times$1 for vacuum-level alignments, 4$\times$4$\times$1 for heterointerface alignments, and 8$\times$8$\times$8 for bulk calculations. All calculations were fully relaxed until the force on each atom was smaller than 0.05 eVÅ^{-1}, and the convergence threshold for pressure was set at 0.1 GPa in bulk calculations. The planar-averaged Kohn-Sham potential used as the reference potential was extracted using the $c2x$ software package [161].

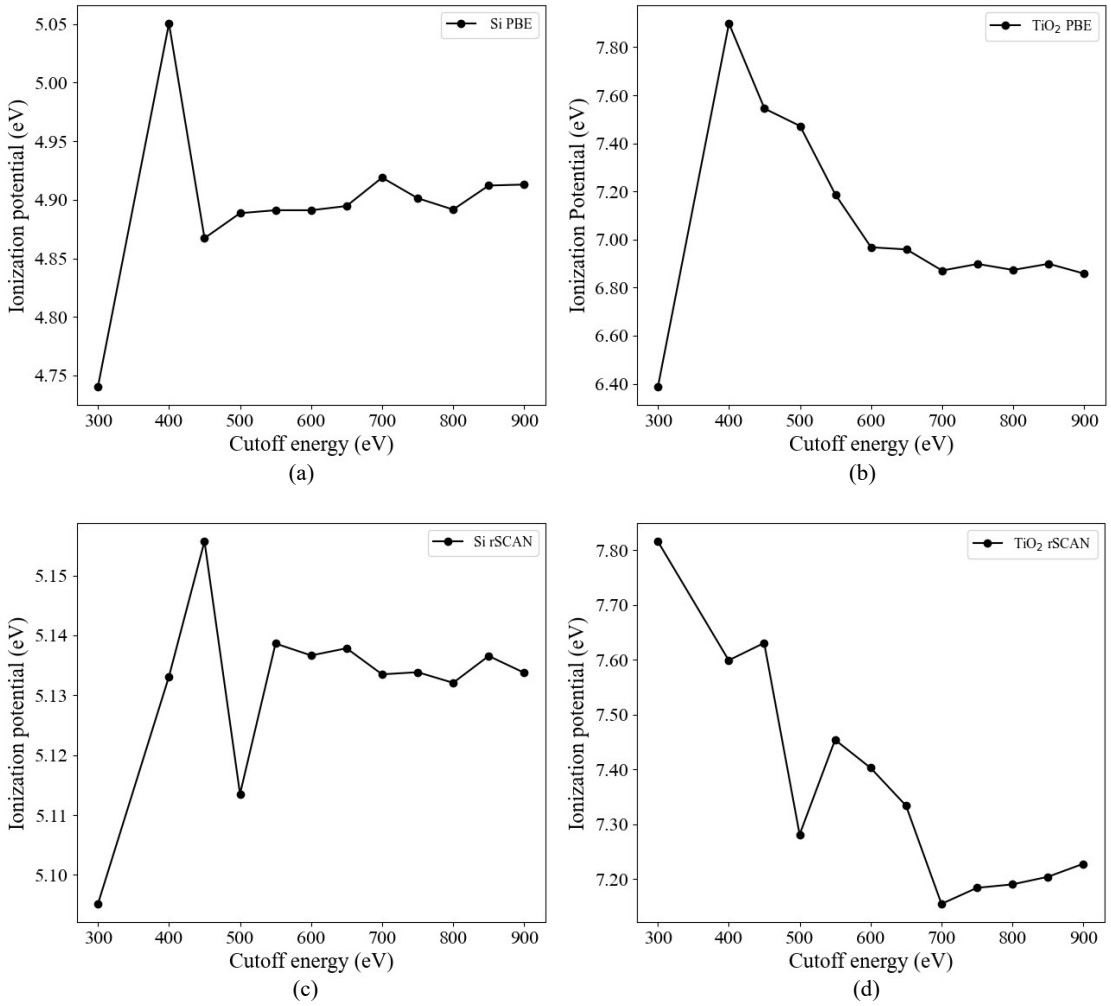


Figure 6.4: Calculated IP of Si(001) and TiO_2(001) surfaces using PBE and rSCAN as cutoff energy increases from 300 eV to 900 eV. (a) and (c) are the calculated IP of Si(001) surface using PBE and rSCAN, respectively. (b) and (d) are the calculated IP of TiO_2(001) surface using PBE and rSCAN, respectively.

6.3 Convergence tests

6.3.1 Cutoff energy

The chosen cutoff energy and k-point sampling for Si and TiO_2 listed in the above section were determined from convergence tests. The aim of the convergence test is to achieve accurate results while minimizing computational costs. Since the primary focus of this chapter is the band alignments between Si and TiO_2, the convergence test for cutoff energy was specifically conducted in relation to the IP of reconstructed Si(001) and TiO_2(001) surfaces following the procedure provided in Section 4.2.1. Figure. 6.4 shows the calculated IP of these two surfaces using PBE and rSCAN as the cutoff energy increases from 300 eV to 900 eV. The calculations were conducted with k-point grid of $6\times6\times1$ and $8\times8\times8$ for slab and bulk calculations, respectively.

In Fig. 6.4a and Fig. 6.4c, as the cutoff energy reaches 550 eV and beyond, the calculated IP of Si(001) surface remains consistent, with a negligible variation of only 0.01 eV, when using PBE and rSCAN, respectively. In terms of TiO_2(001) surface, the calculated IP using PBE remains the same value as the cutoff energy reaches 700 eV, while the calculated IP remains constant as the cutoff energy is higher than 750 eV when using rSCAN. Since heterointerface calculation, which involves both Si and TiO_2 slabs, was conducted in this thesis, the choice of cutoff energy was determined based on the convergence test performed on TiO_2. For the PBE functional, a cutoff energy of 700 eV was sufficient, while for the rSCAN functional, a higher cutoff energy of 800 eV was proven to be reliable.

It should be noted that when using ultrasoft pseudopotentials, the augmentation charges can be described using a finer grid. In the CASTEP package, this finer grid for the augmentation charges is set by the "fine grid scale" parameter. To determine the appropriate value for this parameter, a convergence test was conducted by calculating the energy difference between the VBM and the macroscopic average of the Kohn-Sham potential, denoted as $\Delta\varepsilon_{\mathrm{VBM-Ref}}$, of bulk structure, while varying the "fine grid scale" at different cutoff energy levels. The $\Delta\varepsilon_{\mathrm{VBM-Ref}}$ is a crucial quantity for determining the IP. The details of the convergence test can be found in Section A.2 of Appendix A. Based on the results presented in Figure A.1, at the chosen cutoff energy levels in this thesis (700 eV for PBE and 800 eV for rSCAN), it was observed that changes in "fine grid scale" parameter has no significant influence on the calculated $\Delta\varepsilon_{\mathrm{VBM-Ref}}$. Therefore, for the calculations in this thesis, the "fine grid scale" parameter is set to be 1.75, which is the default setting in CASTEP.

6.3.2 k-point sampling for bulk Si and TiO_2

The convergence test for k-point sampling was conducted separately for bulk and slab models since a vacuum region is involved in the slab model, which set the k-point in the direction perpendicular to the surface to be 1. For bulk models, the convergence test focuses on calculating the $\Delta\varepsilon_{\mathrm{VBM-Ref}}$, which serves as the initial step in determining the IP. Figure 6.5 displays the calculated $\Delta\varepsilon_{\mathrm{VBM-Ref}}$ for bulk Si and TiO_2 using the PBE and rSCAN functionals, as the k-point sampling range from $2\times2\times2$ to $10\times10\times10$. The calculations were carried out with cutoff energy of 700 eV and 800 eV for PBE and rSCAN, respectively.

The calculated $\Delta\varepsilon_{\mathrm{VBM-Ref}}$ of bulk Si shows a negligible variation when using both the PBE and rSCAN functionals for all the k-point grids considered in the calculation. Specifically, as the

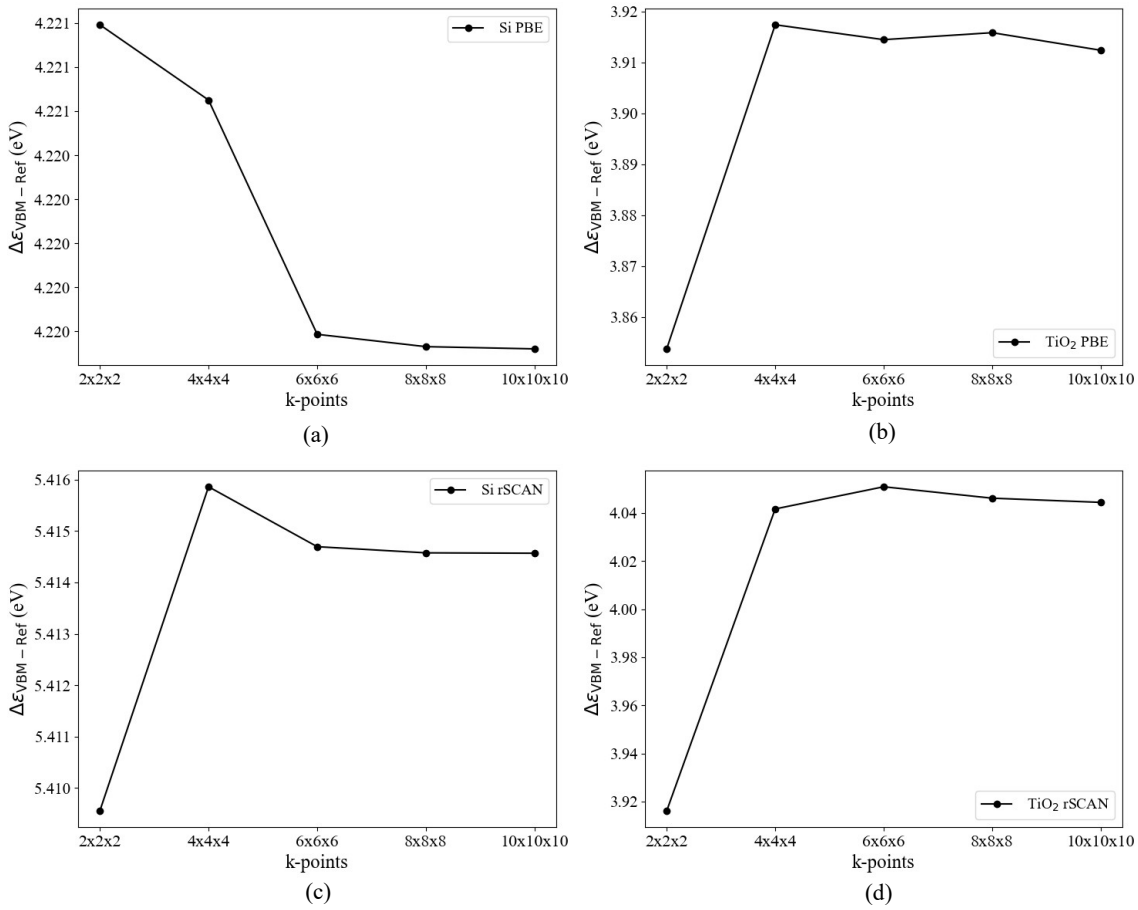


Figure 6.5: Calculated $\Delta\varepsilon_{\mathrm{VBM-Ref}}$ of bulk Si and TiO_2 using PBE and rSCAN as the k-point sampling increase from $2\times2\times2$ to $10\times10\times10$. (a) and (c) are the calculated $\Delta\varepsilon_{\mathrm{VBM-Ref}}$ of bulk Si using PBE and rSCAN, respectively. (b) and (d) are the calculated $\Delta\varepsilon_{\mathrm{VBM-Ref}}$ of bulk TiO_2 using PBE and rSCAN, respectively.

k-point sampling reaches $6\times6\times6$ and beyond, the calculated energy difference is essentially zero. In the case of TiO_2, there is a slight variation of 0.1 eV as the k-point sampling changes from $2\times2\times2$ to $4\times4\times4$. Once the k-point sampling reaches $6\times6\times6$, the calculated $\Delta\varepsilon_{\mathrm{VBM-Ref}}$ of TiO_2 becomes nearly constant. Therefore, it is reasonable to select a k-point sampling of $6\times6\times6$ or higher for both bulk Si and TiO_2. In this study, a k-point sampling of $8\times8\times8$ was chosen for bulk Si and TiO_2 to ensure better-converged results.

It is important to note that the bulk anatase TiO_2 unit cell exhibits a tetragonal shape, with a significant difference in the lattice constant along the z-axis compared to the other two axes. Considering this, it is advisable to adjust the k-point grid accordingly, with a smaller grid size in the z-axis to accommodate the larger cell length. To conduct a comprehensive k-point convergence test for TiO_2, the k-point grid was modified specifically along the z-axis while maintaining a fixed sampling of 8×8 for the remaining two axes. The calculated energy difference, $\Delta\varepsilon_{\mathrm{VBM-Ref}}$, along with different grid sizes in the z-axis is given in Section A.3 of Appendix A. From the

results depicted in Fig. A.2, it is evident that the energy difference is well converged when using a k-point grid of 8×8×2 or larger. The actual cubic 8×8×8 grid used in this thesis is also proven to be effective. An 8×8×8 k-point grid was also used in Ref. 174 for optimizing bulk anatase TiO_2. For future calculations, it is recommended to use an 8×8×2 k-point sampling for bulk TiO_2 to reduce computational cost. However, considering that only 12 atoms are involved in the bulk anatase TiO_2 system, the computational cost is unlikely to significantly differ when using an 8×8×8 grid in this thesis.

6.3.3 k-point sampling for Si and TiO_2 slabs

Based on the above section, an 8×8×8 k-point grid was chosen for bulk Si and TiO_2 calculations. When dealing with Si and TiO_2 slabs, adjustments of k-point sampling are necessary due to the presence of a vacuum region along the z-axis between the periodic slabs and different sizes of cells used. In the absence of periodicity in the z direction, the k-point is set to be 1 in the z dimension. However, modifying the k-point sampling for Si and TiO_2 slabs along the remaining two axes is challenging since the constructed slabs in this thesis do not typically correspond to the expanded cells derived from the bulk structure. For example, the orientation of the Si(001) slab is different from the bulk Si in order to easily modified the surface Si atoms and achieve the reconstructed surface. The Si-OH slab is a 3×1 surface cell expanded from bulk Si for better visualizing the 2×2 reconstructed surface. As it is difficult to change the k-point sampling accordingly based on bulk Si and TiO_2, a separate k-point convergence test was conducted for each individual slab.

The convergence test focuses on calculating the $\Delta\varepsilon_{\mathrm{Vac-Ref}}$, which represents the energy difference between the macroscopic average of reference potential in the vacuum region and the bulk-like region obtained from the slab calculation with respect to the k-point sampling. The computational details and the calculated $\Delta\varepsilon_{\mathrm{Vac-Ref}}$ of Si and TiO_2 slabs with different k-point sampling are provided in Section A.4 of Appendix A. According to Fig. A.3, Fig. A.4, and Fig. A.5, it is clearly observed that all the Si and TiO_2 slabs are well converged as the k-point sampling reaches 6×6×1 and higher. Therefore, even though it is difficult to adjust the k-point sampling for slab models based on the convergence test for bulk models, the convergences tests indicate that a 6×6×1 k-point sampling is a reliable choice for Si and TiO_2 slabs in order to obtain accurate results in this thesis.

6.3.4 Vacuum spacing and slab thickness

The vacuum spacing for all the slab models is constructed to be 20 Å to 23 Å in order to avoid spurious slab-slab interactions. This choice of vacuum spacing aligns with similar values used in the existing literature. In Ref. 174, approximately 20 Å of empty space was included in TiO_2(001) and TiO_2(101) slab. A 14 Å of vacuum space was included in the $SrTiO_3$:anatase TiO_2(001) interface in Ref. 175. The Si(100) slab in Ref. 176 was generated from the 7 monolayers of bulk Si with approximately 12 Å of vacuum space included. When dealing with Si:SiO_2 interface, 20 Å vacuum was implemented along the normal direction to the interface to separate the periodic images [177]. Considering the vacuum spacing incorporated in Si and TiO_2 slabs throughout the literature, it is reasonable to conclude that the 20 Å to 23 Å vacuum region in Si and TiO_2 slabs will effectively prevent spurious interactions between the replicated slabs.

The selection of slab and interface thicknesses in this thesis is influenced by the thicknesses reported in previous studies as well as the available computational resources. For instance, when considering the thickness of the Si slab, published works on Si-based heterointerfaces, such as $ZrSiO_4$:Si(001) [176], GaP:Si(001) [178], HfO_2:Si, and ZrO_2:Si interfaces [49], have considered Si slabs ranging from 7 to 13 monolayers. Therefore, in the Si:TiO_2 interface, a Si slab comprising 9 layers with a thickness of 11 Å is incorporated. To ensure compatibility with the Si slab, the thickness of the TiO_2 slab is chosen to match that of the Si slab. Thus, a TiO_2 slab consisting of 5 monolayers with a thickness of 10 Å is used to construct the Si:TiO_2 interface. In addition, 4 and 6 monolayers of anatase TiO_2 were considered when constructing $SrTiO_3$:TiO_2(001) interface in Ref. 175.

The choice of slab thickness is also influenced by the computational power available for the calculations. In the case of incorporating 9 layers of Si and 5 layers of TiO_2, the resulting 2×2 Si:TiO_2 interface (Model 1-3) contains a total of 216 atoms. The presence of this large number of atoms significantly slows down the calculation process and sometimes leads to job crashes due to memory deficiency. Including additional layers of Si or TiO_2 will result in even slower computations. If computational power continues to advance, it is advisable to match the thickness of Si or TiO_2 with experimental studies, which is typically a few nanometers [63]. By aligning the slab thickness with experimental measurements, the calculated results should be more reliably compared with experimental studies. In this thesis, the thickness of Si and TiO_2 is selected to be consistent with what is commonly applied in other computational studies.

6.4 Results

6.4.1 Structural and electronic properties of bulk anatase TiO_2 and Si

Table 6.1: Experimental and calculated lattice constants (Å) and band gap (eV) of Si and anatase TiO_2 using PBE and rSCAN.

	PBE			rSCAN			Expt. [38, 179, 180]			PBE in Ref. [38, 90, 181]		
	a	c	E_g^{PBE}	a	c	E_g^{rSCAN}	a	c	$E_g^{Expt.}$	a	c	E_g^{theory}
Si	5.47	-	0.61	5.44	-	0.77	5.43	-	1.17	5.48	-	0.69
TiO_2	3.80	9.71	2.12	3.77	9.57	2.54	3.78	9.51	3.20	3.79	9.74	2.08

Table 6.1 presents the structural parameters of Si and anatase TiO_2 determined by calculations using the PBE and rSCAN functionals. This table also includes a comparison to values obtained from previous PBE calculations, as well as experimental measurements. The calculated lattice parameters using the PBE functional show reasonable agreement with prior computational results for both materials. However, there is a tendency for the PBE functional to overestimate bond lengths and lattice constants, with a maximum error percentage of 2.21% compared to experimental values [182]. The lattice parameters obtained using the rSCAN functional show better agreement with experimental measurements. The optimized lattice parameters listed in Table 6.1 were used to construct the slab and interface models discussed in Section 6.2. In terms of electronic properties, there is a significant underestimation of the band gap for both Si and anatase TiO_2 when using the PBE functional, with error percentages of -48% and -34%, respectively. While the use of the rSCAN functional results in decreased error percentages for the band gaps, the values of -34% and -21% for Si and TiO_2 indicate that the "band gap problem" problem remains a significant issue.

Fig. 6.6a shows the band structure of anatase TiO_2 calculated using both the PBE and rSCAN functionals. Anatase TiO_2 has an indirect band gap with the highest occupied state located near the X k-point and the lowest unoccupied state at the Γ point, consistent with the findings of a prior study [183]. The calculated band gap ($\Gamma - X$ gap) using the PBE functional is 2.12 eV. Similar characteristics were observed when using the rSCAN functional, where the indirect band gap is obtained between the Γ and X k-points, but the band gap is enlarged by 0.42 eV compared to the PBE functional. In order to better understand the character of the conduction band and valence band, the partial density of states (PDOS) was calculated using both functionals. The DOS for the valence and conduction bands projected onto the $3d$ states of the Ti atoms and the $2p$ states of the O atoms are shown in Fig. 6.6b and Fig. 6.6c. The PDOS analysis shows that the conduction band

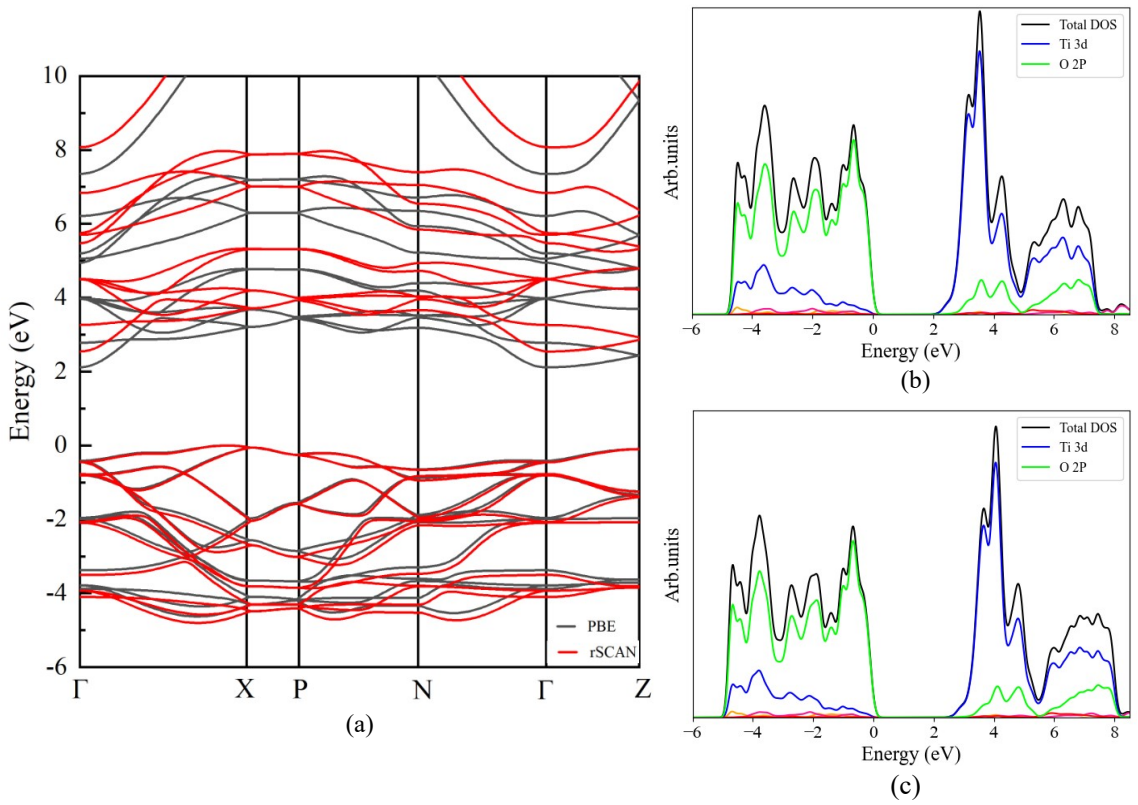


Figure 6.6: (a) Band structure of anatase TiO_2 calculated using PBE (black) and rSCAN (red). Partial density of states obtained using (b) PBE and (c) rSCAN. In units of the reciprocal lattice vectors, the k-point sampling are chosen as Γ = 0 0 0, X = 0 0 $\frac{1}{2}$, P = $\frac{1}{4}$ $\frac{1}{4}$ $\frac{1}{4}$, N = 0 $\frac{1}{2}$ 0, Z = $\frac{1}{2}$ $\frac{1}{2}$ -$\frac{1}{2}$. Gaussian broadening of 0.1 eV is applied for the DOS plot. The energy zero was set to the top of the valence band.

of TiO_2 is primarily dominated by the $3d$ states of the Ti atoms, while the valence band is mainly formed by the O $2p$ states [184]. The conduction band displays two sub-bands, with ranges of 2-5 eV and 5-8 eV. The PDOS plots also highlight an enlargement of the band gap.

Regarding the band structure of Si in Fig. 6.7a, it also exhibits an indirect band gap, with the highest occupied state located at Γ points and the lowest unoccupied states located between X and Γ. Both PBE and rSCAN produce a similar band structure except that the band gap produced by the latter functional is 0.16 eV higher. The valence and conduction bands of Si consist of $3s$ and $3p$ orbitals, as shown in Fig. 6.7b and Fig. 6.7c, which together forms the outer shell and can hybridize to form sp^3 orbitals [185]. Three regions are observed in the energy range of the valence band. The first sub-band, ranging from -12 eV to -7.7 eV, is mainly from $3s$ states, while the second sub-band, ranging from -7.7 eV to -5 eV, is hybridized by $3s$ and $3p$ orbitals. The third region of the valence band, ranging from -5 eV to 0 eV, as well as the conduction band, are mostly dominated by $3p$ states. After obtaining the lattice parameter and band gap values, the next step

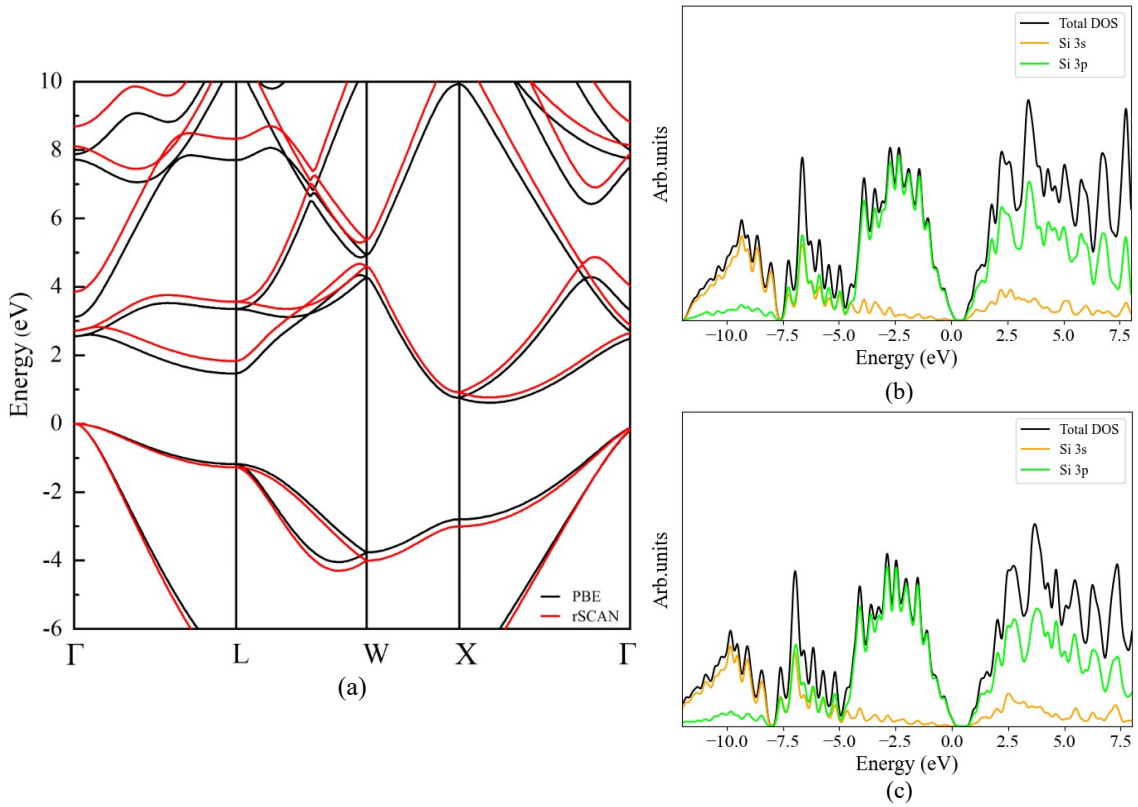


Figure 6.7: (a) Band structure of Si calculated using PBE (black) and rSCAN (red). Partial density of state obtained using (b) PBE and (c) rSCAN. In units of the reciprocal lattice vectors, the k-point sampling are chosen as Γ = 0 0 0, $L = \frac{1}{2}\ \frac{1}{2}\ \frac{1}{2}$, $W = \frac{1}{2}\ \frac{1}{4}\ \frac{3}{4}$, $X = \frac{1}{2}\ 0\ \frac{1}{2}$. Gaussian broadening of 0.1 eV is applied for the PDOS plot. The energy zero was set to the top of the valence band.

involves extracting the IP and EA via slab calculations.

6.4.2 Vacuum-level alignments and effects of surface termination

Based upon the vacuum-level alignment method discussed in Section 4.2.1, the calculated IP and EA using PBE, PBE+U, and rSCAN for TiO_2(001) are shown in Fig. 6.8a. The calculated IPs obtained from PBE and rSCAN agree reasonably well with previously reported experimental IPs within a 0.1 eV difference, lower than the mean error obtained for the test set of semiconductors in the previous chapter. The experimental IPs are indicated by the black dotted line in Fig. 6.8 [96, 97, 186].

However, the calculated EAs of TiO_2(001) using PBE and rSCAN do not match well with the experimental EAs reported in the literature, which are generally around 4.0 eV, due to the underestimation of the band gap by these functionals. The red dotted line in Fig. 6.8 represents the experimental value of EA. The PBE+U results show that the IP value of TiO_2(001) is independent of the U value used, while the EA value is sensitive to the U value. The IP and EA of TiO_2(101)

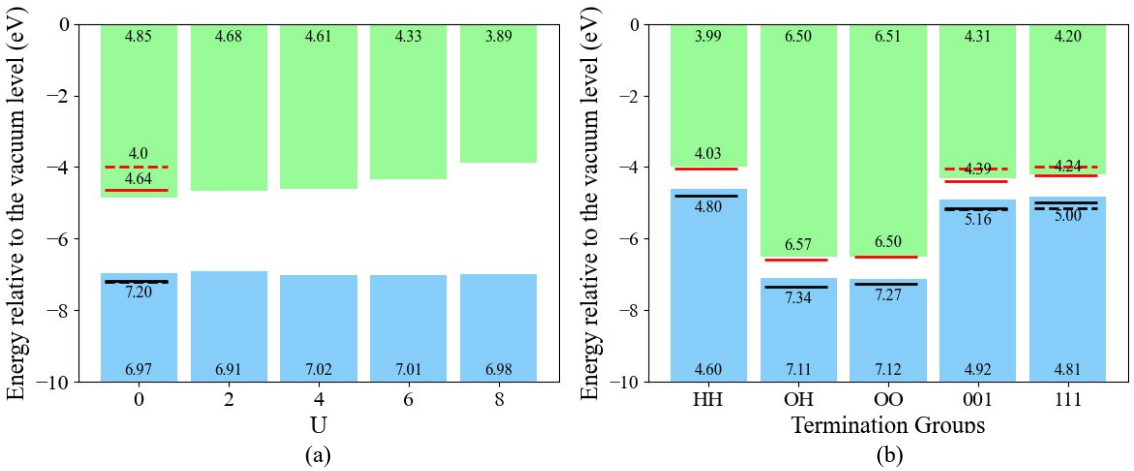


Figure 6.8: Calculated IPs (blue) and EAs (green) of (a) TiO_2(001) and (b) Si slabs using PBE and rSCAN. PBE+U was also used for TiO_2(001) as the U value increases from 0 to 8 eV. The values at the top and bottom represent calculated EA and IP, respectively. The black and red solid lines are the calculated IP and EA using rSCAN. The red and black dotted lines are EAs and IPs in literature [96–98, 162, 186]. The IP and EA in this plot represent the negative values of the valence band maximum and conduction band minimum, respectively, relative to the vacuum level.

are about 0.46 eV higher than those of the (001) surface, with values of 7.43 eV and 5.31 eV using PBE and 7.91 eV and 5.37 eV using rSCAN, respectively. This finding is consistent with experimental measurements reported in Ref. 102, which also observed an increased IP for the (101) surface with a range of 0.1–0.5 eV depending on surface conditions.

Fig. 6.8b shows a similar observation where the IP determination of Si(001) and (111) slabs is generally consistent with experimental measurements, but there are notable differences in EA [98, 162, 186]. These differences in EA are attributed to the underestimation of the band gap, which affects all Si slabs consistently. The calculated IP and EA of the hydrogen-terminated slab using both PBE and rSCAN are in good agreement with previous calculations using the LDA functional [187]. The termination groups on the Si slab have a significant effect on the calculated EAs and IPs. Specifically, the IPs and EAs of Si-OH and Si-OO are approximately 2.1–2.5 eV higher than those of Si-HH, Si(001), and Si(111).

The band offsets determined through the vacuum-level alignment method of Si:TiO_2(001) and Si:TiO_2(101) interfaces using PBE and rSCAN are shown in Fig. 6.9. The most notable feature of this figure is the oxygenated Si slab exhibits a significant reduction in band offsets of approximately 2.1–2.5 eV compared to H termination or pure reconstructed Si slabs, mainly due to a substantial increase in the IP and EAs, as presented in Fig. 6.8b. These observations show how the choice of termination group at the slab has an impact on the calculated band offsets through the

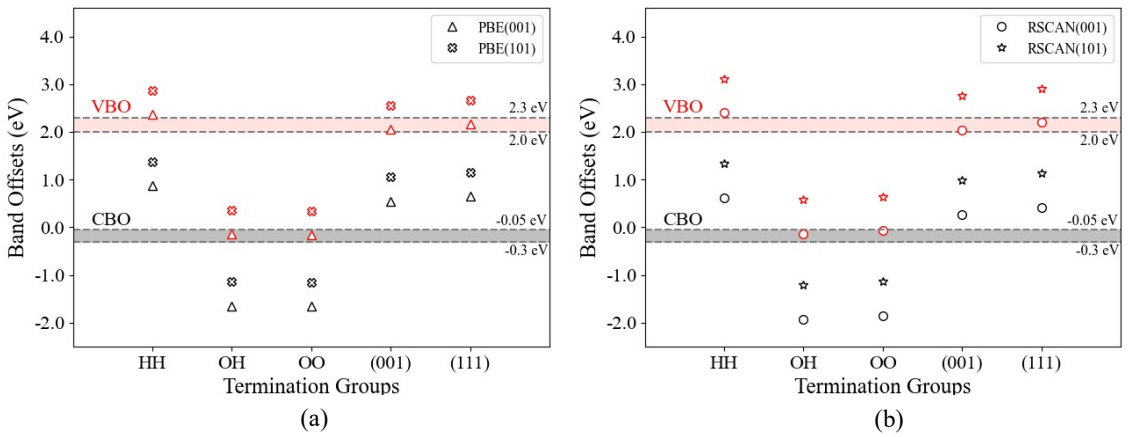


Figure 6.9: Calculated VBOs, shown in red, and CBOs, shown in black, of Si:TiO_2(001) and Si:TiO_2(101) interfaces using (a) PBE and (b) rSCAN. The shaded regions denote the range of values previously reported in experimental literature, as discussed in Section 2.4.

vacuum-level approach. The variations in oxygen-terminated Si slabs can be attributed to changes in the surface structure of Si-OH and Si-OO slabs. This behavior is relevant to the findings for the diamond C(001) surface, as reported in Ref. 188. However, unlike for diamond, the most stable oxygen-terminated Si(001) surface was found to arrange in a 2×2 reconstruction, shown in Fig. 6.1c. The stability of this reconstruction for the diamond C surface was checked and found that the surface relaxed to a pure ether structure, in line with previous results [188], which is likely due to the shorter bond length of carbon bonds. Further discussion on the carbon slab can be found in Chapter 8.

By comparing the circles and stars or triangles and crosses in Fig. 6.9, it can be observed that the anatase (101) surface shows more positive band offsets compared to the (001) surface, with the former having larger values by 0.46 eV. This difference is attributed to the higher IP and EA of the (101) surface. These findings suggest that the surface orientation plays a significant role in determining the calculated band offsets. Moreover, calculations indicate that the Si(111) reconstruction has smaller IP and EA compared to the Si(001) reconstruction by approximately 0.1 eV, consistent with previous studies [189].

Upon comparing the calculated band offsets using PBE and rSCAN to the previously reported experimental band offsets, as discussed in Section 2.4 and shown as shaded regions in Fig. 6.9, it is apparent that the VBOs of non-oxygenated Si slabs agree well with the experimental values. However, the CBOs are approximately 0.9 eV higher than the reported values, indicating that the Si conduction band is higher in energy than the conduction band of TiO_2. The origin of this discrepancy can be attributed to the calculated EA, where the EA of 4.9 eV is too large compared

Table 6.2: Valence band ΔE_v, conduction band ΔE_c shifts, and resulting band gaps (eV) of TiO_2 calculated using PBE+U.

		PBE+U				
		0	2	4	6	8
TiO_2	ΔE_v	0	-0.01	-0.15	-0.21	-0.24
	ΔE_c	0	0.11	0.141	0.36	0.73
	E_g	2.12	2.24	2.41	2.69	3.09

to the values reported in experimental literature, despite the calculated IP for TiO_2 being in good agreement with experimental values at $\sim$7 eV. The CBO calculated using rSCAN is generally closer to the experimental results than PBE due to the relatively more accurate EA; therefore, it is interesting to consider the effect of exchange-correlation treatment on the calculated band offsets.

6.4.3 Influence of exchange-correlation treatment

The reported large values of calculated EA in the previous section were caused by the "band gap problem" in DFT calculations, as described in Section 3.5. To improve the quantitative accuracy of the band gap calculations, various approaches were considered in this thesis, such as GGA+U [190], hybrid functionals [190, 191], or many-body perturbation theory in the GW approximation [191, 192]. One advantage of the GGA+U approach is that it does not require large computational resources like the hybrid functional does, which makes it suitable for large-scale interface models. The valence and conduction bands in TiO_2 are mainly composed of O-2p and Ti-3d character, as shown in Fig. 6.6a [184]. Therefore, applying the Hubbard U correction with various U values to the strongly correlated Ti-3d orbitals can induce band gap opening [181, 184, 190].

Table 6.2 presents the calculated values of valence and conduction band shift and resulting band gaps of TiO_2 using the PBE+U approach. Fig. 6.10a displays the band offsets obtained through the vacuum-level alignment method for the H-terminated Si:TiO_2(001) interface using PBE+U with varying U values from 0 to 8 eV. Over this wide range of U values, the VBO exhibits high stability, with variations less than 0.2 eV. While this may not be surprising considering the low contribution of Ti-3d orbitals to the valence band, it should be noted that the U parameter also induces lattice expansion [184, 193], which could potentially affect the band edges. On the other hand, the CBO is highly sensitive to the U values, demonstrating a decreasing trend as U increases. These trends align with the behavior of the IP and EA of TiO_2 observed in Fig. 6.8a.

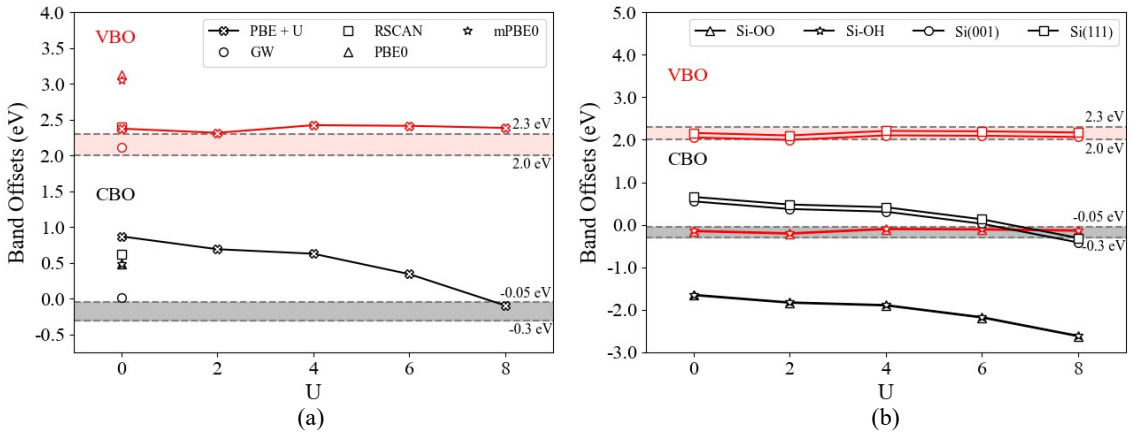


Figure 6.10: Calculated VBOs and CBOs of (a) Si-HH:TiO_2(001) and (b) Oxygen-terminated and reconstructed Si:TiO_2(001) interfaces using PBE+U as the U value increases from 0 to 8 eV. Band offsets obtained using corrected band edges from GW, mPBE0, and PBE0 are also included in the sub-fig. (a).

The U correction is applied to the Ti-3d orbitals that primarily contribute to the conduction band of TiO_2. Therefore, increasing the U value will push the conduction band upward, increasing the band gap and reducing the EA to a more accurate value. Specifically, a band gap of 3.09 eV and an EA of 3.90 eV is achieved for a U value of 8 eV. The correlation of the band gap on the U value in PBE+U calculations is consistent with previous studies [181, 184, 190], although comparing different implementations of PBE+U is not necessarily straightforward.

To further investigate the impact of U on band offsets of the Si:TiO_2 interface, band offsets for reconstructed and oxygen-terminated Si slabs were also calculated using PBE+U following the same procedure, as shown in Fig. 6.10b. Consistently, stable VBOs and decreasing trends in CBOs are observed in these slabs as well. This implies that the GGA+U approach is particularly important for calculating CBOs where, without any correction applied, the TiO_2 conduction band would be erroneously positioned lower in energy than the valence band of the other material, leading to an inaccurate interfacial electronic structure as electrons would occupy TiO_2 conduction states, resulting in metallic behavior [194]. The DOS and band structures of heterointerface Model 1 and Model 2 were further calculated using PBE and rSCAN without any corrections, which also indicate the metallic behavior of the Si:TiO_2 interface. The results of these calculations are presented in Appendix B.

Alternatively, higher levels of theory were used to adjust the band edge positions as a post-processing step, following the approach in Refs. 192 and 194. In Ref. 192, the band edge corrections obtained from the GW approximation were applied to the GGA Si band edges, resulting in shifts of -0.4 eV and +0.2 eV for the valence and conduction bands, respectively. Similarly,

for anatase TiO_2, Ref. 181 reported corrections of -0.14 eV and +1.05 eV. These band edge corrections effectively reduce the VBO by 0.26 eV to 2.11 eV, and the CBO by 0.85 eV to 0.02 eV for the H-terminated interface, illustrated in Fig. 6.10a. It is worth noting that these adjusted band offsets, represented by the circle in the figure, are in good agreement with the band offsets reported in experimental studies.

Moreover, hybrid functionals were also considered for band edge corrections. In Ref. 195, a modified PBE0 (mPBE0) functional was used to obtain band edge shifts of -0.31 eV and +0.28 eV for the Si valence and conduction bands, respectively. The exact exchange fraction α was adjusted to 0.11 to achieve a band gap of 1.2 eV. Another study by Ref. 190 used PBE0 with a modified value of α = 0.18, which was adjusted to yield a self-consistent inverse dielectric constant smaller than a specified threshold. This resulted in band shifts of -0.99 eV and +0.66 eV for anatase TiO_2, leading to an increase in the VBO by 0.68 eV and a reduction in the CBO by 0.38 eV, as indicated by the star in Fig. 6.10a. Additionally, the square symbol in Fig. 6.10a represents the corrected band offsets using the standard PBE0 functional with α=0.25. In Ref. 190, corrections of -1.43 eV and 0.92 eV were reported for TiO_2, while the VBM and CBM shifts for Si were -0.68 eV and +0.53 eV, respectively [191]. These band edge corrections from PBE0 result in an increase in VBO by 0.75 eV and a reduction in CBO by 0.38 eV.

The variation in band offsets in Fig. 6.10a highlight the considerable impact of theoretical approximations on band offsets, especially the CBO. Although DFT+U allows for self-consistent calculations with costs comparable to standard GGA, U values greater than 8 eV are difficult to justify, even though they are necessary to reproduce the band gap of TiO_2. On the other hand, hybrid functionals require significantly more computational resources and extra tests to justify the exchange fraction α. Since GW calculations are the most computationally expensive, they are only feasible here as a non-self-consistent, post-processing step. However, the GW method offers strong theoretical justification, and the corrections can be easily applied since they are intrinsic to the bulk system.

6.4.4 Heterointerface alignments

The band alignments of the Si:TiO_2 interface Models 1–4 in Fig. 6.3 were determined using the heterointerface alignment method. Models 1 and 2 were constructed by placing a TiO_2(001) slab on top of a Si(001) slab but with different types of bonding. In the optimization process of Model 1, half of the oxygen atoms in the TiO_2 bottom layer moved down, while half of the oxygen atoms

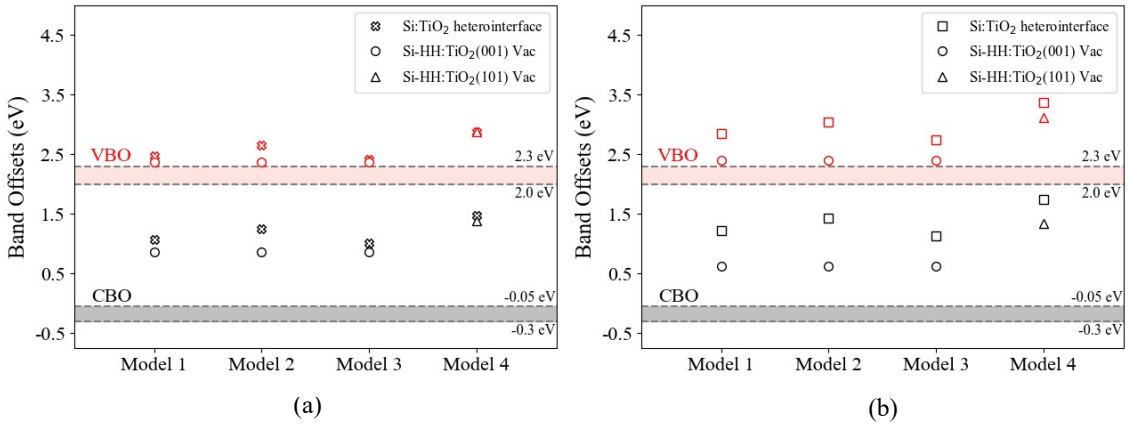


Figure 6.11: Calculated band offsets of Models 1–4 using heterointerface calculations with both (a) PBE and (b) rSCAN along with the band offsets of Si-HH:TiO_2(001) and Si-HH:TiO_2(101) obtained using the vacuum-level alignment method.

in the Si oxygen termination layer moved up, forming Si-O-Ti bridges. The remaining oxygen atoms created Si-O-Si bridges at the Si surface. In contrast, the oxygen atoms in Model 2 were threefold coordinated, compared to the twofold coordinated oxygen atoms in Model 1. The TiO_2 slab moved down during optimization, producing two distinct oxygen sites. The first oxygen site was located between two Si atoms and below a Ti atom. The oxygen atom in this site formed a Si-O-Si bridge and bonded to the above Ti atom. The second oxygen site was located above a Si atom and at the bridge site between two adjacent Ti atoms, creating a Ti-O-Ti bridge at this site. Model 2 was calculated to be more stable than Model 1 by 17 meV (PBE) or 144 meV (rSCAN), per surface Si atom. To investigate the influence of a wider range of bonding types, Model 3 was generated. Although this model had been relaxed such that all atomic forces are zero, it was highly unstable with a thermodynamic instability of +0.9 eV/Si atom compared to Model 2 for PBE calculation. As a results, Model 2 is the most likely match with the heterostructure observed in experimental studies, as it is energetically more stable than the other models considered in this thesis. Model 4 is based on the TiO_2(101) surface and contains a mix of twofold and threefold coordinated O atoms. It should be noted that only a limited number of interface models were taken into consideration, and the interface used in the experiments is likely to be more complex.

Fig. 6.11 displays the band offsets calculated for Models 1-4 using PBE and rSCAN, along with the band offsets of Si-HH:TiO_2(001) and Si-HH:TiO_2(101) obtained using the vacuum-level alignment method. The band offsets obtained using the heterointerface alignment method with the PBE functional are comparable, within 0.4 eV, to those obtained for the H-terminated Si slab using the vacuum-level alignment method, but not to those of O-terminated slabs, which are ap-

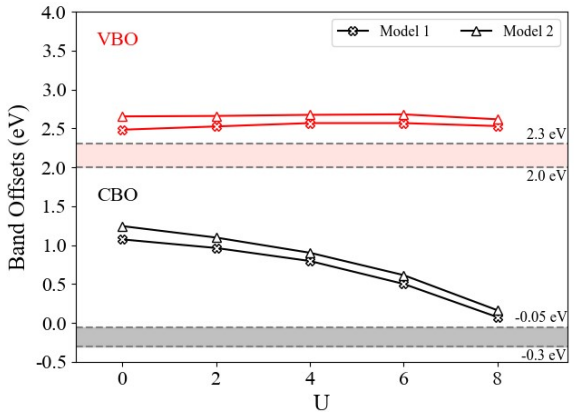


Figure 6.12: Calculated band offsets of Model 1 and Model 2 using PBE+U as the U value increases from 0 to 8 eV.

proximately 2 eV lower, as shown in Fig. 6.9. This suggests that although Models 1–4 are based on O-terminated slabs, the O-layer does not have the same significant impact when the TiO_2 slab is explicitly included. More generally, the agreement between the vacuum and heterostructure aligned offsets provides some support for the use of the vacuum-level alignment method in experimental literature to generate band diagrams [98–100]. However, this agreement is not consistent when using rSCAN, as the difference between offsets obtained using these methods increases to approximately 0.6 eV, as shown in Fig. 6.11b. This discrepancy might be related to the relatively higher lattice mismatch induced by the rSCAN functional, discussed in later Section 6.4.5. Similarly to PBE, the previously dramatic effect of oxygen-terminated Si is not observed when using rSCAN.

Models 1–3 show that the presence of different bonding types results in band offset variations of around 0.3 eV. However, despite the unusual bonding in Model 3, its band offsets are similar, differing only by 0.07 eV from the much more ordered Model 1. A more significant effect is observed for Model 4, which has band offsets that are 0.40 eV and 0.52 eV higher than Model 1 when using PBE and rSCAN, respectively. This observation is consistent with the results of the vacuum alignment calculations in Fig. 6.9, indicating the importance of surface orientation.

Upon further examination of the exchange-correlation treatment, the band offsets of Model 1 and Model 2 were calculated using the PBE+U approach, as shown in Fig. 6.12. Consistent with the trends observed in Fig. 6.10, VBOs of these models remain relatively constant as the value of U increases from 0 to 8 eV, while the CBOs are more sensitive with various U values. Notably, variations in band offsets induced by different bonding types between Model 1 and Model 2 are clearly observed for all values of U. To obtain comparable band offsets with the reported

Table 6.3: Calculated VBOs and CBOs (eV) of Si:TiO_2 interface models using corrected band edges obtained from PBE0, mPBE0, and the GW approximation.

	Si:TiO_2 interface models			
PBE0	Model 1	Model 2	Model 3	Model 4
VBO	3.23	3.40	3.17	3.63
CBO	0.68	0.86	0.62	1.08
mPBE0				
VBO	3.16	3.33	3.10	3.56
CBO	0.69	0.87	0.63	1.09
GW				
VBO	2.22	2.39	2.15	2.62
CBO	0.22	0.39	0.15	0.62

values in the literature, post-processing GW corrections [181, 192] and corrections from hybrid functionals [190,191,195] were applied to the PBE band edges for Model 1–4. The corrected band offsets of Models 1–4 are presented in Table 6.3, and the resulting GW-corrected band alignments are shown in Fig. 6.13. For Models 1–3, constructed using TiO_2(001), the VBOs fall in the range 2.1–2.4 eV, while the CBOs are in the range 0.1–0.4 eV. These values align closely with the GW-corrected vacuum-aligned offsets in Fig. 6.10a, where the VBO is 2.11 eV and the CBO is 0.02 eV. In contrast to experimental studies in Section 2.4, which report a type I band alignment with a slightly negative CBO between Si and TiO_2, the calculated positive CBOs in Fig. 6.13 indicate a type II band alignment (Fig. 1.1b) with the TiO_2 conduction band being slightly lower in energy than the Si conduction band. However, the difference between the calculated CBO and zero is small enough to fall within the error bars of the heterointerface alignment method, especially given the highly idealized model of the interfaces that were constructed.

6.4.5 Effects of lattice mismatch on the band alignments

The TiO_2 slab in Models 1–4 was built using the relaxed Si lattice parameters, resulting in strain being applied to the slab. Specifically, the PBE results showed that the TiO_2(001) surface was subjected to a lateral strain of +1.7%, while the (101) surface experienced strains of +4.8% and -2.0% in the two perpendicular directions. Using the rSCAN functional, the (001) surface had a lateral strain of +1.9%, while the (101) surface experienced strains of +5.2% and -1.5% in the two

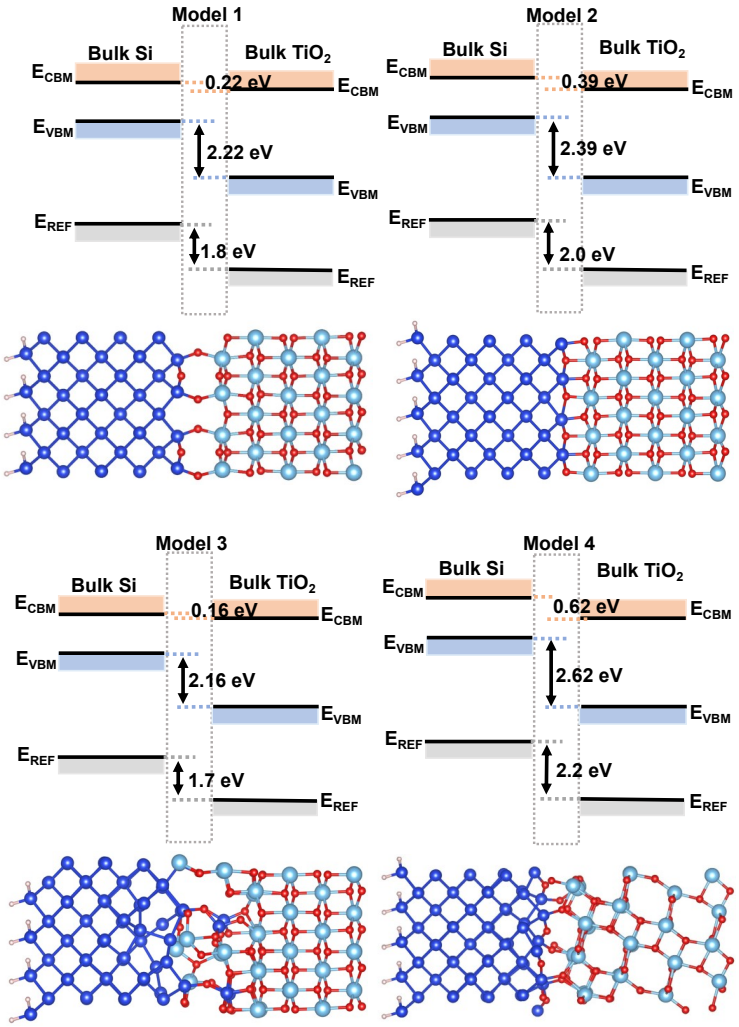


Figure 6.13: Calculated band offsets of Models 1–4 using a post-processing step that applies the band edge correction from GW calculations to the PBE band edges. E_{REF} is the reference potential used in the alignment.

perpendicular directions. To examine the effects of lattice mismatch on the band alignments of the Si:TiO_2(001) interface model, Model 1 and Model 2 were constructed using the in-plane lattice parameters of TiO_2 instead of Si. The resulting band offsets were compared to those of previous interface models constructed with Si lattice constants, shown in Fig. 6.14. The VBOs of the interface models with TiO_2 in-plane lattice parameters were higher than those of the models using Si lattice constants, increasing by approximately 0.1 eV and 0.2 eV using PBE and rSCAN, respectively. The CBOs of Model 1 and Model 2 decreased by 0.1 eV with the TiO_2 in-plane lattice parameters. These results demonstrate that different lattice mismatches impact the band alignments of the Si:TiO_2 interface model, highlighting the importance of considering strain effects in future investigations of the Si:TiO_2 interface.

To further examine the effects of strain on band alignments, vacuum-level alignments for the

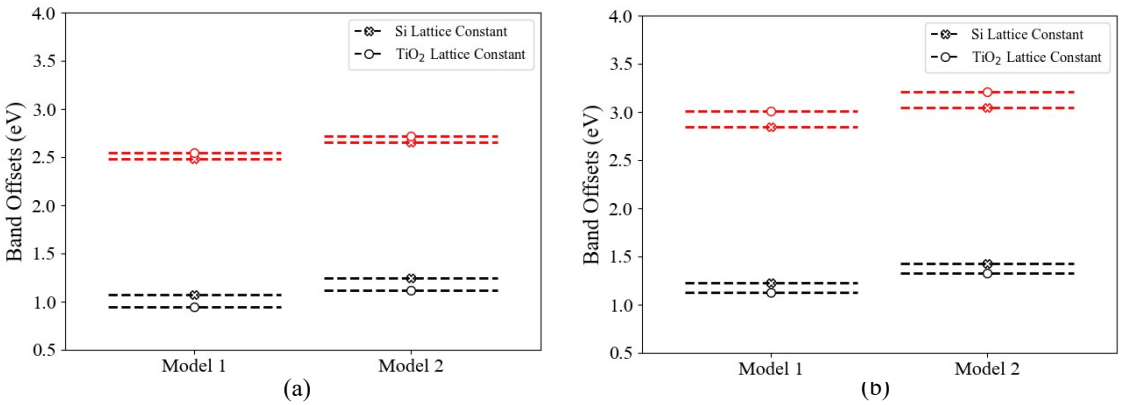


Figure 6.14: Calculated VBOs (red dotted line) and CBOs (black dotted line) of Si:TiO_2(001) interface models constructed using in-plane lattice parameters of Si and TiO_2 with (a) PBE and (b) rSCAN.

TiO_2(101) surface were recalculated in the situation where the surface is constructed using the Si lattice parameters, which was placed under the above +4.8 and -2.0% strains. The resulting calculated offsets for the strained TiO_2(101) surface were approximately 0.33 eV higher than those obtained using the natural lattice constants. This suggests that the higher band offsets observed in the Si:TiO_2(101) interface model is attributed to both the change in surface orientation of TiO_2 and lattice mismatch.

6.5 Conclusion

This chapter has first dealt with the structural and electronic properties of bulk Si and anatase TiO_2. The calculated band gaps using PBE and rSCAN are found to be smaller than experimental data [38, 180], leading to inconsistencies when calculating EA and CBO. To investigate the dependence of band offsets on the structural features of the Si:TiO_2 interface, several Si:TiO_2 interface models were created using the optimal lattice parameter. The band offset calculations were performed using the vacuum-level alignment and heterointerface alignment methods, following the approaches described in Section 4.2. For almost all interfaces models considered, sizeable VBOs of order 2 eV are found with the exception of O-terminated Si slabs in which the calculated VBOs are significantly smaller by 2.1 eV. However, these large differences are not shown in the heterointerface calculation even though the Si slab is terminated with oxygen. This shows that the TiO_2 overlayer effectively screens the large surface dipole of the O-terminated Si surface.

To address the impact of the "band gap problem" on band offsets, calculations beyond the standard GGA level calculation are applied in order to obtain more accurate band gaps. The

DFT+U and post-processing results show that the VBOs are independent of theoretical approaches and insensitive to the Hubbard U value. However, the CBOs are found to be much more sensitive, exhibiting a reduction of approximately 1 eV as the Hubbard U value varies between 0 to 8 eV. Applying a post-processing GW correction [181, 192] also yields a similar reduction in CBOs. The GW-corrected values are considered to be the most accurate, resulting in CBOs on the order of 0.02 eV in vacuum-level alignment and 0.15 eV in heterointerface alignment.

As previously mentioned, the positive CBOs calculated in this study correspond to a shift from Type I to Type II alignment, in contrast to previously reported results with slightly negative CBOs (Section 2.4). Unlike the very large VBO which acts as a barrier to prevent the flow of holes, the calculated similarity in the positions of the conduction band edges of Si and TiO_2 show that small changes in the relative band positions can enable or prevent carrier transport (electrons) across the interface. Even though the forming of a disordered array of bonds as in Model 3 does not lead to a significant change in band offsets compared to the highly ordered Models 1 and 2, the band calculations in this chapter show that the formation of different types of bonds (twofold or threefold coordinated O), different anatase surface orientations, or application of strain can account for this shift. Therefore, the device performance is expected to be sensitive to the fabrication methods.

Chapter 7

Infrared spectra of Si, TiO_2 slabs, and Si:TiO_2 interface models

7.1 Introduction

In Chapter 6, I have proposed three Si:TiO_2(001) interface models with different types of interfacial bonds. Among these models, Model 1 and Model 2 are more likely to match the heterointerface that appeared in experimental studies due to their relatively smaller energy compared to Model 3. Unfortunately, there is a lack of theoretical and experimental studies to characterize the structural features of the Si:TiO_2(001) interface, which makes it difficult to systematically compare the proposed models with the experimental heterointerface. To partially fill this gap, the infrared absorption spectra of Model 1 and Model 2 were calculated following the method in Section 4.3. In the absence of experimental infrared measurements for the Si:TiO_2 interface, the calculated vibrational modes were compared with experimentally measured frequencies for related systems. The vibrational frequencies of isolated oxygen-terminated Si and TiO_2 slabs were first calculated. The results were then compared with experimental frequencies to assess the accuracy of the calculation. Then, infrared absorption spectra of the Si:TiO_2 interface were calculated.

7.2 Constructing slabs and interface models

The slab and interface models were reconstructed using similar methods as described in Section 5.3.1 by optimizing the slab with fixed lattice parameters obtained from bulk calculations. The oxygen-terminated Si(001) slab is the primary focus of this chapter since the interface models

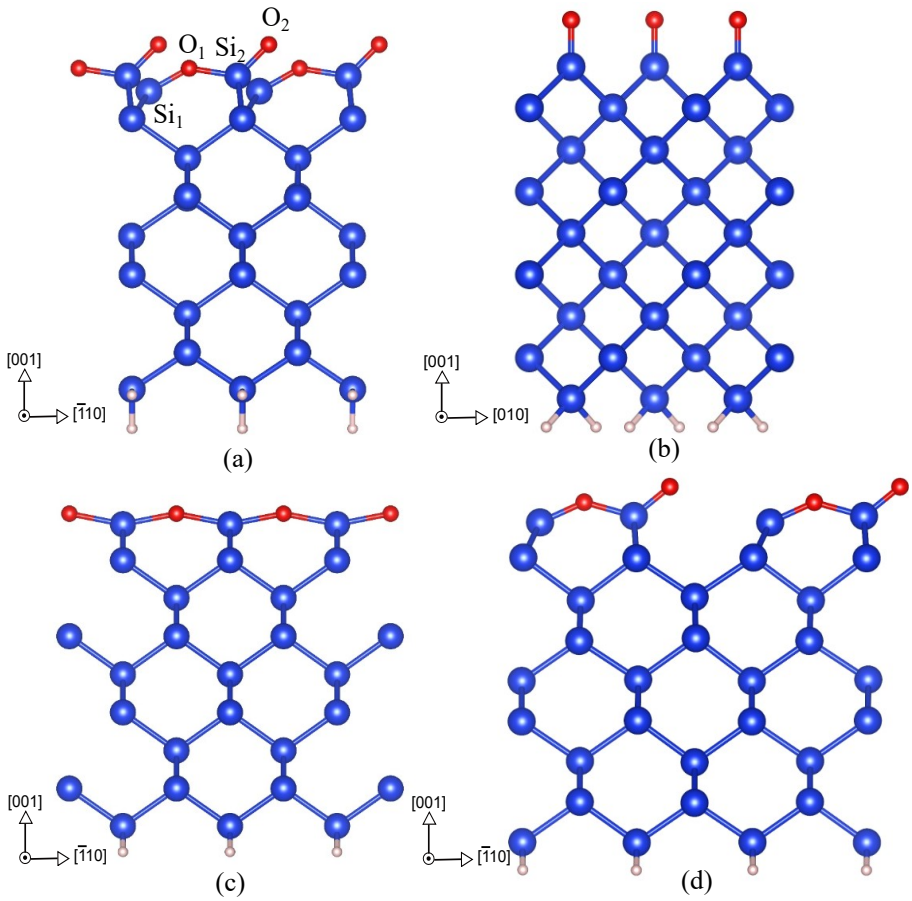


Figure 7.1: (a) 2×2 reconstructed, (b) ketone, (c) ether, (d) 2×1 reconstructed Si(001) slabs with hydrogen passivated at the lower surface. Si/H/O atoms are shown in blue/pink/red, respectively.

were constructed based on this slab. The optimized oxygen-terminated Si slab contains mixed ether and ketone forms, resulting in a 2×2 reconstructed surface as shown in Fig. 7.1a. This surface is calculated to be more stable than pure ketone (Fig. 7.1b) and ether (Fig. 7.1c) Si slabs by 0.6 eV and 0.5 eV per Si surface atom, respectively. A 2×1 reconstructed slab in Fig. 7.1d was also considered and found to be more stable than pure ether and ketone slabs, but less stable than the 2×2 reconstructed Si slab. As a result, the infrared calculations were performed on the 2×2 reconstructed Si slab. Additionally, the infrared spectra of the ketone Si slab, which involves placing the oxygen atom directly above or below a surface Si, was calculated for comparison purposes. The dangling bonds on the lower surface of these Si slabs were passivated with hydrogens. The lateral dimensions of both Si slabs are approximately 6 Å×6 Å, with a thickness of 12 Å, and a vacuum region of 24 Å along the z-axis between the periodic slabs. The TiO_2 slab has lateral dimensions of 4 Å×4 Å, a thickness of 20 Å, and a vacuum region of 23 Å. The Si:TiO_2(001) interface model's lateral dimension is halved from its initial value in order to decrease computational

cost while keeping the rest of the structural parameters.

7.3 Computational details

All calculations presented in this chapter followed the same computational methodology described in Section 5.3.2, except that the Quantum ESPRESSO package [149] was used instead of CASTEP [112]. Although both packages use plane wave based DFT, it is not appropriate to use the lattice parameter obtained from CASTEP in Quantum ESPRESSO calculations because of the different pseudopotentials used. When using the CASTEP package, on-the-fly generated Vanderbilt ultrasoft pseudopotentials were used, which are constructed by the built-in pseudopotential generator in CASTEP. For Quantum ESPRESSO calculations in this thesis , ultrasoft pseudopotentials from the "BRV" open-source pseudopotential library were used, which are generated using the Vanderbilt pseudopotential generation code [196]. A fully-relaxed structure is required for accurate phonon calculations. Therefore, the structural parameters were re-optimized through geometry optimization calculations until the force acting on each atom was less than 3×10^{-5} eVÅ^{-1}. Convergence tests were conducted to determine the appropriate cutoff energy for wavefunctions and charge density, as well as the k-point sampling. These tests are described in Section A.5 of Appendix A. As a result, plane wave energy cutoffs of 65 Ry and 650 Ry for the wavefunction and the charge density were used. Once the optimized geometry was achieved, consecutive self-consistent field (SCF) calculations were performed on structures that were generated by the $Phonopy$ package [150, 151] with an atom being displaced from its relaxed position in order to extract the force acting on every atom and build the force constant matrix. A $6\times6\times1$ k-point sampling was used within the Monkhorst-Pack scheme [160] for optimization and SCF calculation. The vibrational modes of all structures were calculated at the Γ point. The non-analytical term in the dynamical matrix was included by calculating the Born effective charges and dielectric constant using the $ph.x$ program from the Quantum ESPRESSO package [149].

7.4 Infrared spectra

7.4.1 Infrared spectra of Si slabs

The surface Si-Si and Si=O bond lengths in the ketone slab (Fig. 7.1b) are calculated to be 2.35 Å and 1.54 Å, respectively. These findings are in reasonable consistency with the experi-

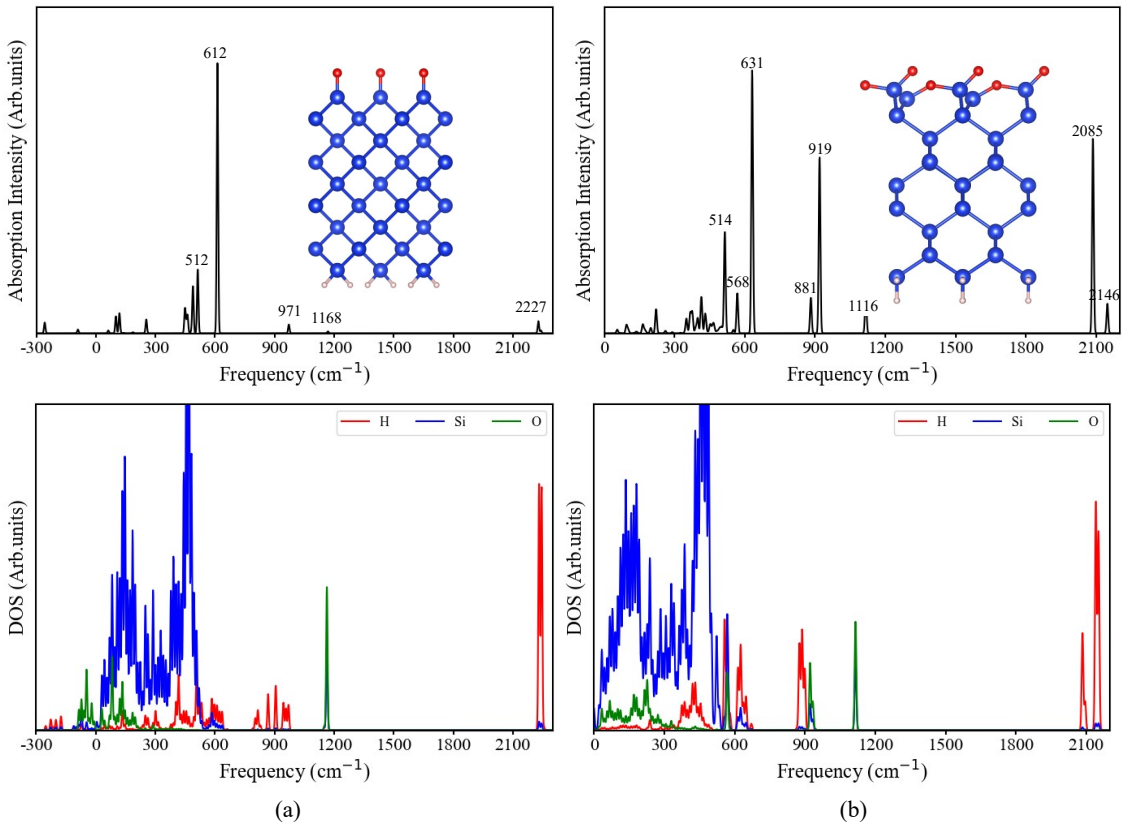


Figure 7.2: Infrared spectra of (a) the oxygen-terminated ketone and (b) the 2×2 reconstructed Si slabs along with their corresponding vibrational DOS plots shown below them. Gaussian broadening of 5 cm^{-1} is applied for the infrared spectra and the DOS plot.

mentally determined Si-Si bond length of 2.35 Å in Si crystals and the Si=O bond length of 1.52 Å in H_2SiO system [168, 197]. On the other hand, the 2×2 reconstructed Si slab contains two distinct atomic sites of oxygen, labeled as O_1 and O_2 in Fig. 7.1a. The calculated bond lengths of the Si_1-O_1 and Si_2-O_1 appearing in the ether configuration are 1.62 Å and 1.72 Å, respectively. The Si_1-O_1-Si_2 bond angle is calculated to be 142°, which agrees with the Si-O-Si bond angle of 143° measured for silica [198]. The Si_2=O_2 bond length appearing in the ketone configuration is 1.55 Å. Furthermore, the 1×1 O-terminated Si(100) slab with ether configuration (Fig. 7.1c) given in Ref. 168 was also investigated, yielding a Si-O bond length of 1.96 Å and a Si-O-Si angle of 160°, similar to the results given in this reference.

Table 7.1 displays the numerical values of calculated vibrational frequencies, along with the corresponding experimental values measured for related systems. Figure 7.2 presents the calculated infrared spectra of the oxygen-terminated ketone and 2×2 reconstructed Si(001) slabs, as well as their calculated vibrational DOS. To make the comparison more meaningful, Table 7.2 provides some details of the references used for comparison. Based on the vibrational DOS plot

Table 7.1: Calculated infrared modes of the ketone and 2×2 reconstructed Si(001) slabs along with the experimentally measured vibrational frequencies of related systems. The symbol s and b represent the stretching and bending modes, respectively.

Mode	Frequency (cm^{-1})			References
	Ketone	2×2 reconstructed	Expt.	
Si-H s	2227	2146, 2085	2086, 2089	[199, 200]
Si-H b	612, 971	881, 631	876, 600-630	[200, 201]
Si-O-Si s	-	1116	800, 1050-1150	[202–204]
Si-O-Si b	-	568	488	[205]
Si-O s	1168	919	890, 840	[199, 200]

and the visualization of the vibrational modes generated by the $Phonopy$ package [150, 151], the Si-H stretching mode of the ketone Si slab is located at 2227 cm^{-1}, which is higher than the experimental Si-H stretching region at 2086 cm^{-1} for the H_2O-saturated Si(100) surface by 141 cm^{-1} [199]. The small vibrational peak identified at 1168 cm^{-1} corresponds to the motion of Si-O stretching, resulting in a large discrepancy of 270 cm $^{-1}$ compared with the Si-O stretching region at 890 cm $^{-1}$ for H_2O-exposed Si(100) surface [200]. The peaks at 971 cm^{-1} and 612 cm^{-1} correspond to Si-H bending modes, respectively. While the Si-H bending mode agrees with experimental frequencies ranging from 600 cm^{-1} to 630 cm^{-1} for the H_2O-exposed Si(001) surface [200], a discrepancy of 95 cm^{-1} is found for the Si-H bending mode at 971 cm^{-1} compared to the experimentally and theoretically determined frequency at 876 cm^{-1} for the HSi-O_3 system [201,206]. It is worth noting that there are negative frequencies in Fig. 7.2a, demonstrating that the atoms in the ketone Si slab are displaced away from their equilibrium positions. Specifically, according to the DOS plot, the vibrational mode at -257 cm^{-1} corresponds to the Si-H bonding, which indicates that the hydrogen atoms in the ketone slab are not at their equilibrium positions. However, this negative Si-H vibrational frequency is not shown in the 2×2 reconstructed Si slab (Fig. 7.2b), where the hydrogen atoms move from the symmetric configuration to the canted configuration. This observation indicates that the canted configuration represents the equilibrium positions for the hydrogen-terminated Si slab. Therefore, in this case, the force constant matrix constructed for the ketone Si slab is not reliable since the relaxed structure is not a true minimum of the potential energy surface, which might explain the discrepancies found when

Table 7.2: Description of the experimental studies used in this chapter for comparison purposes. The references in this table contain the vibrational frequencies of particular structures observed in the Si slabs or Si:TiO_2 interface models.

References	Systems	Comments
199	H_2O-saturated Si(100)-(2×1) surface	Infrared spectra was obtained after annealing the surface to 27°C.
200	H_2O-exposed Si(001) surface	The Si surface was exposed to varying doses of H_2O at -53°C
201	$HSi-(OSi)_3$	Ref. 206 confirmed the results for the Si-H bending mode theoretically.
202	Titania-silica aerogels mixed with oxides (TiO_2-SiO_2)	The infrared spectra was obtained after the aerogels calcined in air at 600°C
203	Titanium silicate ($Ti_xSi_{(1-x)}O_2$) thin film	This thin film was fired at 600°C with various compositions.
204	Silica gel obtained from $Si(OC_2H_5)_4$	The infrared spectra was obtained after the gel was heated to 40, 250, 400 500°C.
205	SrO-Al_2O_3-B_2O_3-SiO glass	Infrared spectra was measured after gamma-ray irradiation with a dose of 30 kGy
207	Titania-silica mixed oxides (TiO_2-SiO_2)	The interaction between TiO_2 and SiO_2 is strongly depend on the preparation conditions

compared with experimental measurements.

Indeed, the calculated vibrational frequencies of the more stable 2×2 reconstructed Si slab in Fig. 7.2b are in closer agreement with experimental measurements except for low-frequency Si-O-S mode. From the highest to lowest frequencies, the calculated peaks can be assigned as follows: Si-H stretching at 2146 cm^{-1} and 2085 cm^{-1}, symmetric Si-O-Si stretching at 1116 cm^{-1}, Si-O stretching at 919 cm^{-1}, Si-H bending at 881 cm^{-1} and 631 cm^{-1}, and Si-O-Si bending at 568 cm^{-1}. The peak located at 512 cm^{-1} and 514 cm^{-1} measured for both slabs represent the Si-Si stretching mode; therefore, vibrational peaks below 550 cm^{-1} are typically not considered since they primarily correspond to the vibrational model within bulk Si, which makes it hard to identify the vibrational mode at the surface. Accordingly, the experimental frequencies with their corresponding vibrational mode are given in Table 7.1. The calculated Si-O-Si stretching mode at 1116 cm^{-1} falls within the frequency range of 1050 cm^{-1} to 1150 cm^{-1}, which has been experimentally determined for both titania-silica aerogels [202] and titanium silicate thin film [203].

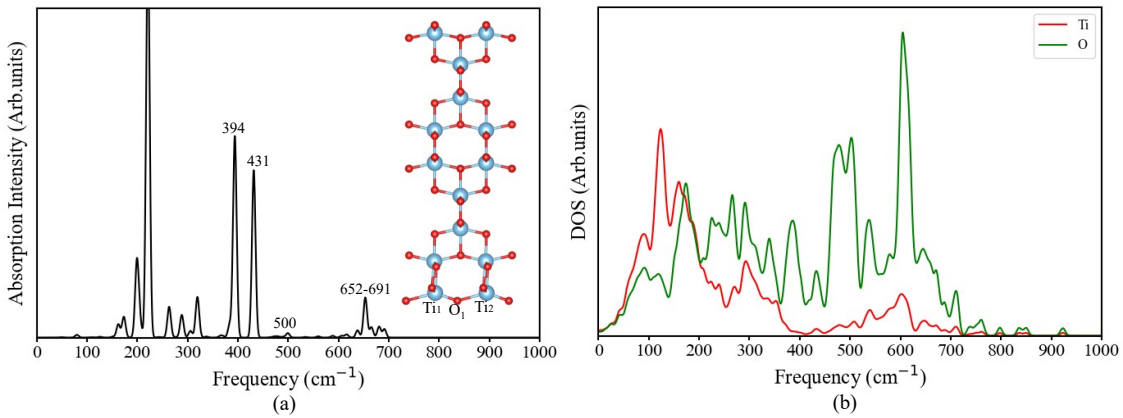


Figure 7.3: (a) Infrared spectra of the anatase TiO_2(001) slab along with the corresponding (b) vibrational DOS plot. Gaussian broadening of 5 cm^{-1} is applied for both plots.

However, the calculated Si-O-Si bending mode at 568 cm^{-1} is higher than the experimental value of 488 cm^{-1} for SrO-Al_2O_3-B_2O_3-SiO glass [205]. Still, the agreement between the experimental and calculated values supports the accuracy of the calculations, which then consider moving forward to calculate the infrared spectra of the Si:TiO_2 interface models.

7.4.2 Infrared spectra of the anatase TiO_2 slab

The calculated infrared spectra and vibrational DOS for the anatase TiO_2(001) slab are shown in Fig. 7.3. The labeled Ti_1-O_1 and Ti_2-O_1 bond lengths of this relaxed TiO_2 slab were determined to be 1.74 Å and 2.24 Å, respectively. These values are consistent with previously reported bond lengths at the anatase TiO_2(001) surface with values of 1.76 Å and 2.20 Å [90]. The Ti_1-O_1-Ti_2 angle was calculated to be 145°, which agrees well with the reported value of 146° in the above reference.

The absorption peaks calculated in this study were compared with experimental values from Ref. 208 and Ref. 209, both of which concentrated on anatase TiO_2. The broad absorbance band observed between 652 cm^{-1} and 691 cm^{-1} in the calculated spectra agrees well with the experimental frequencies in Ref. 209, which were measured at 690 cm^{-1} and 700 cm^{-1}. Ref. 208 also noted that the peaks at 700 cm^{-1} formed a very broad band. The calculated peaks at 394 cm^{-1} and 431 cm^{-1} were found to be shifted in frequency by about 40 cm^{-1} from the experimental peaks at 347 cm^{-1} and 470 cm^{-1} [209]. This shift was also observed when comparing the small peak at 500 cm^{-1} to the experimental peak at 525 cm^{-1} [208].

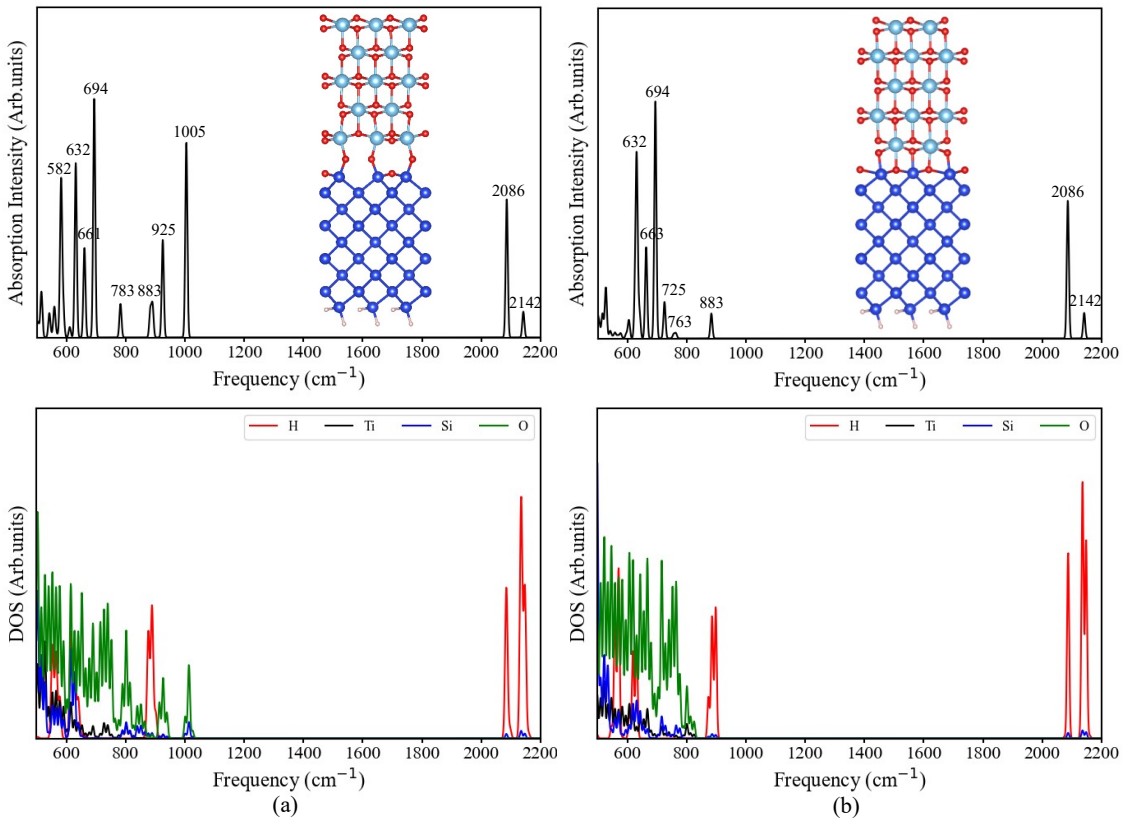


Figure 7.4: Infrared spectra of (a) Model 1 and (b) Model 2 along with their corresponding vibrational DOS plots shown below them. Gaussian broadening of 5 cm^{-1} is applied for both plots

7.4.3 Infrared spectra of Si:TiO_2(001) interface models

Fig. 7.4 illustrates the calculated infrared spectra of Model 1 and Model 2 along with their corresponding vibrational DOS plots. The Si-H stretching modes are assigned to the absorption peaks at 2142 cm^{-1} and 2086 cm^{-1} in Model 1, while the Si-bending modes are identified at 883 cm^{-1} and 632 cm^{-1}. These identified modes are consistent with those measured in the 2×2 reconstructed Si slab, as well as the experimental Si-H vibrational modes in Table 7.1 for the H_2O-saturated Si and the HSi-$(OSi)_3$ systems [199–201]. The peaks at 1005 cm^{-1} and 783 cm^{-1} are associated with the symmetric and asymmetric Si-O-Si stretching modes, which is in reasonable agreement with the modes identified for the titania-silica aerogels [202] and the silica gel [204] with frequencies at 1050 cm^{-1} and 800 cm^{-1}, respectively. The presence of the absorption peaks at 925 cm^{-1} is determined to be Ti–O–Si stretching mode, similar to the experimental study on the titania-silica mixed oxides [207] with corresponding frequencies ranging from 910–960 cm^{-1}. The rest of the absorption peaks below 700 cm^{-1} are related to the vibrational modes of the anatase TiO_2 and Si slabs.

In contrast to Model 1, the vibrational features of the Model 2 interface exhibit significant differences, except for the Si-H stretching and bending modes which appear at 2142 cm^{-1}, 2086 cm^{-1}, 883 cm^{-1}, and 632 cm^{-1}. Unlike Model 1, there are no absorption modes found for Model 2 at the 1000 cm^{-1} region, demonstrating the absence of the Si-O-Si and Ti-O-Si bonds compared to Model 1. This difference between the two models is also evident by looking at their structural diagram presented in Fig. 7.4, where Model 1 exhibits the Si-O-Si and Si-O-Ti bonds. In contrast, Model 2 contains threefold coordinated oxygen atoms bonded with either two Si and one Ti or vice versa within the interface. The vibrational peaks at 725 cm^{-1}, 763 cm^{-1}, and 663 cm^{-1} are attributed to the vibrational motion of the threefold coordinated oxygen atoms in Model 2, while the 694 cm^{-1} peak corresponds to the motion of Ti-O-Ti in the TiO_2 slab.

7.5 Conclusion

This chapter has focused on calculating the infrared spectra of two Si:TiO_2 interface models, presented as Model 1 and Model 2 in Fig. 6.3. Based upon the finite displacement method described in Section 4.3, the calculations were first carried out on the isolated Si and TiO_2 slabs to confirm the accuracy of the calculation. In fact, the identified vibrational modes for the ketone Si slab were inconsistent with those experimental measured for similar systems, likely due to its relatively unstable structure. The vibrational modes of the 2×2 reconstructed Si slab, on the other hand, were in good agreement with experimental measurements [199–203, 205]. While discrepancies of 40 cm^{-1} were observed in the TiO_2 infrared spectra, the overall peaks identified were reasonably consistent with experimental data for anatase TiO_2 [208, 209].

The infrared calculations were then carried out for Model 1 and Model 2. As there are no available experimental infrared studies on the Si:TiO_2 interface, the calculated vibrational frequencies of Model 1 were compared to experimental measurements for systems related to the Si:TiO_2 interface [204, 207]. The Si-O-Ti and Si-O-Si bonds in Model 1 were found to correspond to the peaks in the region around 1000 cm^{-1}. However, these corresponding vibrational frequencies were not present in the calculated infrared spectra of Model 2. Therefore, by examining the vibrational frequencies in the 1000 cm^{-1} region, experimental studies can determine whether their Si:TiO_2 interface has more similarity to Model 1 or Model 2

Chapter 8

DFT calculations of C slabs

8.1 Introduction

According to the vacuum-level alignment calculations in Section 6.4.2, a 2.1 eV reduction in band offsets is found for the 2×2 reconstructed oxygen-terminated Si slab. This dramatic reduction mirrors the behavior of the EA found for the C(001) surface in Ref. 188. However, unlike the most stable 2×2 reconstructed oxygen-terminated Si(001) surface that comprised both ether and ketone configurations, Ref. 188 only proposed the isolated ether and ketone configurations for the oxygen-terminated C(001) surface. Therefore, it is possible that there exists an even more stable oxygen-terminated C(001) slab with the 2×2 reconstructed surface, similar to the Si(001) surface. To investigate this hypothesis, the stabilities and EAs of the ether, ketone, and 2×2 reconstructed C(001) slabs were calculated. Additionally, the 2×1 reconstructed C(001) slab was considered as another possible stable configuration. The results were compared with the given values in Ref. 188 to make sure the consistency of the calculations. The infrared calculations were then conducted for the optimized ether and ketone C(001) slab in order to identify their distinct bond types. Finally, the stabilities and EAs of the canted hydrogen-terminated Si and C slabs were calculated to investigate their potential effects on band offsets compared to the symmetric hydrogen-terminated slabs.

8.2 Constructing C slabs and computational details

Following the oxygen-terminated Si slab in Fig. 6.1d, the 2×2 reconstructed C slab was constructed by replacing the Si atoms with the C atoms and using the relaxed lattice parameters of

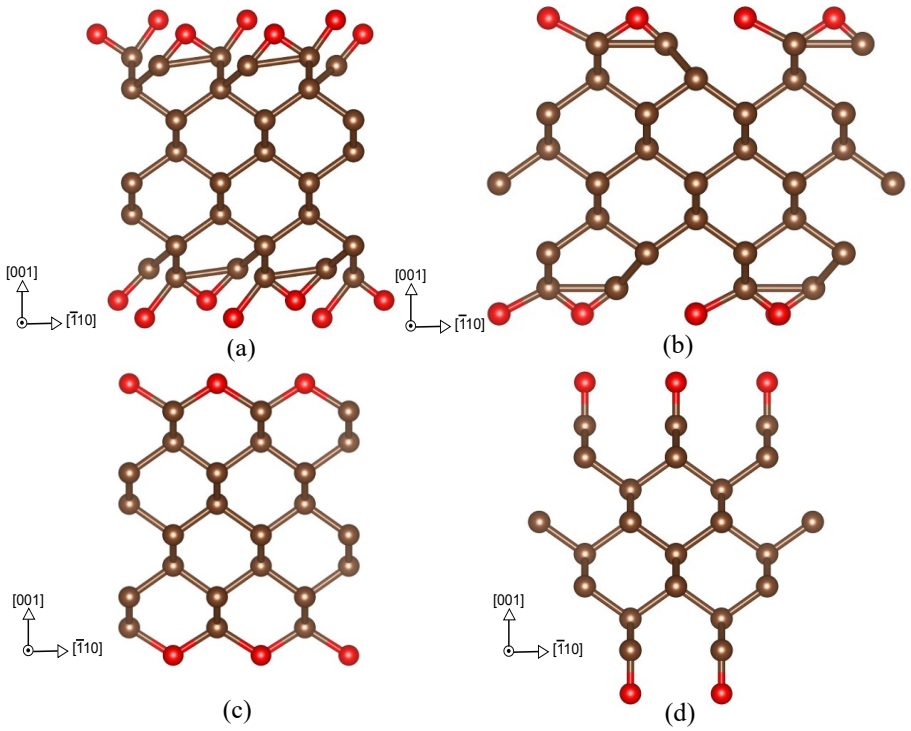


Figure 8.1: Four possible configurations for the H-terminated C(001) surface. (a) 2×2 reconstructed, (b) 2×1 reconstructed, (c) ether, and (d) ketone C(001) slabs. C and H atoms are shown in brown and pink, respectively.

C from the bulk calculation, as shown in Fig. 8.1a. This reconstructed C slab has approximate lateral dimensions of 3.5 Å×3.5 Å (4 surface atoms) and a thickness of 8 Å (8 atomic layers), with a vacuum region of 10 Å separating periodic replicas along the surface normal. For the 2×1 reconstructed slab as shown in Fig. 8.1b, a larger cell with dimensions of 7 Å×7 Å (16 surface atoms) was used while maintaining the same thickness and vacuum region. The ether and ketone configurations were constructed based on Fig. 3 in Ref. 188 with the lateral dimensions, thickness, and vacuum region in line with 2×2 reconstructed C, shown in Fig. 8.1c and Fig. 8.1d.

The computational details for optimizing C slabs here are similar to the detail presented in Section 5.3.2 with the exception of using the LDA functional [117, 118] with a 700 eV cutoff energy in order to match with Ref. 188, which also used the LDA functional, for a reasonable comparison. A k-point sampling of 4×4×1 was used for the 2×1 reconstructed slab, while 8×8×1 was used for the remaining slabs. The smaller k-point grid used for the 2×1 reconstructed slab arises from the fact that it is a 2×2 surface cell in which its lattice parameters are twice larger than the other slabs. The infrared calculations were carried out following the same procedure outlined in Section 7.3, but with cutoffs of 55 Ry and 550 Ry for charge density. The convergence tests for cutoff energy and k-point sampling are detailed in Section A.6 of Appendix A.

Table 8.1: Calculated energies per surface C atom and EAs (eV) of various oxygen-terminated C(001) surfaces along with the calculated results in Ref. 188. 0 eV in energy indicates the most stable structure, acting as a reference energy for better comparison. The calculations for 2×2 and 2×1 reconstructed surfaces were carried out using input structure without optimization.

Oxygen termination	Calc. Energy/ C atom	Energy/ C atom in Ref. 188	Calc. EAs	EAs Ref. 188
Ether	0	0	2.60	2.61
ketone	0.6	0.5	3.73	3.64
2×2 reconstruction	4.73	-	-	-
2×1 reconstruction	5.78	-	-	-

8.3 Stabilities and EAs of oxygen-terminated C slabs

The optimization calculation was first performed in order to find the structure with the lowest energy. After optimization, the 2×2 and 2×1 reconstructed C slabs relaxed to a pure ether structure in which the oxygen atoms are all placed between carbon atoms and form a bridge, in line with the configuration present in Fig. 3b in Ref. 188. This finding is contrary to the idea proposed that the 2×2 reconstructed C(001) slab is expected to be more stable than pure isolated slabs, as observed in the Si(001) slabs. This difference between the silicon and diamond surfaces is attributed to the relatively short C-C bond length compared to Si.

Calculations were then carried out for ketone and ether C slabs, demonstrating that the ether structure is more stable by approximately 0.6 eV per surface carbon atom, consistent with the findings in Ref. 188. The calculated EAs for ether and ketone C slabs are 2.60 eV and 3.73 eV, respectively. These calculated EAs are in good agreement with EA values of 2.61 and 3.64 eV in Ref. 188. These calculation results are given in Table 8.1 along with the corresponding calculated values in Ref. 188 for a clear comparison.

8.4 Infrared spectra of oxygen-terminated C slabs

Fig. 8.2 shows the calculated infrared spectra and vibrational DOS for C(001) slabs with ether and ketone configurations. In the case of the ether slab, the peaks observed above 550 cm^{-1} correspond to the vibrational motion of the carbon atoms within the slab, except for a small peak located at 981 cm^{-1}. This peak is attributed to the stretching mode of C-O-C and falls within the C-O-C stretching region (900–1300 cm^{-1}) reported for polyurethanes [210]. Peaks at 527 cm^{-1}

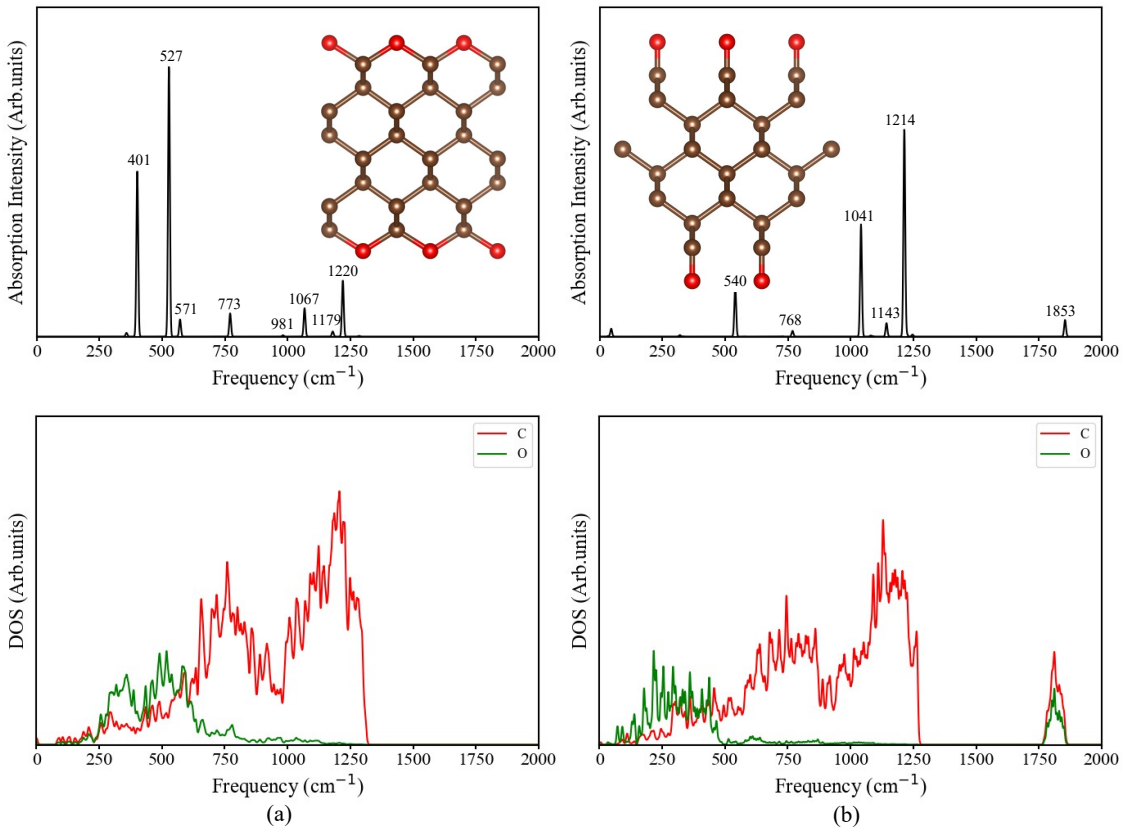
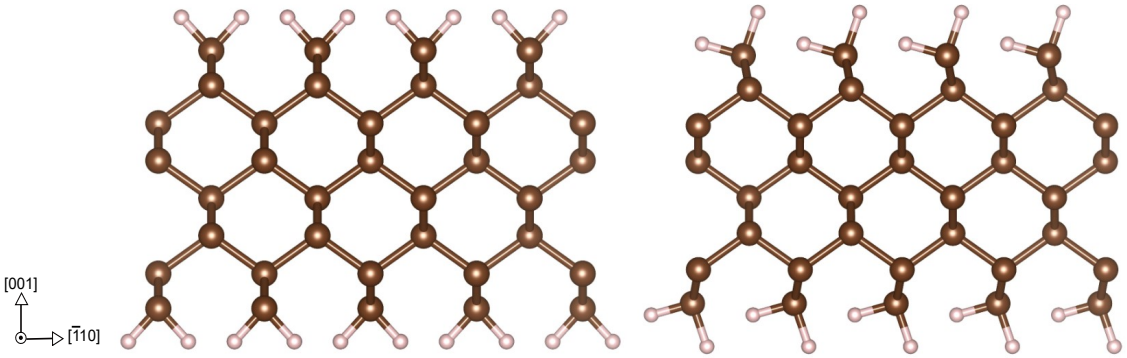


Figure 8.2: Infrared spectra of the (a) ether and (b) the ketone C(001) slabs along with the corresponding vibrational DOS plots shown below them. Gaussian broadening of 5 cm^{-1} is applied for both plots.

and 401 cm^{-1} are also identified as stretching modes of C-O-C, but they are hardly distinguishable in experimental studies. Simultaneously, the carbon atoms within the slab also vibrate at these two frequencies.

The infrared spectra of the ketone C slab in Fig. 8.2b exhibits a clear presence of the C=O stretching mode at 1853 cm^{-1}, slightly higher than the C=O stretching region (1600-1800 cm^{-1}) identified in the above reference [210]. Consistency exists between the calculated vibrational frequencies of ketone and ether C slabs. Vibrational modes of C appear in both spectra with frequencies at approximately 1220/1214 cm^{-1}, 1179/1143 cm^{-1}, 1067/1041 cm^{-1}, 773/768 cm^{-1}, and 571/540 cm^{-1}. These frequencies are in reasonable agreement with the calculated phonon frequencies at the Γ point for the phonon band structure of diamond nanowires obtained using DFT with the LDA functional [211].



(a) (b)

Figure 8.3: Two possible configurations for the H-terminated C(001) surface reported in Ref. 188. (a) Symmetric and (b) canted configurations. C and H atoms are shown in brown and pink, respectively.

8.5 Stabilities and EAs of hydrogen-terminated C slabs

In addition to the oxygen-terminated C slab, Ref. 188 reported hydrogen-terminated C with two distinct configurations. The symmetric configuration places two hydrogen atoms symmetrically above a carbon atom at the same height above the surface, as shown in Fig. 8.3a. In the canted configuration, adjacent hydrogen atoms have different heights as their distance from each other increases, as shown in Fig. 8.3b. The energy and EA of each configuration were calculated and presented in Table 8.2. The canted structure was found to be more stable by approximately 0.44 eV per surface carbon atom, consistent with the value of 0.42 eV reported in Ref. 188. Moreover, the calculated EAs of these two configurations show very good consistency with the EAs in the above reference.

This canted configuration is very interesting and might be applicable to the Si slab as an

Table 8.2: Calculated energies per surface C/Si atom and EAs of the symmetric and canted hydrogen-terminated C/Si(001) surfaces along with the calculated EAs in Refs. 188 and 187.

C surfaces	Energy/ C(Si) atom	EAs	EAs in Ref. 187, 188
Canted	0	-2.25	-2.36
Symmetric	0.44	-3.17	-3.19
Si surfaces			
Canted	0	3.99	-
Symmetric	0.13	3.98	4.22

alternative configuration to the symmetric hydrogen-terminated Si(001) slab used in this thesis. The symmetric configuration of the Si slab in Fig. 6.1e has been widely used in many studies [104, 187, 212]. The canted Si(001) slab has not been reported in the scope of my knowledge. An interesting thing to notice is that the symmetric Si slab maintains its original form after relaxation as an isolated slab, while it transforms to the canted configuration in the Si:TiO_2 interface (Model 1–4) after optimization. To obtain an independent canted Si slab, hydrogen atoms were intentionally placed at different heights, and the structure was relaxed. The relative surface energies and EAs were calculated for both configurations, provided in Table 8.2. The canted Si slab was found to be relatively stable with a 0.13 eV lower in energy per surface Si atom compared to the symmetric configuration. As for EA, the calculated difference between these two configurations is within 0.015 eV. Therefore, changing the symmetric hydrogen-terminated Si(001) slab configuration to the canted structure has a negligible effect on the calculated band offsets in this case.

8.6 Conclusion

The initial focus of this chapter is on the reconstructed 2×2 C(001) slab. The motivation for this study comes from the fact that the reconstructed 2×2 Si(001) slab is relatively more stable than the ether and ketone configurations. Therefore, it is expected that the 2×2 reconstructed C(001) slab will exhibit lower energy. However, the calculations showed that this idea is not feasible as the oxygen atoms in the 2×2 reconstructed C(001) slab tend to form an ether structure during relaxation. The relaxed ether and ketone slabs were used to determine the EAs, and the results were consistent with those previously reported values in Ref. 188. Furthermore, the calculated infrared spectra showed that the ketone and ether C(001) slabs exhibit C=O and C-O-C stretching modes, respectively. The calculated frequencies were in good agreement with the phonon frequencies of diamond nanowires obtained theoretically [211].

A final interesting point of this chapter is the investigation of the symmetric and canted hydrogen-terminated C and Si slabs. The calculated stability and EAs for the C slabs aligned with those reported in Ref. 188. Furthermore, calculations were then performed on the symmetric and canted Si(001) slab, with results indicating that the canted Si slab is a more stable configuration. Notably, switching between symmetric and canted configurations of the Si slab had a negligible effect on the calculated band offsets.

Chapter 9

Conclusion

9.1 General overview

The primary objective of this thesis was to use first-principles calculations to investigate the impact of structural features on the band offsets of the Si:TiO_2 interface, which is relevant to the development of TMO-passivated solar cells (Chapter 6). Understanding the sensitivity of band alignments will help experimentalists to understand the underlying correlation between the electronic properties and the structural properties of the Si:TiO_2 interface. Experimentalists can use this correlation to interpret the performance of Si:TiO_2-based solar cells produced using different fabrication techniques and potentially achieve improvements in solar cell performance by considering this sensitivity. Furthermore, the impacts of different levels of theory on calculating the band alignments of the Si:TiO_2 interface were investigated, aiming to propose a more computationally efficient method for additional theoretical research on the Si:TiO_2 interface. Prior to this investigation, the recently developed meta-GGA rSCAN functional had drawn attention. The performance of rSCAN compared to PBE and the GW approximation was investigated (Chapter 5). This evaluation of rSCAN will serve as a benchmark study to help researchers determine the suitability of using rSCAN in their calculations. Finally, the interfacial properties of the Si:TiO_2 interface models proposed in Chapter 6 were explored through infrared calculations in Chapter 7, which can serve as a reference point for further experimental studies on this interface. Relevant calculations focusing on the stabilities, structural properties, and EAs of the C and Si slabs with hydrogen and oxygen termination were presented in Chapter 8.

In Chapter 5, the calculated IPs and band gaps of a test set of semiconductors using rSCAN are in better agreement with experimental data compared to the calculated PBE values, which is con-

sistent with the recent examination of r^{2}SCAN functional [163] for calculating band alignments. Therefore, it is reasonable to believe that the accuracy in calculating band offsets using rSCAN is indeed improved compared to the PBE functional. However, the rSCAN results are still not as precise as the reported GW approximation results, particularly for materials with higher IPs. Higher levels of theory or methods are still required for more precise accuracy.

In Chapter 6, the band offsets of the Si:TiO_2 interface were calculated using two well-established methods: vacuum-level alignments, which aligns the energy levels of separate materials to a common vacuum level, and heterointerface alignments, which considers the potential variation across the heterointerface model. The results obtained through the vacuum-level alignment method show a significant decrease of 2.1 eV when oxygens terminate the dangling bonds on the silicon surface. However, this oxygen effect is not observed in heterointerface alignments, where the Si slab is also passivated with oxygens but with a TiO_2 slab placed above. Other than the oxygen-terminated Si slab, the calculated band offsets using the heterointerface alignment method agree well with the vacuum-level alignment method. A considerable shift of 0.4 eV is observed depending on whether the Si surface is in contact with the anatase (101) or (001) surfaces. Nevertheless, the band offsets are less sensitive to the degree of disorder at the interface when comparing highly crystalline Model 1 and amorphous Model 3. The exchange-correlation effects were examined using the GGA, meta-GGA, and GGA+U level of theory, as well as the band edge correction from hybrid functionals and the GW approximation [190–192, 194, 195]. The VBO is found to be mostly independent of the level of theory used but increased with the band edge corrections from hybrid functionals. In contrast, the CBO is much more sensitive, particularly to the U value. Applying post-processing GW correction brings the band offsets to the closest value to experimental results [35, 80, 98–101]. The small positive CBO obtained using the GW approximation indicates that the conduction band edges of Si and TiO_2 are in similar positions. This similarity suggests that small changes in the relative band positions can either enable or prevent electron transport across the interface. Therefore, it is likely that the preparation conditions will significantly impact electron transport across the Si:TiO_2 interface due to the induced changes in the CBO.

Chapter 7 focuses on investigating the structural properties of two proposed Si:TiO_2 interface models with relatively low surface energies using infrared calculations. The calculations were first conducted on the isolated Si and TiO_2 slabs, resulting in reasonably consistent vibrational modes compared to experimental measurements for similar systems [199–203, 205, 208, 209]. In terms of Si:TiO_2 interface models, the comparison between the calculation and experimental measurements

for related systems [204, 207] shows the existence of Si-O-Ti and Si-O-Si bonds in Model 1, with vibrational peaks detected in the 1000 cm^{-1} region. However, these corresponding vibrational frequencies are not present in the calculated infrared spectra of Model 2. Therefore, experimentalists can distinguish between Model 1 and Model 2 by examining the absorption modes in the 1000 cm^{-1} region, which will enable them to determine the similarity of their Si:TiO_2 interface to either model.

Chapter 8 focuses on investigating the stabilities, structural properties, and EAs of the C and Si slabs with oxygen and hydrogen termination. In contrast to the 2×2 reconstructed Si slab, the 2×2 reconstructed C slab is not stable and eventually transforms to an ether configuration after relaxation. The formation of C-O-C and C=O bonds in the ether and ketone configurations are observed in calculated infrared spectra, respectively. The calculated surface energies and EAs of the oxygen and hydrogen-terminated C slabs are in good agreement with the results reported in Ref. 188. The canted hydrogen-terminated Si slab is calculated to be a stable structure by 0.13 eV compared to the symmetric configuration, but it has a negligible impact on band offsets.

9.2 Future work

In this thesis, it has been demonstrated that although rSCAN provides band offsets that are closer than PBE to experiment and to higher-level calculations, it is still not accurate enough, particularly for CBOs. Hence, it is crucial to obtain the best possible description of CBOs. The GW corrected band edges applied to PBE yield comparable band offsets. Therefore, it would be worthwhile to use rSCAN as the starting point for the GW calculation and apply the corrections as shown in Fig. 6.10a to the rSCAN band edges.

In addition, rather than focusing on the crystalline Si:TiO_2 interface (Model 1 and Model 2), Model 3 with disordered interfacial bonding might be feasible to use as an amorphous interface, but more work is required in order to confirm this. Furthermore, while it is widely accepted that the Si(001) surface is the most stable at high temperatures, theoretical studies have revealed that Si(113) remains stable at both high and low temperatures despite its high index [166]. Both experimental and theoretical studies have confirmed that Si(111) is the most stable surface at low temperatures [166, 213]. It would be interesting to investigate how the band alignments are impacted by these Si surfaces. Alternatively, the slightly O-rich interfaces have been studied in this thesis. O-deficient interfaces acting as hole-selective contacts are not considered [86]. Therefore,

creating and analyzing O-deficient Si:TiO_2 interface models will be helpful in understanding the versatility of TiO_2 passivating layer, which can serve as both electron-selective and hole-selective contacts. Furthermore, first-principles calculations could be conducted on other electron-selective TMOs, such as ZnO_x and TaO_x, to determine whether they can be modified to become hole-selective through the creation of O-deficient interfaces.

Again, this thesis has only examined a limited number of Si:TiO_2 interface models. As computational power continues to advance, it would be beneficial to construct a large number of more complex Si:TiO_2 interface models with diverse structural characteristics. Such a model may correspond to a more realistic representation of the Si:TiO_2 interface observed in experiments.

Finally, the infrared spectra obtained from this study can be used as a valuable reference for future experimental investigations on the Si:TiO_2 interface. Since there are no experimental infrared measurements available for the Si:TiO_2 interface at this moment, an important future direction would be to experimentally measure the infrared spectra of this interface and compare them to the calculated spectra presented in this thesis in order to assign observed features to particular structures and then determine which interface model is more likely to be observed experimentally. In addition to infrared spectra, Raman spectra can also be calculated which serve as a valuable complement to infrared spectra in verifying the identified structural features and detecting infrared inactive vibrations. In this way, experimental and computational research can be used together to understand more about this important interface.

Appendix A

Convergence tests

A.1 Introduction

The purpose of this appendix is to offer supplementary convergence tests to support the computational parameters used in this thesis. While certain convergence tests regarding cutoff energy and k-point sampling are already outlined in the main thesis, this appendix will delve deeper into the specifics of the "fine grid scale" parameter, k-point sampling for bulk TiO_2 in the z-axis, as well as Si and TiO_2 slabs used in the thesis. Additionally, the convergence tests for Si, TiO_2, and C within the Quantum ESPRESSO package are also present.

A.2 "Fine grid scale"

The convergence test for the "fine grid scale" parameter was performed at different cutoff energy levels using the PBE and rSCAN functionals. Specifically, $\Delta\varepsilon_{\mathrm{VBM-Ref}}$ of Si and TiO_2 were calculated with cutoff energy of 300 eV, 500 eV, 700 eV, and 900 eV when using the PBE functional. For the rSCAN functional, cutoff energy of 400 eV, 600 eV, 800 eV, and 1000 eV were used. Fig. A.1 presents the calculated $\Delta\varepsilon_{\mathrm{VBM-Ref}}$ of bulk Si and TiO_2 with different cutoff energy levels as the "fine grid scale" increases from 1.75 to 5.

Based on Fig. A.1a and Fig. A.1c, very small fluctuations in $\Delta\varepsilon_{\mathrm{VBM-Ref}}$ of Si were observed across all cutoff energy levels when the "fine grid scale" parameter transitions from 1.75 to 2. As this parameter continues to increase, the variations reach a plateau. The magnitude of these variations in $\Delta\varepsilon_{\mathrm{VBM-Ref}}$ remains within 0.01 eV, indicating that changing the "fine grid scale" at the selected cutoff energy levels does not significantly influence the $\Delta\varepsilon_{\mathrm{VBM-Ref}}$ of Si.

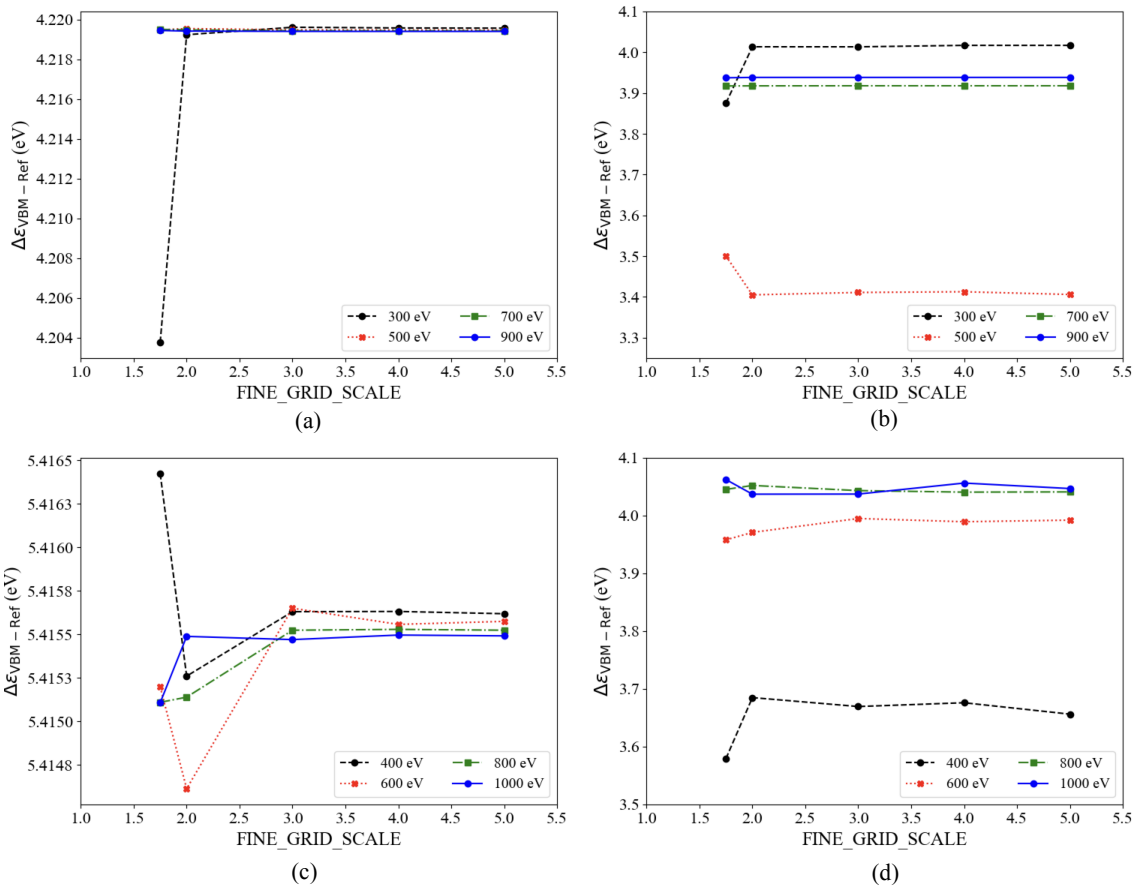


Figure A.1: Calculated $\Delta\varepsilon_{\mathrm{VBM-Ref}}$ of bulk Si and TiO_2 with different cutoff energy levels using PBE and rSCAN as the "fine grid scale" increases from 1.75 to 5. (a) and (c) represent the calculated $\Delta\varepsilon_{\mathrm{VBM-Ref}}$ of Si using PBE and rSCAN, respectively. (b) and (d) represent the calculated $\Delta\varepsilon_{\mathrm{VBM-Ref}}$ of TiO_2 using PBE and rSCAN, respectively. The calculations were conducted with a k-point grid of $8\times8\times8$.

In Fig. A.1b and Fig. A.1d, there are noticeable changes in the $\Delta\varepsilon_{\mathrm{VBM-Ref}}$ of TiO_2 at low cutoff energy as the "fine grid scale" parameter varied. However, the $\Delta\varepsilon_{\mathrm{VBM-Ref}}$ obtained with low cutoff energy and high "fine grid scale" is still not comparable to those obtained with high cutoff energy. When using higher cutoff energy, 700 and 900 eV for PBE or 800 and 1000 eV for rSCAN, the calculated $\Delta\varepsilon_{\mathrm{VBM-Ref}}$ of TiO_2 remain relatively constant as the "fine grid scale" parameter varied.

At the cutoff energy used in this thesis, which is 700 eV for PBE and 800 eV for rSCAN, there is no significant change in $\Delta\varepsilon_{\mathrm{VBM-Ref}}$ with an increase in the "fine grid scale" parameter. Therefore, the "fine grid scale" parameter is set to be 1.75, which is the default value in the CASTEP package, for calculations in this thesis.

A.3 k-point sampling for bulk TiO_2 in the z-axis

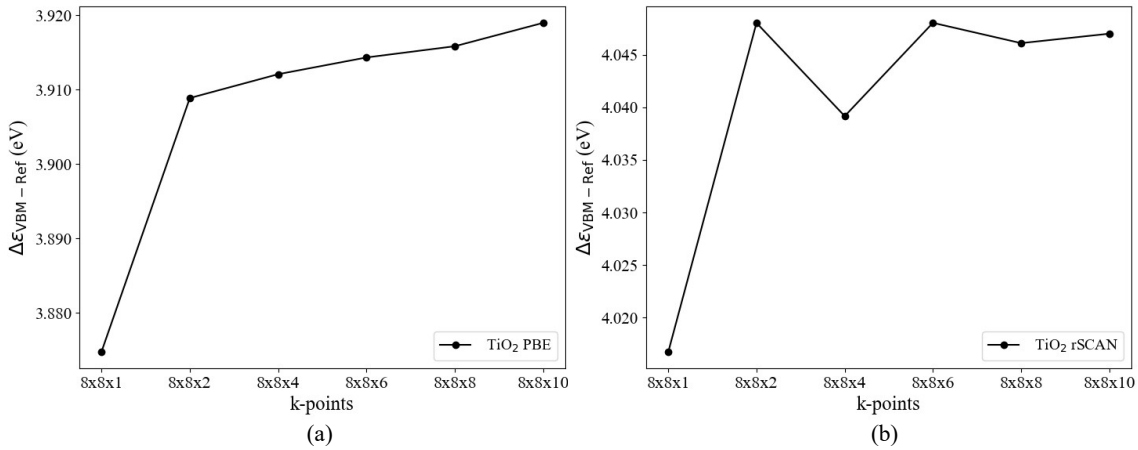


Figure A.2: Calculated $\Delta\varepsilon_{\mathrm{VBM-Ref}}$ of bulk TiO_2 using (a) PBE and (b) rSCAN as the k-point sampling in the z-axis increases from 2 to 10 while maintaining a fixed sampling of 8×8 for the remaining two axes. Cuttoff energy of 700 eV and 800 eV were applied when using PBE and rSCAN, respectively.

As previously mentioned, in bulk TiO_2 the lattice constant along the z-axis is greater than the lattice constants along the other two axes. Consequently, a smaller number of k-point could be used to sample the Brillouin zone in the z dimension. However, despite the significant difference in lattice constants between axes, a cubic grid of size 8×8×8 was used in the thesis. Based on the results shown in Figure A.2, the calculated $\Delta\varepsilon_{\mathrm{VBM-Ref}}$ remains relatively constant once the k-point sampling in the z dimension reaches 2 or higher. Therefore, the use of the 8×8×8 grid in this thesis ensures accurate results but requires higher computational costs. However, considering only 12 atoms are involved in the bulk anatase TiO_2 system, the amount of extra computational resource required to do 8×8×8 compared to 8×8×2 k-point sampling is not very large. Specifically, the PBE bulk calculation, using an 8×8×8 k-point sampling, takes 101 seconds to complete, while the calculation using an 8×8×2 k-point sampling finishes in 37 seconds. For future calculations, it is recommended to use an 8×8×2 k-point sampling for bulk TiO_2 in order to save computational resources.

A.4 k-point sampling for Si and TiO_2 slabs

k-point convergence test was performed for each Si and TiO_2 slab individually, where the energy difference between the macroscopic average of reference potential in the vacuum region and the bulk-like region of a slab model, $\Delta\varepsilon_{\mathrm{Vac-Ref}}$, is calculated as the k-point sampling increases from

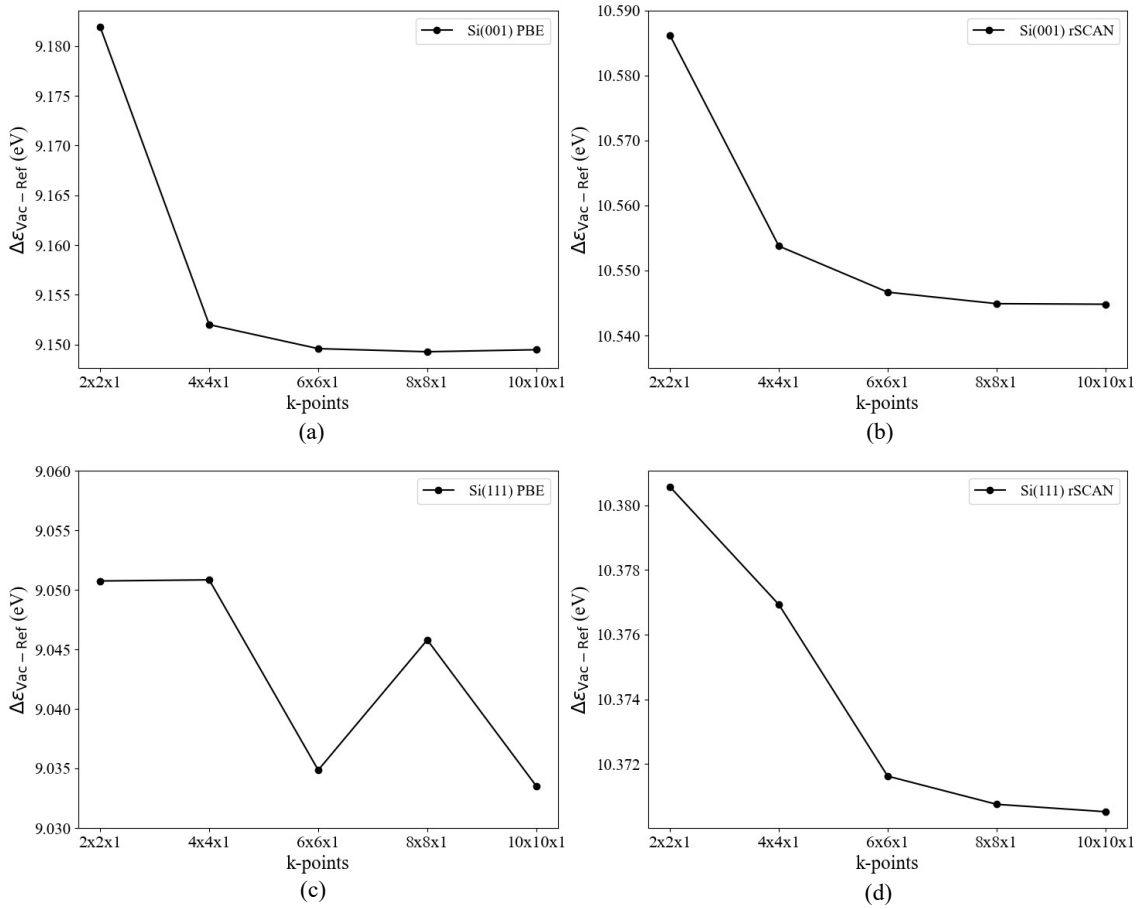


Figure A.3: Calculated $\Delta\varepsilon_{\mathrm{Vac-Ref}}$ of reconstructed Si(001) and (111) surfaces using PBE and rSCAN as the k-point grid increases from 2×2×1 to 10×10×1. (a) and (b) are the calculated $\Delta\varepsilon_{\mathrm{Vac-Ref}}$ of Si(001) using PBE and rSCAN, respectively. (c) and (d) are the calculated $\Delta\varepsilon_{\mathrm{Vac-Ref}}$ of Si(111) using PBE and rSCAN, respectively.

2×2×1 to 10×10×1. The calculations were performed using PBE and rSCAN with 700 eV and 800 eV, respectively. Fig. A.3, Fig. A.4, and Fig. A.5 present the calculated $\Delta\varepsilon_{\mathrm{Vac-Ref}}$ of each Si and TiO_2 slabs involved in this thesis with respect to different k-point sampling. Based on all these figures, it is obvious that the calculated $\Delta\varepsilon_{\mathrm{Vac-Ref}}$ exhibit a nearly constant trend as the k-point sampling reaches 6×6×1 or higher. This observation strongly suggests that using a 6×6×1 k-point sampling is sufficient to obtain accurate results for the Si and TiO_2 slabs used in this thesis.

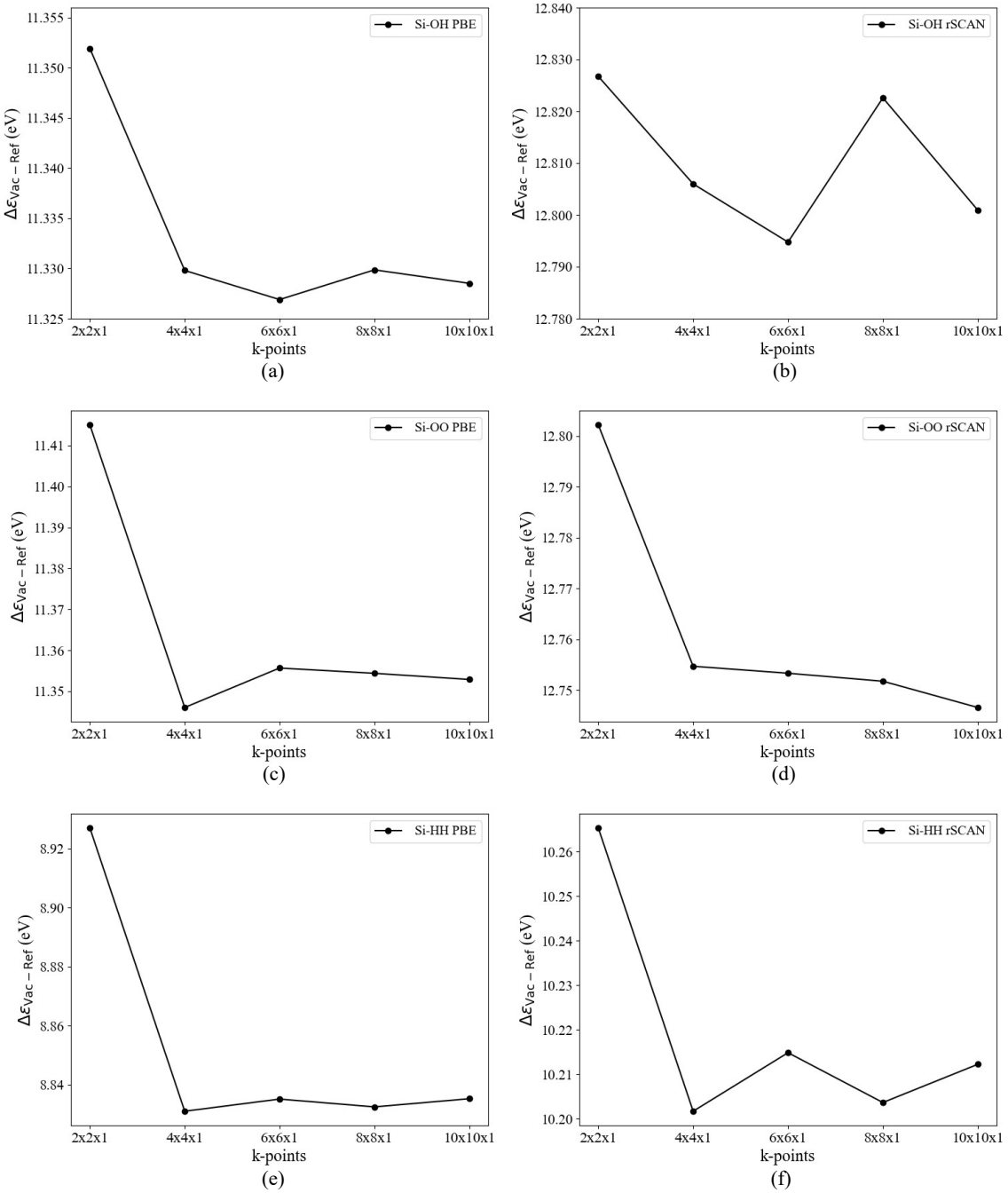


Figure A.4: Calculated $\Delta\varepsilon_{\mathrm{Vac-Ref}}$ of Si-OH, Si-OO, and Si-HH surfaces using PBE and rSCAN as the k-point sampling increases from $2\times2\times1$ to $10\times10\times1$. (a) and (b) are the calculated $\Delta\varepsilon_{\mathrm{Vac-Ref}}$ of Si-OH using PBE and rSCAN, respectively. (c) and (d) are the calculated $\Delta\varepsilon_{\mathrm{Vac-Ref}}$ of Si-OO using PBE and rSCAN, respectively. (e) and (f) are the calculated $\Delta\varepsilon_{\mathrm{Vac-Ref}}$ of Si-HH using PBE and rSCAN, respectively.

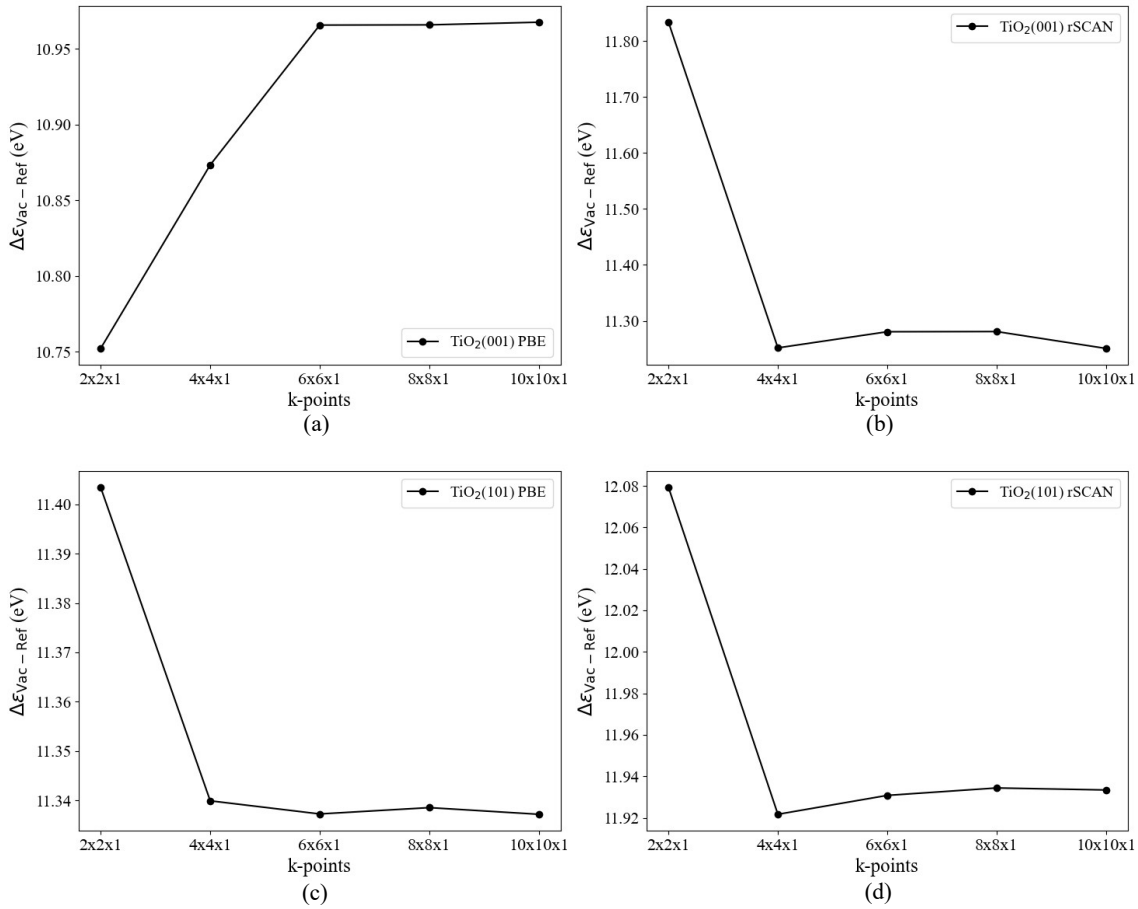


Figure A.5: Calculated $\Delta\varepsilon_{\mathrm{Vac-Ref}}$ of TiO_2(001) and (101) surfaces using PBE and rSCAN as the k-point sampling increases from $2\times2\times1$ to $10\times10\times1$. (a) and (b) are the calculated $\Delta\varepsilon_{\mathrm{Vac-Ref}}$ of TiO_2(001) using PBE and rSCAN, respectively. (c) and (d) are the calculated $\Delta\varepsilon_{\mathrm{Vac-Ref}}$ of TiO_2(101) using PBE and rSCAN, respectively.

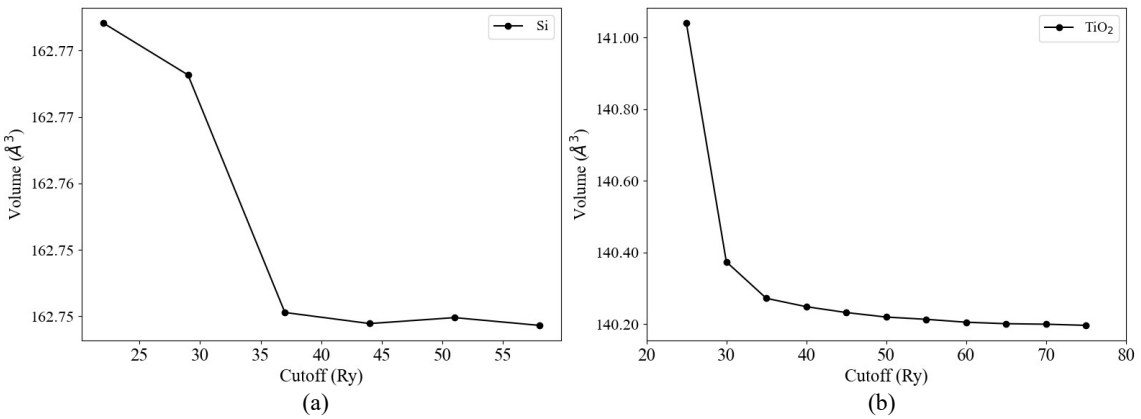


Figure A.6: Calculated volume of bulk (a) Si and (b) TiO_2 using the PBE functional as the cutoff energy increases from 22 Ry to 58 Ry and 25 Ry to 75 Ry, respectively. A k-point grid of 8×8×8 was used in the calculation.

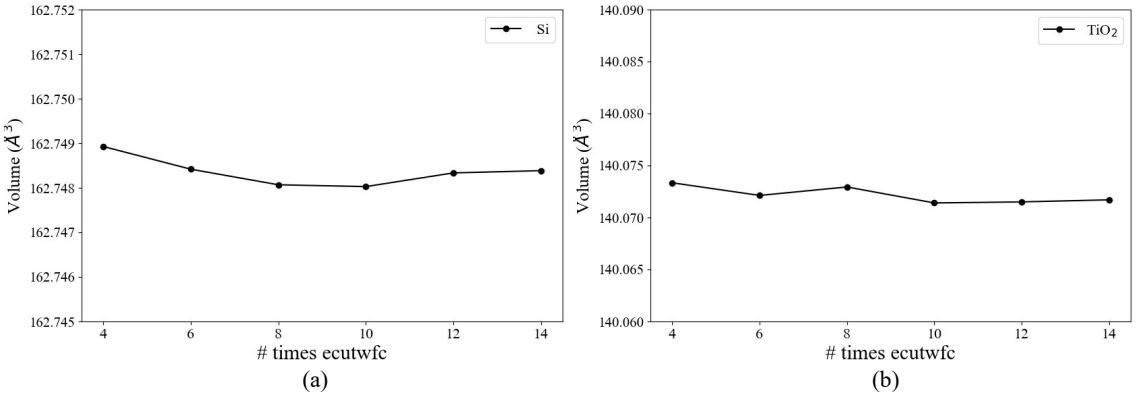


Figure A.7: Calculated volume of bulk (a) Si and (b) TiO_2 using the PBE functional as the cutoff energy for charge density increases from 4 times ecutwfc to 14 times ecutwfc. The ecutwfc represents the cutoff energy for wavefunction, which is 65 Ry in this case. A k-point grid of 8×8×8 was used in the calculation.

A.5 Convergence tests for Si and TiO_2 within the Quantum ESPRESSO package

Instead of calculating band alignments within the CASTEP package, calculations performed within the Quantum ESPRESSO package are focused on obtaining the infrared spectra, which require a fully optimized structure for accurate results. Therefore, convergence tests were conducted by calculating the volume of bulk Si and TiO_2 with different cutoff energies and k-point sampling. The cutoff energy for charge density is set to be 10 times the cutoff energy for wavefunction. Figure A.6 presents the calculated volume of bulk Si and TiO_2 using the PBE functional with various cutoff energy.

The volume of bulk Si in Fig. A.6a indicates a small variation as the cutoff energy increases from 22 Ry to 36 Ry. Upon reaching 36 Ry and beyond, the volume remains nearly constant.

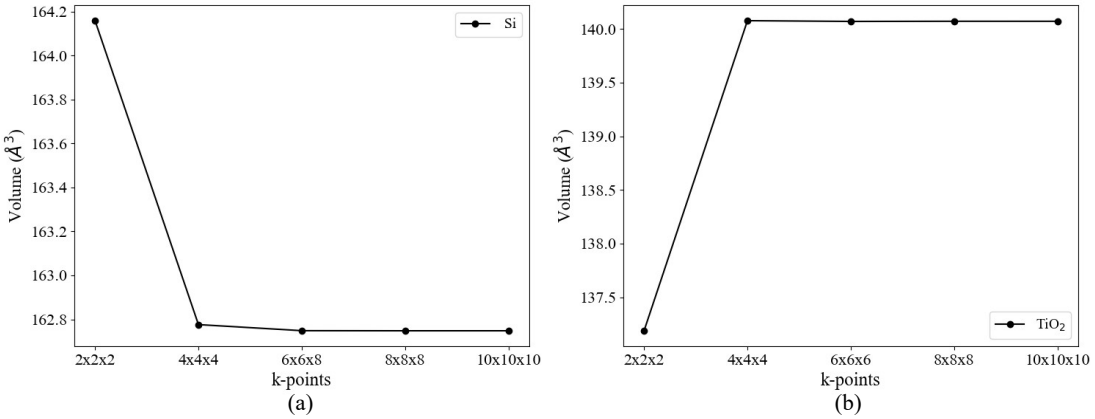


Figure A.8: Calculated volume of bulk (a) Si and (b) TiO_2 using the PBE functional as the k-point sampling increases from $2\times2\times2$ to $10\times10\times10$. 65 Ry cutoff energy was used in the calculation.

However, for TiO_2, there is a decrease in volume as the cutoff energy changes from 25 Ry to 45 Ry. As the cutoff energy increases further, the variation in volume continues to drop until it reaches 60 Ry. Therefore, cutoff energy of 65 Ry is considered reliable for bulk TiO_2. Since heterointerface calculation is later performed, the cutoff energy for Si is also chosen to be 65 Ry, matching that of TiO_2.

To determine the appropriate cutoff energy for charge density, volume of bulk Si and TiO_2 was calculated while keeping the cutoff energy for wavefunction fixed at 65 Ry. The cutoff energy for charge density was varied as 4, 6, 8, 10, 12, and 14 times the cutoff energy for wavefunction. Fig. A.7 presents the calculated volume of bulk Si and TiO_2 as the cutoff energy for charge density varied. The results indicate that the calculated volumes of Si and TiO_2 exhibit negligible changes across all the cutoff energy for charge density considered. In this thesis, the cutoff energy for charge density is selected to be 10 times the cutoff energy for wavefunction, as it has been demonstrated to be reliable through the convergence test shown in Figure A.7.

After selecting the cutoff energy, a convergence test was conducted for the k-point sampling. Figure A.8 shows the calculated volume of bulk Si and TiO_2 using the PBE functional with different k-point sampling. The results indicate that the calculated volumes of Si and TiO_2 remain almost constant when using a k-point sampling of $4\times4\times4$ or higher. Considering the slab models used in Chapter 7, which share the same lattice parameters as bulk Si and TiO_2, a k-point sampling of $6\times6\times1$ was chosen for the slab calculations. This $6\times6\times1$ k-point sampling is believed to be reliable enough to ensure the accuracy and convergence of the calculations for the slab models.

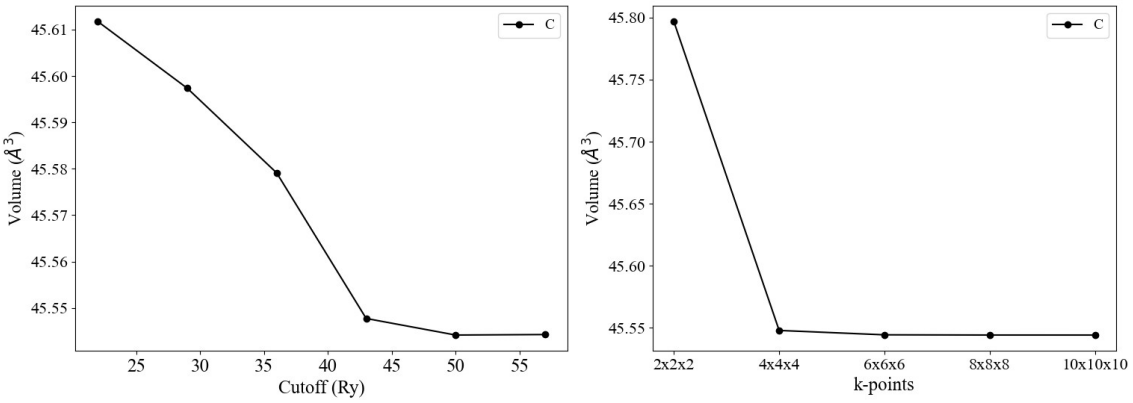


Figure A.9: Calculated volume of bulk C using the LDA functional as the (a) cutoff energy and (b) k-point sampling varied. The cutoff energy for charge density is set to be 10 times the cutoff energy for wavefunction.

A.6 Convergence tests for C cell

Since Chapter 8 involves the use of the Quantum ESPRESSO package for calculating infrared spectra and the CASTEP package for determining the EA, convergence tests for the C cell were performed separately for each package. For the Quantum ESPRESSO package, convergence tests were performed by varying the cutoff energy and k-point sampling in relation to the volume of the bulk C cell. The calculated results for cutoff energy and k-point sampling are present in Fig. A.9, which clearly demonstrate that the volume of bulk C is converged when cutoff energy reaches 50 Ry and k-point sampling reaches $4\times4\times4$. When calculating the infrared spectra of C slabs in Chapter 8, cutoff energy of 55 Ry and $8\times8\times1$ k-point grid were chosen for even better convergence.

The EA of C slabs was determined using LDA functional within the CASTEP package. Therefore, convergence tests were performed by calculating EA and $\Delta\varepsilon_{\mathrm{VBM-Ref}}$ with respect to different cutoff energies and k-point sampling, respectively. The EA was calculated for oxygen-terminated C slab with ketone configuration. The $\Delta\varepsilon_{\mathrm{VBM-Ref}}$ was extracted from bulk C calculation, which is the essential quantity needed to determine the EA. The calculated results for cutoff energy and k-point sampling are illustrated in Fig. A.10.

The calculated EA of oxygen-terminated C slab in Fig. A.10a reaches a plateau value when the cutoff energy reaches 600 eV. Therefore, 700 eV cutoff energy was chosen for C slab calculation. In terms of k-point sampling in Fig. A.10b, the $\Delta\varepsilon_{\mathrm{VBM-Ref}}$ of bulk C remains constant when using a $6\times6\times6$ k-point grid and higher. As a result, the k-point sampling for C is set to be $8\times8\times8$. An $8\times8\times1$ k-point grid was used for C slab calculation since the lattice parameter of

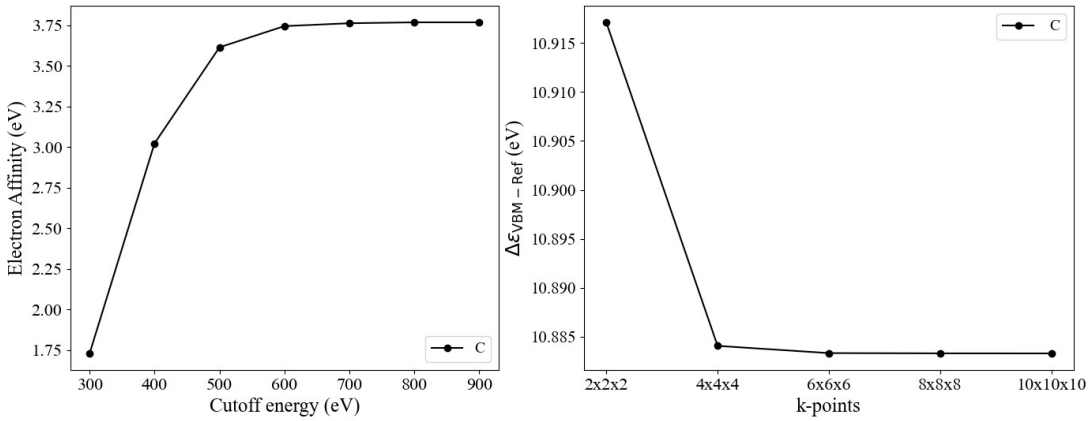


Figure A.10: (a) Calculated EA of oxygen-terminated C slab and (b) $\Delta\varepsilon_{\mathrm{VBM-Ref}}$ of bulk C using the LDA functional as the cutoff energy and k-point sampling varied, respectively.

C slab is consistent with bulk C cell. However, a $4\times4\times1$ k-point grid was selected for the 2×1 reconstructed C slab because it is a 2×2 surface cell, which contains twice the lattice constant compared to the rest of the slabs.

Appendix B

Band structure and DOS of the Si:TiO_2 interface

B.1 Introduction

The aim of this appendix is to provide further information to support the conclusion proposed in Section 6.4.3 in which the Si:TiO_2 interface shows metallic properties after aligning the energy level of Si and TiO_2 obtained using PBE and rSCAN without any correction applied. The metallic behavior rises from the well-known "band gap problem", where the band gap of Si and TiO_2 are underestimated, resulting in the conduction band of TiO_2 erroneously placed lower in energy than the valence band of Si. To further justify this finding, the band structure and DOS of the Si:TiO_2 interface (Model 1 and Model 2) were calculated using the PBE and rSCAN functionals.

B.2 Model 1

The computational detail for calculating the band structure and DOS followed the same computational methodologies described in Section 5.3.2. For the self-consistent step to determine the density, a grid of $4\times4\times1$ k-point was used. Subsequently, a finer grid of $8\times8\times1$ k-point was employed to compute the eigenvalues required for the DOS calculation. The resulting band structure and DOS for Model 1, obtained using PBE and rSCAN, are presented in Figure B.1.

Based on Figure B.1a and Figure B.1c, it is evident that no band gap is observed in Model 1, indicating its metallic behavior. This conclusion is further supported by the DOS plot depicted in Figure B.1b and Figure B.1d, where the CBM of TiO_2 is located at a lower energy level compared

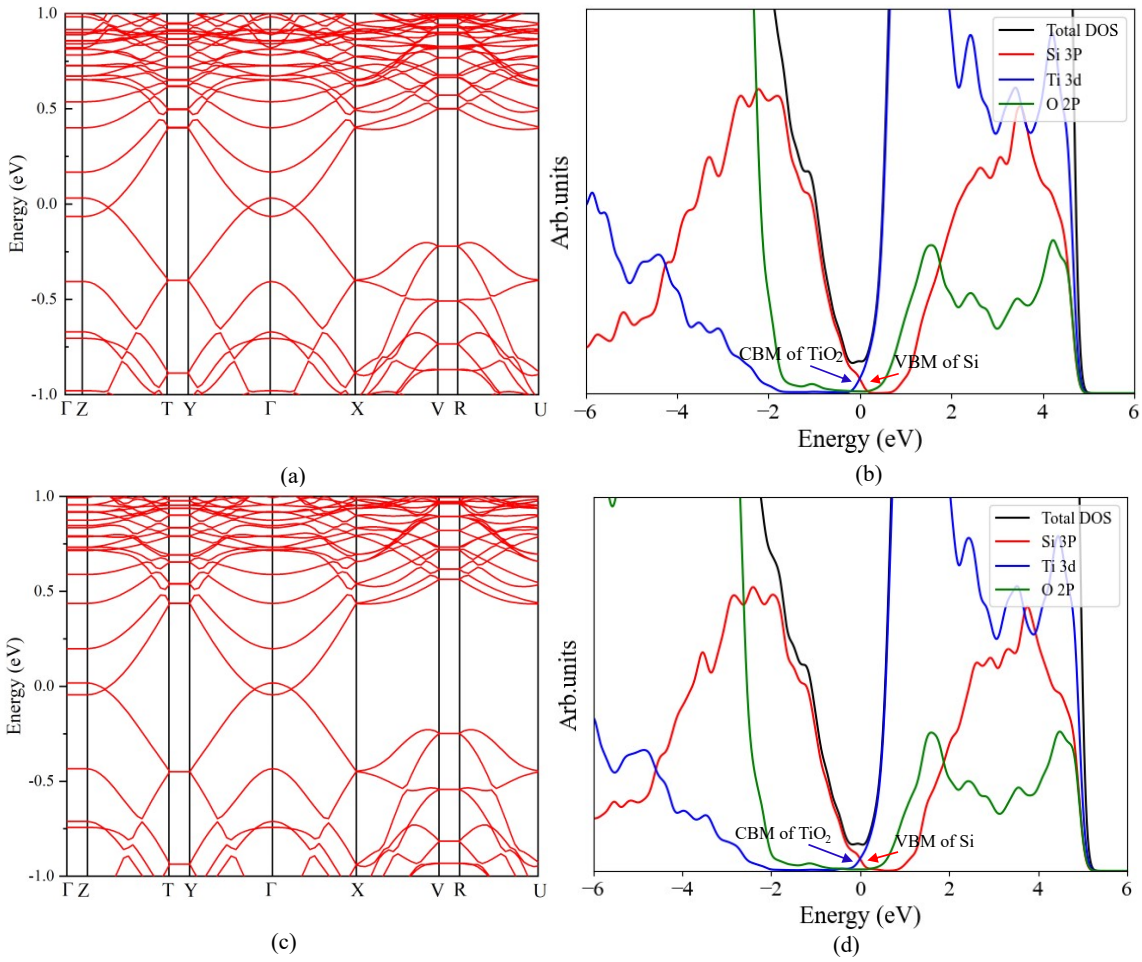


Figure B.1: Band structure and DOS of Model 1 Si:TiO_2 interface obtained using (a,b) PBE and (c,d) rSCAN. In units of the reciprocal lattice vectors, the k-point sampling are chosen as Γ = 0 0 0, Z = 0 0 $\frac{1}{2}$, T = 0 $\frac{1}{2}$ $\frac{1}{2}$, Y = 0 $\frac{1}{2}$ 0, X = $\frac{1}{2}$ 0 0, V = $\frac{1}{2}$ $\frac{1}{2}$ 0, R = $\frac{1}{2}$ $\frac{1}{2}$ $\frac{1}{2}$, U = $\frac{1}{2}$ 0 $\frac{1}{2}$. Gaussian broadening of 0.1 eV is applied for the DOS plot. The Fermi energy was set to be at zero energy.

to the VBM of Si. This observation aligns with the argument discussed in Section 6.4.3, stating that the metallic property is calculated in the Si:TiO_2 interface when using the PBE and rSCAN functionals without applying any band gap corrections.

B.3 Model 2

The band structure and DOS for Model 2 were calculated using the PBE and rSCAN functionals, following the same computational approach mentioned above. The corresponding results are displayed in Figure B.2. Upon analyzing the calculated band structure, it is observed that a small gap of 0.02 eV and 0.03 eV exists when using the PBE and rSCAN functionals, respectively. These gaps were caused by the coarse k-point sampling used when calculating the DOS. As more dense k-point sampling was used, the energy states in the band structure plots will smoothly connect and

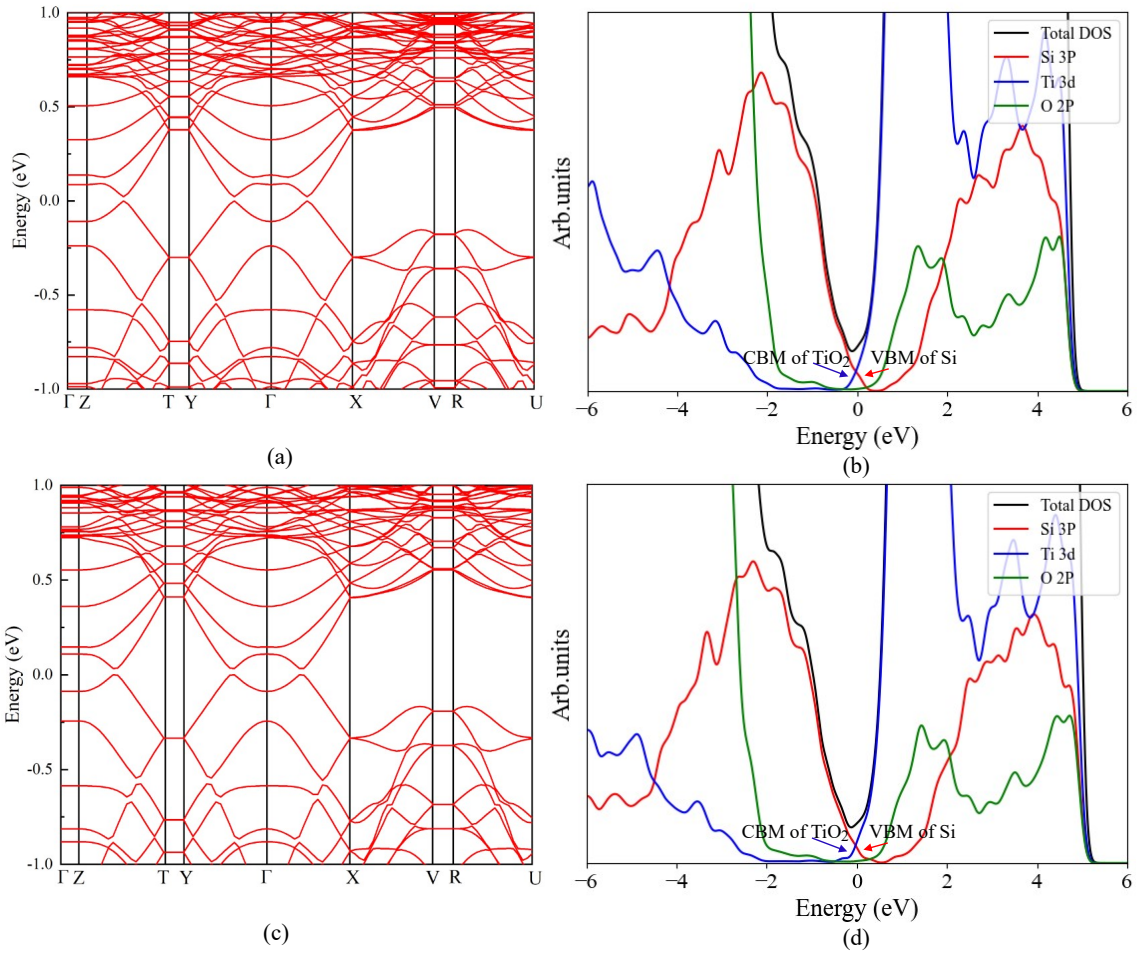


Figure B.2: Band structure and DOS of Model 2 Si:TiO_2 interface obtained using (a,b) PBE and (c,d) rSCAN. In units of the reciprocal lattice vectors, the k-point sampling are chosen as Γ = 0 0 0, Z = 0 0 $\frac{1}{2}$, T = 0 $\frac{1}{2}$ $\frac{1}{2}$, Y = 0 $\frac{1}{2}$ 0, X = $\frac{1}{2}$ 0 0, V = $\frac{1}{2}$ $\frac{1}{2}$ 0, R = $\frac{1}{2}$ $\frac{1}{2}$ $\frac{1}{2}$, U = $\frac{1}{2}$ 0 $\frac{1}{2}$. Gaussian broadening of 0.1 eV is applied for the DOS plot. The Fermi energy was set to be at zero energy.

eliminate the small gaps. Further clarification is derived from the calculated DOS plots for Model 2, where it is evident that the VBM of Si is positioned at a higher energy level than the CBM of TiO_2. This finding suggests that Model 2 also exhibits metallic behavior when using both the PBE and rSCAN functionals.

Bibliography

[1] J. Houghton, *Reports on Progress in Physics*, 2005, **68**, 1343.

[2] A. Olabi and M. A. Abdelkareem, *Renewable and Sustainable Energy Reviews*, 2022, **158**, 112111.

[3] G. Bo, P. Cheng, K. Dezhi, W. Xiping, L. Chaodong, G. Mingming, and N. Ghadimi, *Energy Sources, Part A: Recovery, Utilization, and Environmental Effects*, 2022, **44**, 7109–7131.

[4] A. Olabi, K. Obaideen, K. Elsaid, T. Wilberforce, E. T. Sayed, H. M. Maghrabie, and M. A. Abdelkareem, *Renewable and Sustainable Energy Reviews*, 2022, **153**, 111710.

[5] M. Mathew, *Progress in Nuclear Energy*, 2022, **143**, 104080.

[6] D. Scott, C. M. Hall, and S. Gössling, *Journal of Sustainable Tourism*, 2016, **24**, 933–948.

[7] X. Zhao, X. Ma, B. Chen, Y. Shang, and M. Song, *Resources, Conservation and Recycling*, 2022, **176**, 105959.

[8] M. Lenzen, *Energy Conversion and Management*, 2008, **49**, 2178–2199.

[9] S. Mughal, Y. R. Sood, and R. Jarial, *International Journal of Scientific Research in Computer Science, Engineering and Information Technology*, 2018, **4**, 227–235.

[10] T. D. Lee and A. U. Ebong, *Renewable and Sustainable Energy Reviews*, 2017, **70**, 1286–1297.

[11] H. Hoppe and N. S. Sariciftci, *Journal of Materials Research*, 2004, **19**, 1924–1945.

[12] N. J. Jeon, J. H. Noh, Y. C. Kim, W. S. Yang, S. Ryu, and S. I. Seok, *Nature Materials*, 2014, **13**, 897–903.

[13] M. A. Green, *Joule*, 2019, **3**, 631–633.

[14] T. G. Allen, J. Bullock, X. Yang, A. Javey, and S. De Wolf, *Nature Energy*, 2019, **4**, 914–928.

[15] K. Wojciechowski and D. Forgács, *ACS Energy Letters*, 2022, **7**, 3729–3733.

[16] J. Pastuszak and P. Wegierek, *Materials*, 2022, **15**, 5542.

[17] T. Saga, *Npg Asia Materials*, 2010, **2**, 96–102.

[18] D. E. Carlson and C. R. Wronski, *Applied Physics Letters*, 1976, **28**, 671–673.

[19] V. Fthenakis, *Renewable and Sustainable Energy Reviews*, 2009, **13**, 2746–2750.

[20] M. V. Dambhare, B. Butey, and S. Moharil, *Journal of Physics: Conference Series*, 2021, **1913**, 012053.

[21] B. O'regan and M. Grätzel, *Nature*, 1991, **353**, 737–740.

[22] M. A. Green, A. Ho-Baillie, and H. J. Snaith, *Nature Photonics*, 2014, **8**, 506–514.

[23] A. Chirilă, P. Reinhard, F. Pianezzi, P. Bloesch, A. R. Uhl, C. Fella, L. Kranz, D. Keller, C. Gretener, H. Hagendorfer, et al., *Nature Materials*, 2013, **12**, 1107–1111.

[24] G. Li, R. Zhu, and Y. Yang, *Nature Photonics*, 2012, **6**, 153–161.

[25] S. Das, D. Pandey, J. Thomas, and T. Roy, *Advanced Materials*, 2019, **31**, 1802722.

[26] M. A. Iqbal, M. Malik, W. Shahid, S. Z. U. Din, N. Anwar, M. Ikram, and F. Idrees, *Thin Films Photovoltaics*, 2022.

[27] S.-H. Bae, H. Zhao, Y.-T. Hsieh, L. Zuo, N. De Marco, Y. S. Rim, G. Li, and Y. Yang, *Chem*, 2016, **1**, 197–219.

[28] A. Uruena, J. Horzel, S. Singh, I. Kuzma-Filipek, E. Cornagliotti, B. John, R. Mertens, and J. Poortmans, *Energy Procedia*, 2012, **27**, 561–566.

[29] J. Melskens, B. W. van de Loo, B. Macco, L. E. Black, S. Smit, and W. Kessels, *IEEE Journal of Photovoltaics*, 2018, **8**, 373–388.

[30] A. Richter, S. W. Glunz, F. Werner, J. Schmidt, and A. Cuevas, *Physical Review B*, 2012, **86**, 165202.

[31] M. Wolf, *Solar cells*, 1986, **17**, 53–63.

[32] F. Meyer, A. Ingenito, J. J. D. Leon, X. Niquille, C. Allebé, S. Nicolay, F.-J. Haug, and C. Ballif, *Solar Energy Materials and Solar Cells*, 2022, **235**, 111455.

[33] S. Acharyya, S. Sadhukhan, T. Panda, D. K. Ghosh, N. C. Mandal, A. Nandi, S. Bose, G. Das, S. Maity, P. Chaudhuri, et al., *Surfaces and Interfaces*, 2022, **28**, 101687.

[34] L. Zhang and M. Jaroniec, *Applied Surface Science*, 2018, **430**, 2–17.

[35] J. Robertson, *Journal of Vacuum Science & Technology A: Vacuum, Surfaces, and Films*, 2013, **31**, 050821.

[36] A. Klein, *Thin Solid Films*, 2012, **520**, 3721–3728.

[37] Y. Mi and Y. Weng, *Scientific Reports*, 2015, **5**, 1–10.

[38] Y. Hinuma, A. Grüneis, G. Kresse, and F. Oba, *Physical Review B*, 2014, **90**, 155405.

[39] I. Vurgaftman, J. á. Meyer, and L. á. Ram-Mohan, *Journal of Applied Physics*, 2001, **89**, 5815–5875.

[40] W. Hu and J. Yang, *Journal of Materials Chemistry C*, 2017, **5**, 12289–12297.

[41] A. P. Bartók and J. R. Yates, *The Journal of Chemical Physics*, 2019, **150**, 161101.

[42] R. T. Tung, *Applied Physics Reviews*, 2014, **1**, 011304.

[43] J. Tersoff, *Physical Review B*, 1985, **32**, 6968.

[44] B. Min, M. Müller, H. Wagner, G. Fischer, R. Brendel, P. P. Altermatt, and H. Neuhaus, *IEEE Journal of Photovoltaics*, 2017, **7**, 1541–1550.

[45] S. Olibet, E. Vallat-Sauvain, and C. Ballif, *Physical Review B*, 2007, **76**, 035326.

[46] H. Lu, Y. Guo, H. Li, and J. Robertson, *Applied Physics Letters*, 2019, **114**, 222106.

[47] A. J. Bard, A. B. Bocarsly, F. R. F. Fan, E. G. Walton, and M. S. Wrighton, *Journal of the American Chemical Society*, 1980, **102**, 3671–3677.

[48] D. Yan and A. Cuevas, *Journal of Applied Physics*, 2013, **114**, 044508.

[49] P. Peacock, K. Xiong, K. Tse, and J. Robertson, *Physical Review B*, 2006, **73**, 075328.

[50] M. Hermle, F. Feldmann, M. Bivour, J. C. Goldschmidt, and S. W. Glunz, *Applied Physics Reviews*, 2020, **7**, 021305.

[51] T. Nishimura, K. Kita, and A. Toriumi, *Applied Physics Express*, 2008, **1**, 051406.

[52] S. W. Glunz, *Advances in OptoElectronics*, 2007, **2007**.

[53] M. A. Green and R. Godfrey, *Applied Physics Letters*, 1976, **29**, 610–612.

[54] M. Green and R. Godfrey, *Japanese Journal of Applied Physics*, 1978, **17**, 295.

[55] R. Hezel, *Progress in Photovoltaics: Research and Applications*, 1997, **5**, 109–120.

[56] A. Blakers and M. Green, *Applied Physics Letters*, 1981, **39**, 483–485.

[57] J. Pankove and M. Tarng, *Applied Physics Letters*, 1979, **34**, 156–157.

[58] D. Adachi, J. L. Hernández, and K. Yamamoto, *Applied Physics Letters*, 2015, **107**, 233506.

[59] Z. C. Holman, A. Descoeudres, L. Barraud, F. Z. Fernandez, J. P. Seif, S. De Wolf, and C. Ballif, *IEEE Journal of Photovoltaics*, 2012, **2**, 7–15.

[60] J. M. Gee In *Conference Record of the Twentieth IEEE Photovoltaic Specialists Conference*, Vol. 1, pp. 549–554, 1988.

[61] K. Masuko, M. Shigematsu, T. Hashiguchi, D. Fujishima, M. Kai, N. Yoshimura, T. Yamaguchi, Y. Ichihashi, T. Mishima, N. Matsubara, et al., *IEEE Journal of Photovoltaics*, 2014, **4**, 1433–1435.

[62] H.-Y. Tsai, S.-W. Wang, S.-Y. Wu, J.-R. Chen, E. Y. Ngai, and K. P.-P. Huang, *Journal of Loss Prevention in the Process Industries*, 2010, **23**, 170–177.

[63] X. Yang, Q. Bi, H. Ali, K. Davis, W. V. Schoenfeld, and K. Weber, *Advanced Materials*, 2016, **28**, 5891–5897.

[64] Y. Wang, S.-T. Zhang, L. Li, X. Yang, L. Lu, and D. Li, *EcoMat*, 2023, **5**, e12292.

[65] R. S. Bonilla, B. Hoex, P. Hamer, and P. R. Wilshaw, *Physica Status Solidi (A)*, 2017, **214**, 1700293.

[66] H. Peng and S. Lany, *Physical Review B*, 2012, **85**, 201202.

[67] D. O. Scanlon, G. W. Watson, D. Payne, G. Atkinson, R. Egdell, and D. Law, *The Journal of Physical Chemistry C*, 2010, **114**, 4636–4645.

[68] J. Cho, N. Nawal, A. Hadipour, M. R. Payo, A. van der Heide, H. S. Radhakrishnan, M. Debucquoy, I. Gordon, J. Szlufcik, and J. Poortmans, *Solar Energy Materials and Solar Cells*, 2019, **201**, 110074.

[69] V. E. Henrich and P. A. Cox, *The surface science of metal oxides*, Cambridge University Press, 1996.

[70] M. Bivour, B. Macco, J. Temmler, W. E. Kessels, and M. Hermle, *Energy Procedia*, 2016, **92**, 443–449.

[71] B. Han, M. Gao, Y. Wan, Y. Li, W. Song, and Z. Ma, *Materials Science in Semiconductor Processing*, 2018, **75**, 166–172.

[72] S. Smit, D. Garcia-Alonso, S. Bordihn, M. Hanssen, and W. Kessels, *Solar Energy Materials and Solar Cells*, 2014, **120**, 376–382.

[73] Y. Wan, J. Bullock, and A. Cuevas, *Solar Energy Materials and Solar Cells*, 2015, **142**, 42–46.

[74] J. Bullock, M. Hettick, J. Geissbühler, A. J. Ong, T. Allen, C. M. Sutter-Fella, T. Chen, H. Ota, E. W. Schaler, S. De Wolf, et al., *Nature Energy*, 2016, **1**, 1–7.

[75] M. Bivour, J. Temmler, H. Steinkemper, and M. Hermle, *Solar Energy Materials and Solar Cells*, 2015, **142**, 34–41.

[76] B. Richards, *Progress in Photovoltaics: Research and Applications*, 2004, **12**, 253–281.

[77] K. Kern and E. Tracy, *RCA Rev.;(United States)*, 1980, **41**.

[78] G. Sahasrabudhe, S. M. Rupich, J. Jhaveri, A. H. Berg, K. A. Nagamatsu, G. Man, Y. J. Chabal, A. Kahn, S. Wagner, J. C. Sturm, and J. Schwartz, *Journal of the American Chemical Society*, 2015, **137**, 14842–14845.

[79] K. A. Nagamatsu, S. Avasthi, G. Sahasrabudhe, G. Man, J. Jhaveri, A. H. Berg, J. Schwartz, A. Kahn, S. Wagner, and J. C. Sturm, *Applied Physics Letters*, 2015, **106**, 123906.

[80] J. Bullock, Y. Wan, Z. Xu, S. Essig, M. Hettick, H. Wang, W. Ji, M. Boccard, A. Cuevas, C. Ballif, and A. Javey, *ACS Energy Letters*, 2018, **3**, 508–513.

[81] J. Bullock, Y. Wan, M. Hettick, X. Zhaoran, S. P. Phang, D. Yan, H. Wang, W. Ji, C. Samundsett, Z. Hameiri, et al., *Advanced Energy Materials*, 2019, **9**, 1803367.

[82] I.-S. Yu, I.-H. Chang, H.-E. Cheng, and Y.-S. Lin In *2014 IEEE 40th Photovoltaic Specialist Conference*, pp. 1271–1274, 2014.

[83] G. Sahasrabudhe, S. M. Rupich, J. Jhaveri, A. H. Berg, K. A. Nagamatsu, G. Man, Y. J. Chabal, A. Kahn, S. Wagner, J. C. Sturm, et al., *Journal of the American Chemical Society*, 2015, **137**, 14842–14845.

[84] B. Liao, B. Hoex, A. G. Aberle, D. Chi, and C. S. Bhatia, *Applied Physics Letters*, 2014, **104**, 253903.

[85] Z. Ling, J. He, X. He, M. Liao, P. Liu, Z. Yang, J. Ye, and P. Gao, *IEEE Journal of Photovoltaics*, 2017, **7**, 1551–1555.

[86] T. Matsui, M. Bivour, P. F. Ndione, R. S. Bonilla, and M. Hermle, *Solar Energy Materials and Solar Cells*, 2020, **209**, 110461.

[87] D. Reyes-Coronado, G. Rodríguez-Gattorno, M. Espinosa-Pesqueira, C. Cab, R. De Coss, and G. Oskam, *Nanotechnology*, 2008, **19**, 145605.

[88] L. E. Oi, M.-Y. Choo, H. V. Lee, H. C. Ong, S. B. Abd Hamid, and J. C. Juan, *Rsc Advances*, 2016, **6**, 108741–108754.

[89] K. Bourikas, C. Kordulis, and A. Lycourghiotis, *Chemical Reviews*, 2014, **114**, 9754–9823.

[90] M. Lazzeri, A. Vittadini, and A. Selloni, *Physical Review B*, 2001, **63**, 155409.

[91] M. Y. Manuputty, J. A. Dreyer, Y. Sheng, E. J. Bringley, M. L. Botero, J. Akroyd, and M. Kraft, *Chemical Science*, 2019, **10**, 1342–1350.

[92] D. A. Hanaor and C. C. Sorrell, *Journal of Materials Science*, 2011, **46**, 855–874.

[93] D. K. Pallotti, L. Passoni, P. Maddalena, F. Di Fonzo, and S. Lettieri, *The Journal of Physical Chemistry C*, 2017, **121**, 9011–9021.

[94] T. Luttrell, S. Halpegamage, J. Tao, A. Kramer, E. Sutter, and M. Batzill, *Scientific Reports*, 2014, **4**, 4043.

[95] J. Zhang, P. Zhou, J. Liu, and J. Yu, *Physical Chemistry Chemical Physics*, 2014, **16**, 20382–20386.

[96] D. Gebeyehu, C. Brabec, N. Sariciftci, D. Vangeneugden, R. Kiebooms, D. Vanderzande, F. Kienberger, and H. Schindler, *Synthetic Metals*, 2001, **125**, 279–287.

[97] Y. Chung, W. Lo, and G. Somorjai, *Surface Science*, 1977, **64**, 588–602.

[98] S. Avasthi, W. E. McClain, G. Man, A. Kahn, J. Schwartz, and J. C. Sturm, *Applied Physics Letters*, 2013, **102**, 203901.

[99] L. Chen, W. Tian, C. Sun, F. Cao, and L. Li, *ACS Applied Materials & Interfaces*, 2019, **11**, 3241–3250.

[100] X. Yang, P. Zheng, Q. Bi, and K. Weber, *Solar Energy Materials and Solar Cells*, 2016, **150**, 32–38.

[101] J. Robertson, *Journal of Vacuum Science & Technology B: Microelectronics and Nanometer Structures Processing, Measurement, and Phenomena*, 2000, **18**, 1785–1791.

[102] S. Kashiwaya, J. Morasch, V. Streibel, T. Toupance, W. Jaegermann, and A. Klein, *Surfaces*, 2018, **1**, 73–89.

[103] E. Schrödinger, *Annalen der Physik*, 1926, **385**, 437–490.

[104] F. Giustino, *Materials Modelling using Density Functional Theory: Properties and Predictions*, Oxford University Press, 2014.

[105] W. Kohn, *Reviews of Modern Physics*, 1999, **71**, 1253.

[106] M. Born and R. Oppenheimer, *Annalen der Physik*, 1927, **389**, 457–484.

[107] D. Sholl and J. Steckel, *Density Functional Theory: A Practical Introduction*, Wiley, 2011.

[108] D. R. Hartree, *Mathematical Proceedings of the Cambridge Philosophical Society*, 1928, **24**, 89–110.

[109] P. Hohenberg and W. Kohn, *Physical Review*, 1964, **136**, B864.

[110] W. Kohn and L. J. Sham, *Physical Review*, 1965, **140**, A1133.

[111] C. Kittel and P. McEuen, *Introduction to solid state physics*, John Wiley & Sons, 2018.

[112] S. J. Clark, M. D. Segall, C. J. Pickard, P. J. Hasnip, M. I. Probert, K. Refson, and M. C. Payne, *Zeitschrift für Kristallographie-Crystalline Materials*, 2005, **220**, 567–570.

[113] G. N. Lewis, *Journal of the American Chemical Society*, 1916, **38**, 762–785.

[114] N. Troullier and J. L. Martins, *Physical Review B*, 1991, **43**, 1993.

[115] D. Vanderbilt, *Physical Review B*, 1990, **41**, 7892.

[116] P. Borlido, J. Schmidt, A. W. Huran, F. Tran, M. A. Marques, and S. Botti, *npj Computational Materials*, 2020, **6**, 96.

[117] J. P. Perdew and A. Zunger, *Physical Review B*, 1981, **23**, 5048.

[118] D. M. Ceperley and B. J. Alder, *Physical Review Letters*, 1980, **45**, 566.

[119] J. P. Perdew, K. Burke, and M. Ernzerhof, *Physical Review Letters*, 1996, **77**, 3865.

[120] J. P. Perdew and Y. Wang, *Physical Review B*, 1992, **45**, 13244.

[121] M. S. Hybertsen and S. G. Louie, *Physical Review B*, 1986, **34**, 5390.

[122] L. Hedin, *Physical Review*, 1965, **139**, A796.

[123] C. Adamo and V. Barone, *The Journal of Chemical Physics*, 1999, **110**, 6158–6170.

[124] J. Heyd, G. E. Scuseria, and M. Ernzerhof, *The Journal of Chemical Physics*, 2003, **118**, 8207–8215.

[125] J. Harl, L. Schimka, and G. Kresse, *Physical Review B*, 2010, **81**, 115126.

[126] S. A. Tolba, K. M. Gameel, B. A. Ali, H. A. Almossalami, and N. K. Allam, *Density Functional Calculations-Recent Progresses of Theory and Application*, 2018, **1**, 5772.

[127] V. I. Anisimov, F. Aryasetiawan, and A. Lichtenstein, *Journal of Physics: Condensed Matter*, 1997, **9**, 767.

[128] J. Hubbard, *Proceedings of the Royal Society of London. Series A. Mathematical and Physical Sciences*, 1964, **277**, 237–259.

[129] V. I. Anisimov, J. Zaanen, and O. K. Andersen, *Physical Review B*, 1991, **44**, 943.

[130] M. Cococcioni and S. De Gironcoli, *Physical Review B*, 2005, **71**, 035105.

[131] R. T. Scalettar, *Quantum Materials: Experiments and Theory*, 2016, **6**.

[132] S. L. Dudarev, G. A. Botton, S. Y. Savrasov, C. Humphreys, and A. P. Sutton, *Physical Review B*, 1998, **57**, 1505.

[133] Y. Yamamoto, A. Salcedo, C. M. Diaz, M. S. Alam, T. Baruah, and R. R. Zope, *arXiv preprint arXiv:2004.13393*, 2020.

[134] M. Chen, H.-Y. Ko, R. C. Remsing, M. F. Calegari Andrade, B. Santra, Z. Sun, A. Selloni, R. Car, M. L. Klein, J. P. Perdew, et al., *Proceedings of the National Academy of Sciences*, 2017, **114**, 10846–10851.

[135] J. Sun, R. C. Remsing, Y. Zhang, Z. Sun, A. Ruzsinszky, H. Peng, Z. Yang, A. Paul, U. Waghmare, X. Wu, et al., *Nature Chemistry*, 2016, **8**, 831–836.

[136] C. E. Patrick and K. S. Thygesen, *Physical Review B*, 2016, **93**(3), 035133.

[137] B. G. Janesko, T. M. Henderson, and G. E. Scuseria, *Physical Chemistry Chemical Physics*, 2009, **11**, 443–454.

[138] A. J. Cohen, P. Mori-Sánchez, and W. Yang, *Chemical Reviews*, 2012, **112**, 289–320.

[139] L. Weston, H. Tailor, K. Krishnaswamy, L. Bjaalie, and C. Van de Walle, *Computational Materials Science*, 2018, **151**, 174–180.

[140] A. Arbuznikov, *Journal of Structural Chemistry*, 2007, **48**, S1–S31.

[141] J. P. Perdew, M. Ernzerhof, and K. Burke, *The Journal of Chemical Physics*, 1996, **105**, 9982–9985.

[142] M. R. Filip, C. E. Patrick, and F. Giustino, *Physical Review B*, 2013, **87**, 205125.

[143] B. Höffling, A. Schleife, C. Rödl, and F. Bechstedt, *Physical Review B*, 2012, **85**, 035305.

[144] G. Di Liberto, S. Tosoni, F. Illas, and G. Pacchioni, *The Journal of Chemical Physics*, 2020, **152**, 184704.

[145] D. Fang and S. Zhang, *The Journal of Chemical Physics*, 2016, **144**, 014704.

[146] Y. Hinuma, F. Oba, Y. Kumagai, and I. Tanaka, *Physical Review B*, 2013, **88**, 035305.

[147] G. Reich, *Advanced Drug Delivery Reviews*, 2005, **57**, 1109–1143.

[148] F. Giustino and A. Pasquarello, *Physical Review B*, 2008, **78**, 075307.

[149] P. Giannozzi, S. Baroni, N. Bonini, M. Calandra, R. Car, C. Cavazzoni, D. Ceresoli, G. L. Chiarotti, M. Cococcioni, I. Dabo, et al., *Journal of Physics: Condensed Matter*, 2009, **21**, 395502.

[150] A. Togo and I. Tanaka, *Scripta Materialia*, 2015, **108**, 1–5.

[151] A. Togo, *Journal of the Physical Society of Japan*, 2023, **92**, 012001.

[152] A. Shafique and Y.-H. Shin, *Scientific Reports*, 2020, **10**, 1–10.

[153] X. Gonze and C. Lee, *Physical Review B*, 1997, **55**, 10355.

[154] N. Colthup, *Introduction to infrared and Raman spectroscopy*, Elsevier Science, 2012.

[155] J. M. Skelton, L. A. Burton, A. J. Jackson, F. Oba, S. C. Parker, and A. Walsh, *Physical Chemistry Chemical Physics*, 2017, **19**, 12452–12465.

[156] I.-G. Buda, C. Lane, B. Barbiellini, A. Ruzsinszky, J. Sun, and A. Bansil, *Scientific Reports*, 2017, **7**, 1–8.

[157] Z.-h. Yang, H. Peng, J. Sun, and J. P. Perdew, *Physical Review B*, 2016, **93**, 205205.

[158] A. Ghosh, S. Jana, T. Rauch, F. Tran, M. A. Marques, S. Botti, L. A. Constantin, M. K. Niranjan, and P. Samal, *The Journal of Chemical Physics*, 2022, **157**, 124108.

[159] A. Meyer, G.-c. Wang, and H. Young, *Zeitschrift für Naturforschung A*, 1976, **31**, 898–903.

[160] H. J. Monkhorst and J. D. Pack, *Physical Review B*, 1976, **13**, 5188.

[161] M. Rutter, *Computer Physics Communications*, 2018, **225**, 174–179.

[162] W. Mönch, *Semiconductor surfaces and interfaces*, Vol. 26, Springer Science & Business Media, 2013.

[163] J. W. Furness, A. D. Kaplan, J. Ning, J. P. Perdew, and J. Sun, *The Journal of Physical Chemistry Letters*, 2020, **11**, 8208–8215.

[164] J. Bermond, J. Métois, X. Egéa, and F. Floret, *Surface Science*, 1995, **330**, 48–60.

[165] A. Stekolnikov, J. Furthmüller, and F. Bechstedt, *Physical Review B*, 2002, **65**, 115318.

[166] G.-H. Lu, M. Huang, M. Cuma, and F. Liu, *Surface Science*, 2005, **588**, 61–70.

[167] A. Ramstad, G. Brocks, and P. Kelly, *Physical Review B*, 1995, **51**, 14504.

[168] H. Kageshima, *Surface Science*, 1996, **357**, 312–316.

[169] U. Diebold, *Surface Science Reports*, 2003, **48**, 53–229.

[170] F. Labat, P. Baranek, and C. Adamo, *Journal of Chemical Theory and Computation*, 2008, **4**, 341–352.

[171] Z. Zhao, Z. Li, and Z. Zou, *Journal of Physics: Condensed Matter*, 2010, **22**, 175008.

[172] K. Laasonen, A. Pasquarello, R. Car, C. Lee, and D. Vanderbilt, *Physical Review B*, 1993, **47**, 10142.

[173] L. Bengtsson, *Physical Review B*, 1999, **59**, 12301.

[174] L. A. Cipriano, G. Di Liberto, S. Tosoni, and G. Pacchioni, *The Journal of Physical Chemistry C*, 2021, **125**(21), 11620–11627.

[175] H. Seo, A. B. Posadas, C. Mitra, A. V. Kvit, J. Ramdani, and A. A. Demkov, *Physical Review B*, 2012, **86**(7), 075301.

[176] R. Puthenkovilakam, E. A. Carter, and J. P. Chang, *Physical Review B*, 2004, **69**(15), 155329.

[177] M. Ribeiro Jr, L. R. Fonseca, and L. G. Ferreira, *Physical Review B*, 2009, **79**(24), 241312.

[178] O. Romanyuk, O. Supplie, T. Susi, M. May, and T. Hannappel, *Physical Review B*, 2016, **94**(15), 155309.

[179] C. Howard, T. Sabine, and F. Dickson, *Acta Crystallographica Section B: Structural Science*, 1991, **47**, 462–468.

[180] L. Kavan, M. Grätzel, S. Gilbert, C. Klemenz, and H. Scheel, *Journal of the American Chemical Society*, 1996, **118**, 6716–6723.

[181] C. E. Patrick and F. Giustino, *Journal of Physics: Condensed Matter*, 2012, **24**, 202201.

[182] A. Zoroddu, F. Bernardini, P. Ruggerone, and V. Fiorentini, *Physical Review B*, 2001, **64**, 045208.

[183] F.-Q. Bai, W. Li, and H.-X. Zhang, *Titanium Dioxide*, 2017, pp. 229–248.

[184] M. Arroyo-de Dompablo, A. Morales-García, and M. Taravillo, *The Journal of Chemical Physics*, 2011, **135**, 054503.

[185] D. W. Ball and J. A. Key, *Introductory Chemistry; 1st Canadian Edition*, BCcampus, 2014.

[186] L. Chen, W. Tian, C. Sun, F. Cao, and L. Li, *ACS Applied Materials & Interfaces*, 2018, **11**, 3241–3250.

[187] I. Marri, M. Amato, M. Bertocchi, A. Ferretti, D. Varsano, and S. Ossicini, *Physical Chemistry Chemical Physics*, 2020, **22**, 25593–25605.

[188] M. Rutter and J. Robertson, *Physical Review B*, 1998, **57**, 9241.

[189] C. Sgiarovello, N. Binggeli, and A. Baldereschi, *Physical Review B*, 2001, **64**, 195305.

[190] W. J. Kim, M. H. Han, S. Lebègue, E. K. Lee, and H. Kim, *Frontiers in Chemistry*, 2019, **7**, 47.

[191] W. Chen and A. Pasquarello, *Physical Review B*, 2012, **86**, 035134.

[192] R. Shaltaf, G.-M. Rignanese, X. Gonze, F. Giustino, and A. Pasquarello, *Physical Review Letters*, 2008, **100**, 186401.

[193] C. E. Patrick and K. S. Thygesen, *Physical Review B*, 2016, **93**, 035133.

[194] C. E. Patrick and F. Giustino, *Physical Review Letters*, 2012, **109**, 116801.

[195] H.-P. Komsa, P. Broqvist, and A. Pasquarello, *Physical Review B*, 2010, **81**, 205118.

[196] K. F. Garrity, J. W. Bennett, K. M. Rabe, and D. Vanderbilt, *Computational Materials Science*, 2014, **81**, 446–452.

[197] M. Bogey, B. Delcroix, A. Walters, and J.-C. Guillemin, *Journal of Molecular Spectroscopy*, 1996, **175**, 421–428.

[198] M. T. Lan, T. T. Duong, N. V. Huy, and N. Van Hong, *Materials Research Express*, 2017, **4**, 035202.

[199] M. K. Weldon, B. B. Stefanov, K. Raghavachari, and Y. Chabal, *Physical Review Letters*, 1997, **79**, 2851.

[200] A. B. Gurevich, B. B. Stefanov, M. K. Weldon, Y. J. Chabal, and K. Raghavachari, *Physical Review B*, 1998, **58**, R13434.

[201] D. Tsu, G. Lucovsky, and B. Davidson, *Physical Review B*, 1989, **40**, 1795.

[202] D. Dutoit, M. Schneider, and A. Baiker, *Journal of Catalysis*, 1995, **153**, 165–176.

[203] D. Sarkar, D. Brassard, M. El Khakani, and L. Ouellet, *Thin Solid Films*, 2007, **515**, 4788–4793.

[204] A. Bertoluzza, C. Fagnano, M. A. Morelli, V. Gottardi, and M. Guglielmi, *Journal of Non-Crystalline Solids*, 1982, **48**, 117–128.

[205] A. R. Kumar, T. Rao, K. Neeraja, M. R. Reddy, and N. Veeraiah, *Vibrational Spectroscopy*, 2013, **69**, 49–56.

[206] S.-Y. Lin, *Applied physics letters*, 1997, **70**, 203–205.

[207] X. Gao and I. E. Wachs, *Catalysis Today*, 1999, **51**, 233–254.

[208] N. T. McDevitt and W. L. Baun, *Spectrochimica Acta*, 1964, **20**, 799–808.

[209] D. Keomany, C. Poinsignon, and D. Deroo, *Solar Energy Materials and Solar Cells*, 1994, **33**, 429–441.

[210] J. Bandekar and S. Klima, *Journal of Molecular Structure*, 1991, **263**, 45–57.

[211] A. Trejo, A. Miranda, L. N. De Rivera, A. Díaz-Méndez, and M. Cruz-Irisson, *Microelectronic Engineering*, 2012, **90**, 92–95.

[212] N. Yang, W. Li, and L. Dong, *New Journal of Chemistry*, 2020, **44**, 11056–11063.

[213] C. Messmer and J. Bilello, *Journal of Applied Physics*, 1981, **52**, 4623–4629.

Acknowledgements

First of all, I would like to thank my supervisors, Dr. Christopher Patrick and Prof. Jonathan Yates for their guidance, support, and encouragement during my two years research journey. Their profound knowledge and insightful ideas have been important in shaping my research, and I could not have completed this work without their help. I have learned so much useful knowledge and simulation skills from them, which I believe will be really valuable for my further Ph.D. study in China.

I would also like to thank my friends Liren, Runze, and Zisheng for their support and inspiration in various ways during my graduate studies. The conversations during lunchtime at St Anne's College have been some of my precious memories. I wish you guys all the best in your future studies.

I would also like to express my gratitude to my parents and my brother for their love and understanding throughout the years. Their patience and encouragement have helped me overcome many challenges and have allowed me to pursue my dreams. Finally, I would like to thank my girlfriend Yuxiao who has always been a source of love and inspiration. I understand that our long-distance relationship has its challenges, but with you, every moment is worth it. I want to thank you for always being by my side, supporting me, and making me feel happy even when we are miles apart. I am blessed to have you in my life.

To everyone I have met at Oxford, thank you from the bottom of my heart.